

UNIVERSITÄTSKLINIKUM HAMBURG-EPPENDORF

Institut für Immunologie

Prof. Dr. Marcus Altfeld

Optimization of nanobodies for *in vivo* targeting of P2X7 ion channel on brain microglia and kidney T cells

Dissertation

zur Erlangung des Doktorgrades Dr. rer. biol. hum. / PhD
an der Medizinischen Fakultät der Universität Hamburg.

vorgelegt von:

Carolina Pinto Espinoza
aus Arequipa, Peru

Hamburg 2018

(wird von der Medizinischen Fakultät ausgefüllt)

**Angenommen von der
Medizinischen Fakultät der Universität Hamburg am:** _____

**Veröffentlicht mit Genehmigung der
Medizinischen Fakultät der Universität Hamburg.**

Prüfungsausschuss, der/die Vorsitzende: _____

Prüfungsausschuss, zweite/r Gutachter/in: _____

Prüfungsausschuss, dritte/r Gutachter/in: _____

Table of contents

1. Introduction	5
1.1. The nucleotide-gated P2X7 ion channel	5
1.1.1. P2X7-mediated purinergic signaling on immune cells	6
1.1.2. The role of P2X7 on inflammatory disorders	9
1.1.3. The role of P2X7 in neurodegenerative disorders, epilepsy, and psychiatric mood disorders	10
1.1.4. P2X7 antagonists	11
1.2. The adaptive immune system and the antibody response	13
1.2.1. Conventional antibodies	14
1.2.2. Heavy chain antibodies (hcAbs) and nanobodies (Nbs)	16
1.3. The blood brain barrier (BBB)	18
1.3.1. BBB transport mechanisms	19
1.3.2. Delivery of drugs to the Central nervous system (CNS)	21
1.3.3. Targeting P2X7 in the CNS	22
1.4. Goals of the project	24
2. Materials and Methods	25
2.1 Materials	25
2.2 Methods	33
2.2.1 Molecular biology methods	33
2.2 Cell biology methods	39
2.3 Immunology methods	42
2.2.3 Protein biochemistry methods	47
2.2.5 Animal experiments	49
3. Results	52
3.1 Nanobody (Nb) engineering	52
3.1.1 Cloning and reformatting of P2X7-antagonistic nanobodies	52
3.1.2 Expression, purification and chemical characterization of the engineered nanobodies	55
3.2 <i>In vitro</i> targeting of P2X7 with engineered bivalent P2X7-antagonistic half-life extended nanobodies	57
3.2.1 Monovalent and bivalent formats of nanobodies bind P2X7 with high specificity	57
3.2.2 Bivalent P2X7-specific nanobodies block ATP-induced Ca ²⁺ influx more potently than their monovalent counterparts	58
3.2.3 Dimeric half-life extended P2X7-specific nanobodies effectively block ATP-induced release of IL1- β by endotoxin-primed primary microglia	59

3.2.4 Dimeric half-life extended P2X7 nanobody 13A7 blocked ASC speck formation in endotoxin-primed peritoneal macrophages	60
3.3 <i>In vivo</i> targeting of the P2X7 ion channel with engineered bivalent P2X7-antagonistic half-life extended nanobodies.....	62
3.3.1 Full occupancy of P2X7 on microglia can be achieved by a high dose of intravenously injected 13A7-dim HLE	64
3.3.2 Complete occupancy of P2X7 on renal T helper Th cells is achieved by a 300-fold lower dose of intravenously injected 13A7-dim HLE.....	66
3.3.3 Unbound soluble 13A7-dim HLE are detected in the serum in a dose-dependent manner 4 h after intravenous administration.....	69
3.3.4 Full occupancy of P2X7 on microglia can be achieved by a high dose of intravenously injected 1c81-dim ^{sh} HLE	70
3.3.5 AAV-based <i>in vivo</i> production of 13A7-dim HLE results in an extensive and durable occupancy of P2X7 in microglia	72
3.3.6 Intracerebroventricular (icv) injection of 1c81-dim ^{sh} HLE allows a 100-fold reduction of the iv dose to achieve full P2X7 occupancy on microglia.....	76
3.3.7 A low dose of bivalent HLE nanobodies achieved full occupancy of P2X7 on microglia 48 h following icv administration	80
4. Discussion	82
4.1 Engineering and production of P2X7-antagonistic nanobodies	82
4.2 Potential advantages and limitations of engineered nanobodies.....	84
4.3 Occupancy of P2X7 brain microglia and renal T cells by intravenously injected nanobodies	85
4.4 Occupancy of P2X7 brain microglia and renal T cells by endogenously produced nanobodies	89
4.5 Other strategies to improve penetration of nanobodies through the BBB	90
4.6 Perspectives	93
5. Abstract.....	94
6. Zusammenfassung.....	95
7. Abbreviations	96
8. References	99
9. List of Figures and tables	112
10. Acknowledgements.....	114
Curriculum vitae	116
Eidesstattliche Versicherung	117

1. Introduction

1.1. The nucleotide-gated P2X7 ion channel

The purinergic receptor P2X7 is a ligand gated non-selective-cation channel that is prominently expressed by immune cells, including microglia in the CNS, and monocytes, macrophages and T-lymphocytes in the periphery (Ferrari et al., 2006). Structurally, the channel is a homomeric trimer composed of three subunits that self-assemble during translation into stable complexes that mainly traffic to the plasma membrane (Khakh and North, 2006; Nicke, 2008) (Fig. 1). P2X7 is the largest member of the P2X family, with 595 amino acids and a molecular weight of 72 kDa (Surprenant et al., 1996). It has two hydrophobic transmembrane segments that are connected by a glycosylated extracellular domain of 295 amino acids including 10 conserved cysteine residues. The side chains of these cysteine residues form 5 conserved intrachain disulfide bonds.

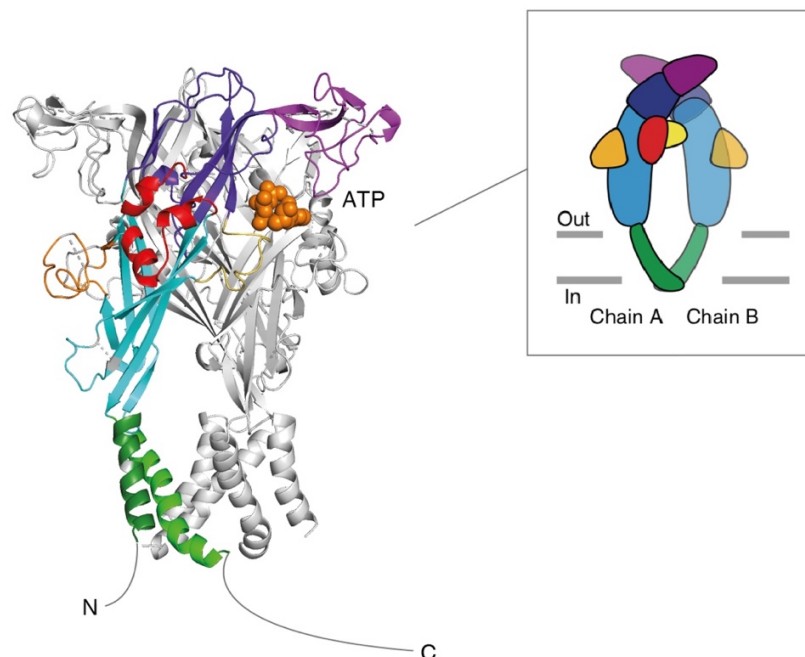


Figure 1. Structural characteristics of P2X7. P2X7 model based on the crystal structure of zebra fish P2X4. The P2X7 ion channel assembles from three subunits; each subunit is compared to a dolphin. The tail flukes correspond to two transmembrane domains (grey). The body projects into the extracellular compartment with the right (red), and left (yellow) flipper, dorsal fin (orange) and head (purple). The ATP-binding pocket is formed by 4 amino acids of one subunit and 7 amino acids of the adjacent subunit, corresponding to the head domain of one dolphin bent downwards toward the left flipper of the adjacent subunit. Binding of ATP causes a conformational shift forming a channel through which ions permeate. The 240 amino acid long C-terminal tail is involved in triggering pore formation. Adapted from (Hattori and Gouaux, 2012) and (Kasuya et al., 2017).

Each extracellular domain is often compared with a dolphin's body. The three ATP-binding pockets each are located between the head domain of one dolphin-subunit bent downwards toward the left flipper of the adjacent dolphin-subunit. The short amino (N) and the long carboxy (C) terminal domains are located in the cytosol (Bradley et al., 2011a; Jiang et al., 2013; Nicke, 2008; North, 2016; Roger et al., 2010). The long C-terminus is thought to be important to mediate the effects of P2X7 activation (Adriouch et al., 2002; Becker et al., 2008; Smart et al., 2003) (Fig. 1).

The structure of the P2X7 receptor among species is conserved: monkey, dog, rat and mouse P2X7 share respectively 96%, 85% and 80% sequence identity to human P2X7 (Bianchi et al., 1999; Bradley et al., 2011b; Donnelly-Roberts et al., 2009; Roman et al., 2009; Surprenant et al., 1996).

P2X7-mediated purinergic signaling on immune cells

Adenosine triphosphate (ATP) is a nucleotide with a central role in intracellular energy supply. ATP can be released to the extracellular milieu upon cellular damage, stress or necrosis (non-physiological cell death), acting as an endogenous "alarmin" or damage associated molecular pattern (DAMP). Although the release of ATP is uncontrolled under pathological conditions, ATP can be released also in a regulated fashion to stimulate cell proliferation and tissue repair (Idzko et al., 2014; Junger, 2011; la Sala et al., 2003). The release of ATP from apoptotic, inflammatory cells or vascular endothelia involves transmembrane protein channels such as pannexins or connexins (Chekeni et al., 2010; Eltzschig et al., 2006; Eltzschig et al., 2008; Faigle et al., 2008; Idzko et al., 2014).

Extracellular ATP activates P2X7 in a canonical manner. Upon binding of ATP, the channel gates to the open state, facilitating a rapid influx of Na⁺ and Ca⁺² and an efflux of K⁺, which results in a rapid membrane depolarization, decreased K⁺ concentrations and increased Ca⁺² and Na⁺ concentrations in the cytosol. An alternative mode of P2X7 activation that mimics ATP-binding has also been described: Another extracellular DAMP molecule, nicotinamide adenine dinucleotide (NAD⁺), indirectly induces gating of P2X7 by serving as a substrate for the toxin-related ecto-enzyme ART2 (ADP-ribosyltransferase 2), which catalyzes the covalent transfer of the ADP-ribose moiety from NAD⁺ to Arg125 of P2X7. ART2 and P2X7 are co-expressed by T lymphocytes

and iNKT cells, on which P2X7 can be activated by micromolar concentrations of NAD^+ (Adriouch et al., 2008; Haag et al., 2007; Young, 2010).

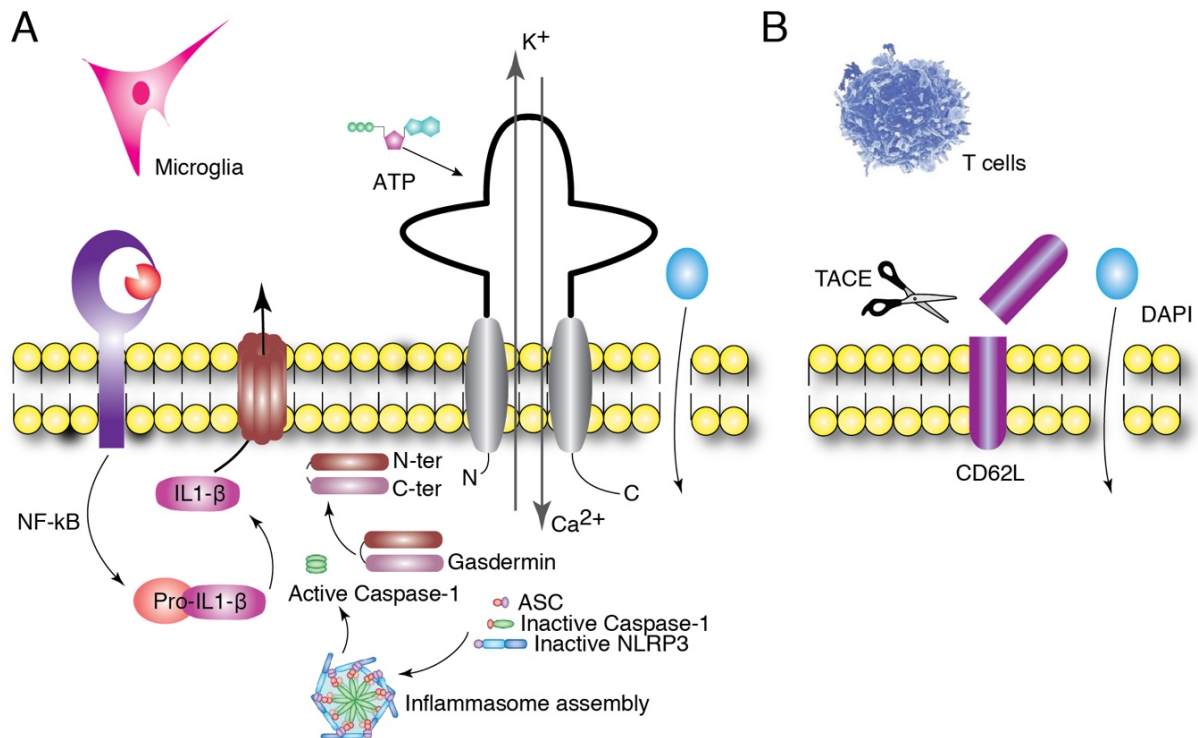


Figure 2. ATP-induced P2X7-mediated downstream effects on microglia and T lymphocytes. Following ATP binding, P2X7 gates a Ca^{2+} influx and a K^+ efflux. **(A)** In microglia, this assembles a protein complex known as the inflammasome, which is composed by cryopirin (NALP3), apoptosis associated speck-like adaptor protein (ASC) and caspase-1. The inflammasome activates caspase-1 by proteolysis; activated caspase-1 in turn cleaves, on one hand, the dimeric protein Gasdermin into C-terminal (C-ter) and N-terminal (N-ter) domains. The released N-ter monomer oligomerizes in the cell membrane forming a pore. On the other hand, caspase-1 cleaves the precursor of IL-1 β (Pro-IL-1 β) into IL-1 β , which is released to the extracellular compartment through the Gasdermin N-ter pore. Pro-IL-1 β is synthesized following the engagement of the TLR-pathway in response to PAMPs and accumulates within the cell cytosol. **(B)** On T cells P2X7 activation by ATP binding leads to the shedding of the ectodomain of L-selectin (CD62L) and other proteins by metalloproteases of the ADAM family such as TNF- α converting enzyme (TACE). Furthermore, gating of P2X7 on both immune cell types induces macropore formation in the cell membrane allowing free diffusion of molecules up to 900 Da e.g. the DNA-intercalating compound dye DAPI.

Figure 2 summarizes diverse intracellular signaling pathways triggered by gating of P2X7 on T cells and microglia (Fig. 2). On myeloid cells such as microglia, monocytes, and macrophages, activation of P2X7 requires millimolar concentrations of ATP (Yan et al., 2010). Gating of P2X7 triggers the recruitment of three proteins: NALP3 or cryopirin (NOD-like receptor subfamily containing a pyrin domain 3), ASC (apoptosis

associated speck-like adaptor protein) and inactive caspase-1. These proteins assemble into a protein complex known as the NALP3 inflammasome. The inflammasome drives the proteolytic activation of caspase-1, which in turn cleaves the precursor of the proinflammatory cytokines, interleukin 1 β and 18 (Pro-IL1- β , Pro-IL18) into mature IL1- β and IL18 respectively (Di Virgilio, 2007; Ferrari et al., 2006; Solle et al., 2001) (Fig. 2A). Pro-IL1- β and Pro-IL18 are synthesized in response to microbial infection and accumulate within the cytosol. Hence, molecular motifs carried by pathogens “pathogen associated molecular patterns” (PAMPs) act through pattern recognition receptors (PRR's) on monocytes, macrophages and microglia engaging the NF κ B signaling pathway that induce the expression of the genes *Il1b* and *Il18*. This process is referred to as priming (Lopez-Castejon and Brough, 2011; Takenouchi et al., 2009) (Fig. 2A). Following maturation, IL1- β and IL18 are released to the extracellular milieu. It was originally proposed that the release of these leaderless cytokines proceeds through pannexin 1 hemichannels or microvesicles that are shed from the plasma membrane (Nickel and Rabouille, 2009; Pelegrin and Surprenant, 2006; Rubartelli et al., 1990) (Fig. 2A). Recent studies have implicated Gasdermin D in the release of IL-1 β (Evavold et al., 2018; Shi et al., 2017). Gasdermin is composed by two domains connected by a linker. The latter is a target for cleavage by caspase-1. The N-terminal domain of Gasdermin D binds to lipid phosphoinositides in the plasma membrane and oligomerizes to form a pore through which IL1- β is released (Evavold et al., 2018; Shi et al., 2017) (Fig. 2A). Other pro-inflammatory mediators including TNF- α and IL-6R are released from myeloid cells in a P2X7-dependent manner (Garbers et al., 2011; Suzuki et al., 2004). These cytokines are cleaved from by metalloproteases of the ADAM family from precursor transmembrane proteins (Blobel, 2005).

On T cells, P2X7 is gated by micromolar concentrations of ATP and NAD⁺. This leads to a transient and reversible externalization of phosphatidylserine on the outer leaflet of the plasma membrane, probably induced by the influx of Ca⁺² ions (Fadeel, 2004; Scheuplein et al., 2009; Seman et al., 2003). Depending on the magnitude and the duration of P2X7 stimulation, it can lead to necrotic cytolysis or apoptotic cell death (Adriouch et al., 2007; Ferrari et al., 2006; Hubert et al., 2010). Moreover, ADAM 17 or TACE (TNF- α converting enzyme) and ADAM 10 have been implicated in ATP-induced

shedding of L-selectin (CD62L) and CD27 by T cells and iNKT cells (Le Gall et al., 2009; Moon et al., 2006) (Fig. 2B).

Prolonged activation of P2X7 on both, macrophages and T cells, triggers the formation of pores that permeate the membrane to molecules up to 900 Da in size, which ultimately lead to disruption of the plasma membrane and cell death (Di Virgilio, 1995; Di Virgilio et al., 2017; Dubyak, 2012; Yan et al., 2008) (Fig. 2). The mechanism is not yet completely understood; however, it is thought to involve pannexin channels (Baroja-Mazo et al., 2013; Gulbransen et al., 2012; Pelegrin and Surprenant, 2006) and/or Gasdermin D pores (Evavold et al., 2018; Shi et al., 2017).

While P2X7-mediated efflux of K⁺ ions is a potent trigger of NALP3 inflammasome assembly (Jin and Flavell, 2010; Petrilli et al., 2007), other P2X7-independent mechanisms of inflammasome activation have also been described in the literature, including the generation of ROS (reactive oxygen species), lysosomal destabilization and the translocation of microbial ligands into the host cytosol (Lamkanfi and Dixit, 2009; Mariathasan et al., 2006; Martinon et al., 2006; Tschopp and Schroder, 2010).

The role of P2X7 on inflammatory disorders

By triggering the release of IL-1 β , P2X7 plays a crucial role in promoting innate immune responses against infection, immunological challenge, and tissue injury. IL-1 β is pyogenic, promotes leukocyte transmigration and activates T-lymphocytes (Dinarello, 2011; Sims and Smith, 2010).

P2X7 has been associated with several inflammatory and autoimmune diseases. Genetic deletion and pharmacological inhibition of P2X7 has shown to ameliorate the disease progression in animal models of inflammatory or autoimmune disorders. P2X7 knockout mice display an attenuated form of experimental glomerulonephritis (EAG) (Taylor et al., 2009). P2X7 deficient mice were resistant to develop T-cell mediated allergic contact dermatitis type IV in response to allergens and the underlying mechanism has been shown to involve P2X7-mediated inflammasome activation and the release of IL1- β (Weber et al., 2010).

Multiple Sclerosis (MS) is a chronic neuroinflammatory disease that is characterized by focal inflamed lesions, infiltration of immune cells, demyelination, oligodendroglial death, and axonal damage (Sperlagh and Illes, 2014). The role of P2X7 in MS has

been investigated by means of animal models of experimental autoimmune encephalomyelitis (EAE): P2X7 deficient mice showed diminished CNS inflammation, axonal damage, and astrocytes activation (Sharp et al., 2008). Moreover, treatment with small molecule P2X7 inhibitors prevented oligodendrocyte excitotoxicity and ameliorated the score of the disease (Matute et al., 2007). Consistently, pharmacological P2X7 blockade in a rat EAE model markedly reduced astrogliosis and alleviated neurological symptoms (Grygorowicz et al., 2016).

Genetic deletion of P2X7 as well as IL1- β ensued in alleviation of inflammatory and neuropathic pain (Chessell et al., 2005; Goloncser and Sperlagh, 2014; Honore et al., 2006) and P2X7 blockade with small molecules have similarly shown benefit in the treatment of neuropathic pain in mouse and rat models (Abdi et al., 2010; Brumfield et al., 2011; Goloncser and Sperlagh, 2014; He et al., 2012; Huang et al., 2014; Ito et al., 2013; Matasi et al., 2011).

Middle cerebral artery occlusion (MCAO) is a surgical procedure used as a model of focal cerebral ischemia. MCAO impairs irrigation in a focal brain area thereby triggering locally, an oxygen/glucose deprivation that in turn provokes anoxic depolarization, cell damage and death. In the surrounding area, so-called penumbra the cellular damage is reversible. P2X7 antagonists decreased both infarct size and neurological deficits. In addition, upregulation of P2X7 was documented in microglia, astrocytes and neurons (Arbeloa et al., 2012; Lammer et al., 2011). Similar results were reported for subarachnoid hemorrhage (Chen et al., 2013), traumatic brain (Kimble et al., 2012; Roth et al., 2014) or spinal cord injury (Peng et al., 2009) and ischemic retina degeneration (Niyadurupola et al., 2013). Using a model global cerebral ischemia, the neuroinflammatory reaction ensuing reperfusion was alleviated by P2X7 antagonists (Chu et al., 2012; Domercq et al., 2010; Yu et al., 2013).

The role of P2X7 in neurodegenerative disorders, epilepsy, and psychiatric mood disorders

P2X7 has also been implicated in neurodegenerative disorders, including Alzheimer's disease (AD) and Huntington's Disease. One of the neuropathological hallmarks of Alzheimer's disease (AD) is the appearance of amyloid plaques. These plaques consist of extracellular deposits of β -amyloid peptide ($A\beta$) surrounded by reactive microglia. In a mouse model of AD, treatment with P2X7 small molecule antagonists

led to a significant decrease in the number of hippocampal amyloid plaques (Delarasse et al., 2011; Diaz-Hernandez et al., 2012). Moreover, β -amyloid peptide ($A\beta$) triggered IL1- β production in a P2X7-dependent manner (Rampe et al., 2004) (Sanz et al., 2009). P2X7 was also found to be upregulated in post-mortem brain tissue from AD patients (McLarnon et al., 2006). Huntington's disease is an autosomal dominant disorder caused by a trinucleotide repeat mutation-like in the HHT gene coding for the huntingtin protein. Here, up-regulation of P2X7 was observed in brains of transgenic mouse models of the disease and P2X7 blockade dampened the disease score and progression (Diaz-Hernandez et al., 2009).

In mouse models of epilepsy, expression of P2X7 was upregulated on microglia, astrocytes and neurons (Dona et al., 2009; Kim et al., 2009) and treatment with P2X7 antagonists reduced the release of IL1- β by microglia, contributing to neuroprotection and seizure suppression (Engel et al., 2012; Jimenez-Pacheco et al., 2013).

P2X7 has been implicated to play a role in neuropsychiatric diseases. Genetic polymorphisms of the human P2X7 gene are associated with bipolar disorders and depression (McQuillin et al., 2009; Roger et al., 2010; Soronen et al., 2011). In mouse models of depression and mania, genetic deletion of P2X7 resulted in protective phenotype (Basso et al., 2009; Boucher et al., 2011) and P2X7 antagonism validated this outcome (Csolle et al., 2013). Consistently, overexpression of IL1- β has been observed in patients with mood disorders and in animal models (Rao et al., 2010; Soderlund et al., 2011).

Together, these studies indicate a pivotal role of P2X7 in the pathogenesis of a variety of diseases, in many cases involving a sustained inflammatory tone by the release of IL1- β . Therefore, this channel represents an attractive target for therapeutic purposes.

P2X7 antagonists

Three categories of P2X7 antagonists can be defined: 1) ions such as Ca^{+2} , Zn^{+2} , Mg^{+2} and protons (Friedle et al., 2010; Guile et al., 2009); 2) ATP analogs and other small, chemically manufactured molecules including the non-selective compounds such as PPADS, Brilliant Blue, suranim, KN-62, as well as more selective lead drugs discovered by high throughput screenings, and 3) biological antagonists including antibodies and nanobodies.

Many of the antagonists used in the studies cited above belong to the second category and currently are broadly used as research tools, but only a few have entered clinical trials. GKS reported a Phase I study with healthy individuals aiming to assess the safety and tolerability of the pyroglutamic acid amide GSK1482160. The release of IL1- β from LPS-primed human monocytes was monitored *ex vivo*. High doses were required to inhibit the release of IL1- β , overly high to compromise the patient safety (Ali et al., 2013). Two other Phase II clinical trials were conducted with CE224,535 (Pfizer) and AZD9056 (AstraZeneca) for the treatment of rheumatoid arthritis (RA). The compounds were safe and well tolerated. While these compounds blocked *ex vivo* the ATP-induced IL-1 β release from human monocytes, the patients did not show significant improvement in the clinical parameters of this disease (Chrovia et al., 2014; Keystone et al., 2012; Stock et al., 2012). Despite their pre-clinical efficacy in animal models, the outcome of these clinical trials illustrates insufficient safety, lack of potency and efficacy of the aforementioned compounds, which impeded their translation into the clinics. Small molecule inhibitors often show short *in vivo* half-life, off-target side effects, and conversion into toxic or inefficacious metabolites (Arulkumaran et al., 2011; Brumfield et al., 2011; Chen et al., 2010; Perez-Medrano et al., 2009; Subramanyam et al., 2011). Biologics may offer more selectivity with better metabolic stabilities and pharmacokinetic profiles (Bartlett et al., 2014).

Biologics are a class of drugs based on proteins with therapeutic effect, which comprise antibodies, antibody fragments and nanobodies. These large molecules generally display a longer half-life than small molecule drugs. Depending on their size some of them do not pass through the renal filtration barrier. Furthermore, since they bind their target with a high specificity, off-target side effects and the associated toxicity are strongly reduced. In 1998, Buell et al. reported a monoclonal antibody, designated L4 that partially blocked *ex vivo* P2X7 function on human monocytes (Buell et al., 1998). More recently, the mouse P2X7-specific monoclonal antibody 1F11 was demonstrated to inhibit mast cell activation and to prevent intestinal inflammation in mice (Kurashima et al., 2012).

Nanobodies, single domain antibodies derived from camelid heavy chain antibodies, have shown to access cavities or clefts on membrane proteins that often are inaccessible to antibodies (De Genst et al., 2006). The ART2-antagonistic nanobody s+16 effectively blocked ART2-catalyzed ADP-ribosylation mediated activation of

P2X7 on T cells and prevented NAD-induced cell death (Koch-Nolte et al., 2007). Moreover, the mouse P2X7-specific antagonistic nanobody 13A7 effectively blocked both, NAD- and ATP-induced gating of P2X7 and alleviated two different mouse models of inflammatory diseases: glomerulonephritis induced by anti-podocyte antibodies (Meyer-Schwesinger et al., 2011) and allergic contact dermatitis (Danquah, 2012; Danquah et al., 2016; Sun and Li, 2013). Similarly, the human P2X7-specific nanobody Dano1 inhibited the release of IL-1 β from LPS-primed human blood with a 1000-fold more potency than other P2X7 small molecule inhibitors (Danquah, 2012; Danquah et al., 2016; Sun and Li, 2013).

1.2. The adaptive immune system and the antibody response

The adaptive arm of the immune system of vertebrates encompasses cellular and antibody responses. Cellular responses are mediated by T lymphocytes and antibody responses are mediated by B lymphocytes. These cells express antigen-binding receptors that have evolved to be rich in diversity, thus an enormous repertoire of receptors is generated allowing the immune system to respond to any existing antigen. Following infection or immunization, professional antigen processing cells (APCs) process and present antigen via the major histocompatibility complex class II (MHC-II). This complex consisting of the MHC-II loaded with an antigen-derived peptide is recognized by the T cell receptor of a T cell clone expressing the CD4 coreceptor of the MHC-II molecule. The result of this particular interaction is the activation of the T cell. Besides, B cells with the appropriate surface immunoglobulin receptor bind the cognate antigen and following processing, present antigen-derived peptides in the MHC-II context to activated CD4⁺ T cells. Upon binding, CD4⁺ T cells, called T helper (Th) cells, provide a stimulus to B cells via the interaction between CD40 expressed on the B cell and CD40L expressed on the T cell. This results in the release of cytokines such as IL-4 and IL-6 by the activated T cell, which in turn activates the B cell to divide and differentiate, creating a large population of antibody producing cells specific to the antigen. Moreover, by a well-regulated mechanism of mutations and selection, known as affinity maturation, repeated antigen encounters lead to the preferential expansion of B cell clones expressing antibodies with higher affinities (Murphy and Weaver, 2016).

Conventional antibodies

Conventional antibodies are glycosylated proteins that belong to the immunoglobulin (Ig) superfamily. The most abundant serum mammalian Ig is the IgG antibody comprising 75% of all serum antibodies (Murphy and Weaver, 2016). It is composed of two copies each of a polypeptide heavy and light chain. These polypeptide chains comprise domains of about 100-110 aminoacids, so called Ig domains. Light chains have two Ig domains whereas heavy chains have 4 to 5 domains depending on the antibody class. The heavy chain has a molecular weight of ~50 kDa whereas the light chain has a smaller size of ~25 kDa. The Ig fold consists of a pair of β sheets of antiparallel strands. Hydrophobic interactions permit the association of two identical heavy with two identical light chains forming a Y-shaped 150 kDa IgG antibody. A conserved disulfide bond links the C-terminus of the light chain with the upper hinge of the heavy chain and two or more additional disulfide bonds in the hinge region establish covalent connections between the heavy chains (Davies and Cohen, 1996) (Fig. 3A).

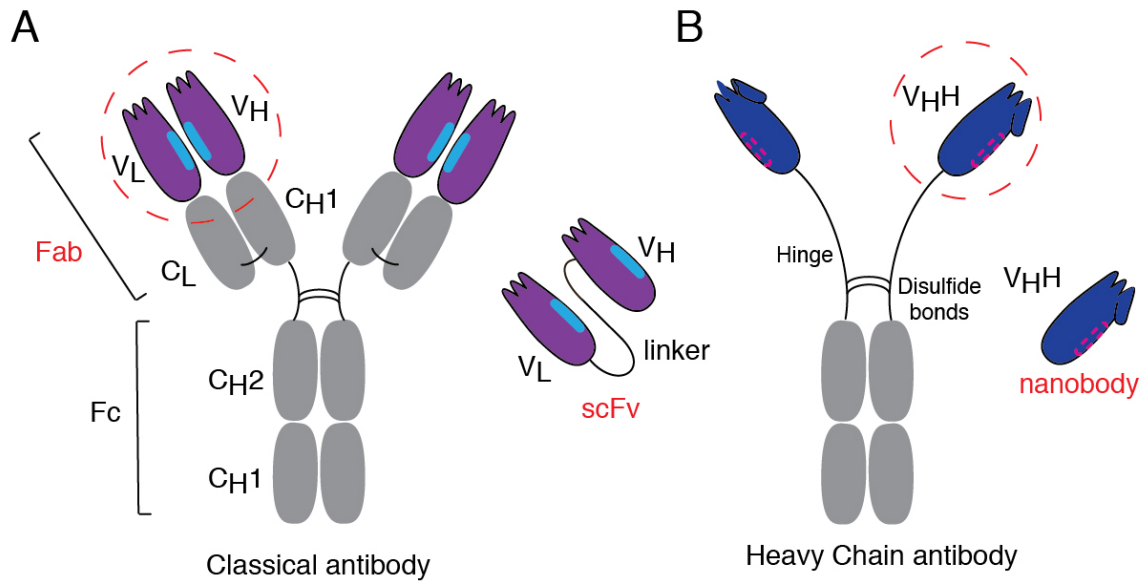


Figure 3. Structural features of conventional antibodies vs. heavy chain antibodies.

Conventional (IgG1) and heavy chain antibodies (hcAbs, IgG2, IgG3) are found in the sera of Camelids. **(A)** Conventional antibodies comprise two heavy polypeptide chains and two light chains. Each light chain is composed of a variable domain (V_L) and a constant domain (C_L) while the heavy chain is composed of one variable domain (V_H), three constant domains (C_{H1}, C_{H2}, C_{H3}) and a hinge region between the C_{H1} and C_{H2} domains. The antigen-binding site is formed by three CDR loops at the tip of the molecule (indicated by finger shapes). The association of V_L and V_H domains is stabilized by hydrophobic interaction between V_H and V_L domains, depicted as blue ellipses. These domains can be genetically fused through a Gly-Ser peptide linker into a single chain variable fragment (scFv). The association of the V_L-C_L together with the V_H-C_{H1} is called Fab fragment. Disulfide bonds mediate the association of the heavy chain with the light chain and between the two heavy chains. The C_{H2}-C_{H3} domains compose the Fc region that mediates effector functions. **(B)** HcAbs are devoid of light chains and the C_{H1} domain; therefore, the antigen-binding module is reduced to a single domain, designated V_HH, single domain antibody (sdAb) or nanobody (because of their small size). The V_HH domain bears hydrophilic amino acids (red dashed line) where V_H domains bear hydrophobic residues for binding to the V_L domain. V_HH domains, therefore do not display any propensity to bind to V_L domains or to interact with other hydrophobic domains. A Pro-rich flexible hinge connects the V_HH domain directly to the C_{H2} and C_{H3} domains (Fc region). As in conventional antibodies, disulfide bonds in the lower hinge region mediate the association of the two heavy chains. The hinge region of hcAbs lacks the cysteine for connection to a V_L domain.

The N terminal domain of both heavy and light chains shows a sequence with high variability, designated therefore variable domain (V_L and V_H for light and heavy chain, respectively). In contrast, the C terminal domains are conserved, denoted constant (C) domains. The light chain possesses one constant domain (C_L) whereas the heavy chain has three or four domains (C_{H1}-C_{H4}). In IgG and IgA isotypes, the C_{H1} links to the C_{H2} through a flexible proline-rich stretch of amino acids referred to as the hinge

region. The portion corresponding to the last two domains (C_{H2} - C_{H3}) is designated Fc domain and mediates the effector responses upon antigen binding. In IgM and IgE isotypes, the hinge is replaced by a proper C domain, designated C_{H2} . The region that binds to the antigen is called antigen-binding fragment (Fab), it consists of the variable domain and neighboring constant domain of each chain connected by the disulfide bond between the C-terminal cysteine of the light chain and the upper cysteine of the hinge region. Fab fragments can be generated from intact IgG *in vitro* by enzymatic cleavage or by genetic engineering approaches (Murphy and Weaver, 2016) (Fig. 3A). The V_L domain together with the V_H domain contains the paratope or antigen-binding site, which consists of a set of three complementary determining regions (CDR) in each V domain. Structurally, these CDRs correspond to loops of hypervariable sequences that are intercalated between β -strands of more conserved framework regions (FR1-FR4). The CDR3 region displays the highest diversity and therefore builds the core of the contact with the antigen. The high diversity of the CDR3 is encoded by new DNA segments generated by DNA recombination and nucleotide insertions/deletions at the junction point that occur during early B cell development (Davies and Cohen, 1996; Kabat and Wu, 1991). The V_L and the V_H domains can be genetically fused *in vitro* through a short linker to form the so-called scFv (Fig. 3A).

Antibodies bind pathogens either to neutralize them or to opsonize them for clearance by phagocytes that carry Fc-receptors. Furthermore, the Fc domain of antibodies can mediate complement activation, thereby inducing further pathogen opsonization and formation of a lytic membrane attack complex that results in elimination of the pathogen (Murphy and Weaver, 2016).

Heavy chain antibodies (hcAbs) and nanobodies (Nbs)

Distinct subclasses of IgG are found in Camelids including llamas, alpacas, vicuñas, guanacos, camels and dromedaries. In addition to the conventional IgG1, they produce heavy chain antibodies (hcAbs: IgG2, IgG3). In llamas, 55 to 75% of serum IgGs correspond to IgG1 and the remaining 25 to 45% correspond to IgG2 and IgG3 or hcAbs. These peculiar hcAbs lack light chains and the C_{H1} domain (Hamers-Casterman et al., 1993; Nguyen et al., 2002). Therefore, the antigen-binding site is reduced to a single variable domain designated single domain antibody (sdAb) or V_{HH} (variable domain of hcAbs) or nanobody (Nb), due to their small size of around 15 kDa.

This single variable domain is connected directly to the Fc domain through a hinge region (Fig. 3B). HcAbs with a long hinge belong to IgG2 subclass whereas IgG3 constitutes the short hinge subclass.

For a conventional antibody, the antigen-binding site or paratope is determined by the contribution of the variable domain of the heavy V_H and the light chain V_L and the structure of this binding surface is usually rather flat. In contrast, for a hcAb, the antigen-binding surface of the V_{HH} generally adopts a convex shape. This is attributed to the exceptionally long CDR3 regions of V_{HH} s (up to 26 residues) that structurally can build flexible finger-like salient extensions (Desmyter et al., 1996; Wesolowski et al., 2009). With these protrusions, Nbs can reach crevices, such as those displayed on ion channels or enzymes (Stortelers et al., 2018). Therefore, Nbs have an intrinsic propensity to block enzymatic or ion channel activity (Alzogaray et al., 2011; Danquah et al., 2016; De Genst et al., 2006; Koch-Nolte et al., 2007; Lauwereys et al., 1998; Rasmussen et al., 2011). A canonical disulfide bond connects the framework region FR1 and FR3 of V_{HH} s. An additional disulfide bond often stabilizes the enlarged CDR3 by linkage with either the CDR1 loop (in camels) or CDR2 loop (in llamas).

For a conventional antibody, the V_H domain carries hydrophobic amino acids to allow interaction with the V_L domain. Within V_{HH} s, hydrophilic amino acids are found at the equivalent positions. These substitutions make Nbs highly soluble (Fig. 3B). Besides, Nbs have demonstrated stability at extremes temperatures and pHs (Vu et al., 1997). Isolated Nbs can be produced as recombinant proteins with high yields either in *E. coli* as periplasmic proteins or in eukaryotic cells as secretory proteins (Holliger and Hudson, 2005; Wesolowski et al., 2009).

Having a 10-fold smaller size, Nbs preserve antigen-binding features. Moreover, their small structure helps them to easily penetrate through the endothelium into tissues, but also increases renal clearance. Owing to their simple structure, Nbs can be reformatted into multimeric molecules to increase avidity and specificities with the goal of increasing functional potency or cell-specific targeting and/or to increase their systemic half-life. Nbs can be also reconstituted into a hcAb of any desired isotype by genetically fusing the C-terminus to the hinge region of a conventional antibody, to allow desired Fc-mediated effector functions and also to increase their systemic half-life (Scheuplein et al., 2010; Tijink et al., 2008).

In virtue of the ability of nanobodies to have access to crevices on membrane proteins,

the Nolte lab at the University Medical Center in Hamburg in collaboration with Ablynx in Ghent generated P2X7-specific nanobodies following immunization of llamas. Some of these showed effective blockade of P2X7-mediated effects *in vitro* and showed benefit in two models of inflammatory diseases (see above, section 1.1.4) (Danquah, 2012; Danquah et al., 2016; Sun and Li, 2013).

1.3. The blood brain barrier (BBB)

The blood brain barrier (BBB) is a blood-tissue site of the central nervous system (CNS). It is composed by a monolayer of cerebral capillary endothelial cells sealed by a complex arrangement of tight junctions and surrounded by the basal lamina and the astrocytic endfeet. The interaction between these diverse cell types establishes a dynamic environment that maintains the BBB function, which is called the neurovascular unit (NVU). Physiologically, the BBB is a critical regulator of the brain homeostasis. Thus, it acts as a gateway between the plasma and the brain parenchyma for exchange of nutrients, metabolites, and hormones. Yet, it functions as a highly restrictive barrier preventing the access of molecules larger than 400 Da (Abbott et al., 2010) (Fig. 4A.).

Endothelial cells in the cerebral vasculature are different from peripheral endothelial cells. They possess an increased number of tight junctions that arrange in a more complex manner, thus restricting paracellular diffusion (Fig. 4A.). This tight junction structure consists of two critical components, occludins and claudins, as well as junctional adhesion molecules (JAMs) and endothelial selective adhesion molecule (ESAM). These proteins bind to zona occludens protein group (ZO), an adaptor molecule in the cytoplasm. Moreover, two other adaptor proteins, cingulin and 7H6 are in charge to establish communication between membrane junctional molecules and the cytoskeleton. A second junctional complex comprises vascular endothelial cadherin (VE-cadherin) and the platelet–endothelial cell adhesion molecule (PECAM). Moreover, brain endothelial cells have a low number of endocytic vesicles, limiting transcellular transport (Begley and Brightman, 2003).

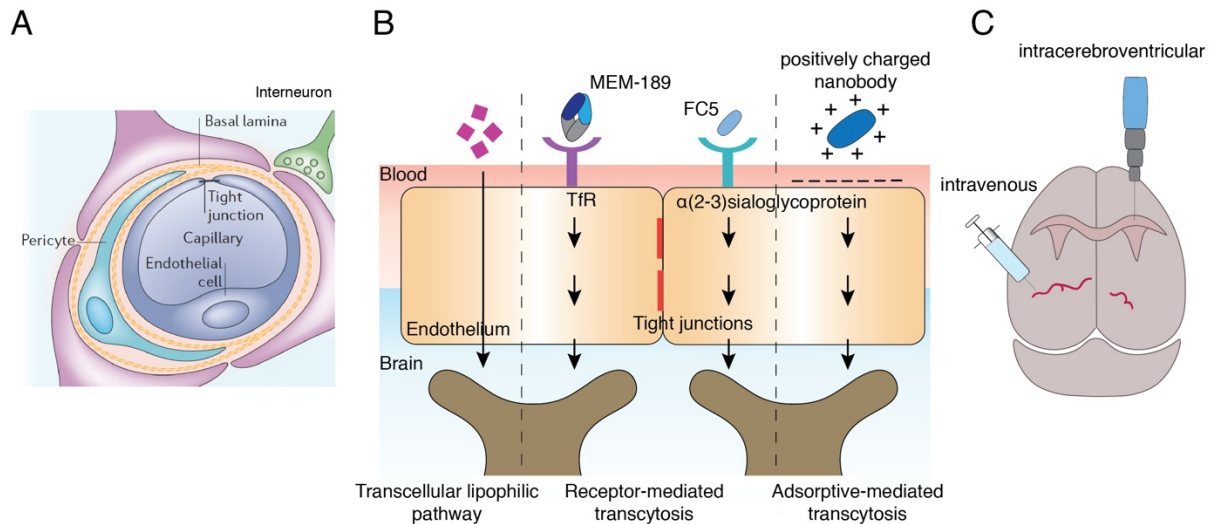


Figure 4. Components of the Blood brain barrier (BBB) and potential pathways for drug delivery to the brain. (A) The blood brain barrier (BBB) acts as a gatekeeper between the circulatory system and the extracellular space of the brain. It is formed by a monolayer of capillary endothelial cells sealed by tight junctions, surrounded by the basal lamina and astrocytic perivascular projections or end-feet. Astrocytes also provide a cellular link to neurons. **(B)** The BBB regulates the passage of molecules into the brain, lipid soluble molecules can permeate into the brain (transcellular lipophilic pathway), proteins such as transferrin (Tf) are actively endocytosed after binding to specific receptors (receptor-mediated transcytosis), and the uptake of some basic proteins is initiated by a charge interaction with the negatively charged BBB surface (adsorptive-mediated transcytosis). Drug delivery across the BBB may be possible by hijacking these pathways, e.g. using antibodies and nanobodies against transcytosis receptors (e.g. MEM-189, a Fab fragment specific for the Tf receptor (TfR) and FC5, a nanobody that binds α -sialoglycoprotein receptors). Protein cationization might increase uptake by adsorptive transcytosis. **(C)** Comparison between two routes of administration targeting the brain. The intracerebroventricular (icv) route bypasses the BBB, molecules are infused directly into the cerebrospinal fluid (CSF) that circulates from the ventricles to the brain parenchyma. In contrast, intravenously injected molecules encounter the BBB that restrict their passage into the brain parenchyma. Adapted from Astrocyte-endothelial interactions at the blood-brain barrier by (Abbott et al., 2006).

BBB transport mechanisms

Transport across the BBB involves passage through two membranes, the luminal and the abluminal membrane of the capillary endothelium; the latter is completely covered by the basement membrane and the astrocyte foot processes. This constitutes a barrier that restricts diffusion. Therefore, permeation of molecules by passive diffusion depends mainly on size. Small molecules with less than 500 Da of size cross the BBB through holes made by displacement of the phospholipid bilayer. Lipid solubility enhances passage of molecules through the BBB (Fig. 4B) (Fischer et al., 1998; Lipinski, 2000; Trauble, 1971).

Due to the presence of the tight junctions, the paracellular transport pathway is restricted (Brightman and Reese, 1969). Circulating molecules gain access to the brain parenchyma mainly via the transcellular route through the brain capillary endothelium. The transcellular pathway involves endogenous mechanisms that transport both small and large molecules and is classified in four systems: carrier-mediated transport (CMT), active efflux transport (AET), receptor-mediated transport (RMT) and adsorptive-mediated transcytosis (AMT). The CMT system comprises highly stereospecific pore-based transporters that mainly transport small molecule nutrients and determined structures are required for transporter affinity. An example is the glucose transporter type 1 (GLU1) (Crone, 1965). The AET system constitutes an active efflux transport system in the brain to the blood direction. It requires an energy-independent system at the luminal endothelial membrane and an energy-dependent transporter at the abluminal side of the capillary endothelium. An example for the first case is the solute carrier exchangers family (SLC) and for the second the ATP binding cassette transporters family (ABC) (Uchida et al., 2011). The RMT system mediates transport of large molecule, e.g. peptides and proteins (Fig. 4B.). Three types are described: i) the transferrin receptor (TfR) is an example of a bidirectional RMT. Thus, holo-transferrin engages the TfR at the luminal side of the endothelium, undergoes endocytosis and exocytosis into the brain interstitial fluid, this process is known as receptor-mediated transcytosis. Apo-transferrin undergoes reverse receptor-mediated transcytosis (Pardridge et al., 1987). ii) The neonatal Fc receptor (FcRn) serves to mediate reverse transcytosis of IgG from the brain to the blood (Schlachetzki et al., 2002). iii) An example of a unidirectional receptor-mediated endocytosis is the type 1 scavenger receptor (SR-VI) that is in charge of the uptake of low-density lipoprotein (LDL) from the blood into the endothelial cell but is not followed by exocytosis into the brain (Pardridge, 2012). Finally, the AMT route does not seem to involve specific receptors but is triggered by electrostatic interactions between polycationic molecules, such as peptides or proteins and negative charges on the membrane of the brain capillary endothelial cell (Fig. 4B.). Examples of the latter are the glycocalyx and the anionic microdomains of clathrin-coated pits along the membrane. Moreover, glycoprotein receptors containing multiple sialic acid residues, such as the TfR, concentrate in such pits, which may contribute to the negative charge (Herve et al., 2008).

Delivery of drugs to the Central nervous system (CNS)

The treatment of CNS disorders represents a challenge since the BBB restricts the delivery of therapeutics into the brain. Thus 98% of small and 99.9% of large molecule drugs are excluded from entering the brain (Pardridge, 2012). During CNS pathogenesis, BBB dysfunction may occur. In some conditions such as Alzheimer's disease, Parkinson's disease and epilepsy subtle changes in the BBB phenotype occur, whereas in multiple sclerosis, stroke, brain cancer, gross changes and loss of the structural integrity have been observed. In such cases, the delivery of the drug molecules may be facilitated (Abbott and Friedman, 2012).

Otherwise, multiple strategies have been explored to deliver drug molecules across the intact BBB (Fig. 4B). Increasing the lipid solubility can enhance penetration across the BBB, however this is restricted to molecules with a size under ~500 Da. Moreover, the penetration of such lipid soluble molecules across other biological membranes is also increased, which provokes a rapid clearance from the blood. Another strategy is to hijack the transcellular BBB transport. For instance, the structure of a small molecule drug can be altered to mimic a nutrient and thus undergo transport by the CMT system (Killian et al., 2007). Also, small molecule drugs conjugated to inhibitors of the AET system may allow better brain penetration (Hawkins et al., 2010). With respect to the RTM system; antibodies, antibody fragments or nanobodies raised against a transcytosis receptor can act as a molecular Trojan horse to shuttle drugs including both small and large molecules (Johnsen et al., 2017; Niewoehner et al., 2014). AMT-based drug delivery involves cationization of large molecule drugs such as antibodies, antibody fragments or nanobodies (Li et al., 2012; Li et al., 2016), as well as the use of cell-penetrating positively charged peptides as brain shuttles. Cationization, however, has limitations including enhanced toxicity, immunogenicity, and peptide instability (Herve et al., 2008) (Fig. 4B). The trans-nasal route of delivery is limited to small lipophilic drugs since the arachnoid membrane, which separates olfactory cerebro-spinal fluid (CSF) from the submucous space of the nose has a similar phenotype as the capillary endothelium of BBB (Kristensson and Olsson, 1971). Only small volumes can be infused without injury (Merkus et al., 2003). BBB disruption with vasoactive agents infused via carotid artery is another strategy to deliver drugs to the brain. These agents exert an osmotic pressure that shrinks the endothelial cell, thus inducing leakage of the BBB (Pardridge, 2005).

Recently, innovative delivery vehicles have been developed. A brain endothelial selective Adeno-associated virus (AAV)-based vector was developed with a novel *in vivo* screening system. In a mouse model of a hereditary monogenetic disorder, transduction of the endothelial-specific AAV vector encoding for the deficient gene restored the gene function and reversed the signs of the disease (Korbelin et al., 2016). Moreover, pre-clinical studies showed that drug-carrying liposomes enhanced delivery and showed benefit in two models of disease (Greenwood et al., 2017).

Intrathecal and intracerebral injections can also be used to bypass the BBB (Fig. 4C). Via the intrathecal or intracerebroventricular (icv) routes, drugs including antibodies can be infused directly into the CSF that circulates from the ventricles to the brain parenchyma (Calias et al., 2014). Owing to the high turnover rate of the CSF, intrathecally injected small molecules and protein therapeutics both typically exhibit a short half-life. Other neurosurgical procedures are also used to inject drugs directly into the brain parenchyma in a focal site. In any case, drug penetration depends on diffusion and drug concentration decreases with the distance from the injection site (Pardridge, 2005).

Targeting P2X7 in the CNS

As described above, the P2X7 ion channel is implicated in many CNS disorders (see sections 1.1.2 and 1.1.3). The literature describes some small and lipophilic P2X7 antagonists that efficiently cross the BBB. GSK1482160 show efficacy in two CNS rat models of chronic inflammatory pain: CFA-induced hypersensitivity in the knee-joint and constriction nerve injury-induced allodynia (Abdi et al., 2010). The Abbot lab reported a cyanoguanidine optimized led compound that reduced allodynia in a model of neuropathic pain and another brain penetrating candidate for pre-clinical studies that showed good potency of P2X7 blockade *in vitro* (Chrovian et al., 2014; Donnelly-Roberts et al., 2009). Merck optimized a P2X7 inhibitor that improved the pain score in three rat models of neuropathic pain, nevertheless, its conversion into toxic metabolites precluded further development (Brumfield et al., 2011). Pfizer developed three brain penetrating P2X7 antagonists. The first showed good receptor occupancy, especially in the cerebral cortex and colliculus (Able et al., 2011), the second showed good potency of P2X7 blockade (Chen et al., 2010). Both are candidates for pre-clinical

trials, unlike the third that showed a low potency of blockade (Chrovian et al., 2014). Janssen discovered a brain penetrating P2X7 antagonist with robust target occupancy, pre-clinical studies are pending (Letavic et al., 2013). Several of these brain-penetrating P2X7 small molecule drugs have shown toxic secondary effects. In addition, the lipidized form of these drugs is rapidly cleared from the blood. In the light of these setbacks, the development of biologics as more potent, selective, non-toxic antagonists that penetrate the brain presents a promising alternative.

P2X7-antagonistic nanobodies 13A7 and 1c81 developed in the Koch-Nolte lab have been shown to block P2X7 function with high potencies *in vitro* and *in vivo* (Danquah, 2012; Danquah et al., 2016). Moreover, they did not show adverse secondary effects and had a longer half-life than the lipophilic brain penetrating small molecule inhibitors. Since these nanobodies are potential translational biologics, they constitute candidates for optimization to increase brain penetration with the perspective of the development of therapeutics for P2X7-related CNS disorders. The Lafaye lab reported that nanobodies with a high isoelectric point (pI) crossed the BBB following intravenous administration and suggested that their transport across the brain endothelial cell is mediated by adsorptive mediated transcytosis (AMT) (Li et al., 2012; Li et al., 2016).

1.4. Goals of the project

The overall goal of this project was to engineer bivalent, half-life extended mouse P2X7-antagonistic nanobodies for targeting P2X7 on microglia *in vivo*. Specific goals were:

- i) to increase the pI and the stability of nanobody 1c81 by site directed mutagenesis,
- ii) to increase the binding avidity and the *in vivo* half-life of nanobodies 1c81 and 13A7 by dimerization and genetic fusion to an albumin-specific nanobody,
- iii) to determine the potency of the generated nanobody constructs to block ATP-mediated Ca^{+2} influx and IL1- β release by P2X7-expressing cells,
- iv) to develop a flow cytometric assay to detect and quantify the *in vivo* occupancy of P2X7 on microglia and T cells by nanobodies following their intravenous, intracerebro-ventricular, or intracerebral injection,
- v) to develop an ELISA assay to detect and quantify unbound nanobodies in serum following intravenous or intracerebro-ventricular injection,
- vi) to determine the *in vivo* potency of injected nanobodies to block ATP-mediated DAPI uptake by microglia, and
- vii) to determine the level of P2X7 occupancy on microglia achieved by nanobodies produced *in vivo* by AAV-transduced muscle cells.

2. Materials and Methods

2.1 Materials

Equipment	Model/Type	Company
Analytical scale	Analytical Plus	Ohaus
Autoclave	Modell 2540 EL	Tuttnauer Europe
Centrifuge	Rotanta 460 R	Hettich
Cell Imaging System	Evos ® FL	Thermo Fisher Scientific
CO ₂ Incubator	MCO-20AIC	anyo Electric Co.
ELISA plate reader	Victor3 1420	Perkin-Elmer
Dissociator	GentleMACS™	Miltenyi Biotec
Flow cytometer	FACSCelesta	BD Biosciences
Flow cytometer	FACSCanto II	BD Biosciences
Freezer	HFC 586 Basic	Heraeus
Heat block	Thermomixer Compact	Eppendorf
Horizontal electrophoresis system for agarose gels	40-0708	Peqlab biotechnology
Laminar Flow Hood	Gelaire Typ BST6	Gelman
Liquid nitrogen tank	K series	Taylor-Wharton
Magnetic stirrer	RCTS 26	OmniLab
Micropipettes	Research Type	Eppendorf
Microwave	M 637 EC	Miele
Neubauer cell chamber		LaborOptik
pH meter	Toledo MP220	Mettler
Photometer	Nanodrop 2000c	Peqlab biotechnology
Pipette Controller	Pipetboy	Integra
Power supply for agarose gel electrophoresis		Biometra
Power supply for SDS-PAGE	PowerPac 200	BioRad
Roller	Mixer SRT6	Staurt

Equipment	Model/Type	Company
Scanner	CanonScan 9800F	Canon
Shaker incubators	HT INFORS	Unitron
Sterile work bench	BSB4	GELAIR
Tabletop centrifuge	5424	Eppendorf
Thermal Cycler	T3/T Gradient	Biometra
UV-Transilluminator	Type TI 1	Biometra
Vertical electrophoresis system for SDS-PAGE	Xcell SureLock MiniCell	Thermo Fisher Scientific
Vortex		Labnet
Water bath	Type 1007	Labortechnik
Weigh Scale	Scout Pro	Ohaus

Consumables	Type	Manufacturer
Cell Culture well-plate	various sizes	Thermo Fisher Scientific
Cell culture flask	T-25, T-75, T-225	Greiner bio one/Nunc™
Cell sieves	70 µm, 40 µm	Falcon
Erlenmeyer flask	various sizes	PP Corning Inc
FACS tubes	various sizes	BD Biosciences
Falcon tubes	15 ml, 50 ml	Greiner
Gloves	Nitratex	Ansell
Microcentrifuge tubes	various sizes	Eppendorf
Nunc 96 well-plate	Nunc™ MaxiSorp	Thermo Fisher Scientific
Nunc 96 well-plate	Optical bottom Nunc™	Thermo Fisher Scientific
Pipette tips	various sizes	Eppendorf
Petri dishes	various sizes	Thermo Fischer Scientific
Scissors, forceps, scalpels	various sizes	FST Fine science tools
SDS-PAGE gels	10% and 12% NuPAGE	Invitrogen
SDS-PAGE gels	10% and 12% NuPAGE	Invitrogen
Serological pipettes	various sizes	BD Falcon
Sterile filtration	Steriflip, Stericup	Millipore
Syringes and needles	various sizes	Braun/BD Biosciences

Chemicals	Manufacturer
4',6-Diamino-2Phenylidole, Dihydrochloride (DAPI)	Thermo Fisher Scientific
Aqua ad iniectabilia	Braun
ATP, sodium salt	Sigma-Aldrich/Merck
Basal Medium Eagle (BME)	Gibco™ /Thermo Fisher Scientific
Blasticidin	Invivogen
β-mercaptoethanol	Gibco™
Bovine serum albumin (BSA)	Sigma-Aldrich/Merck
Carbenicillin	Sigma-Aldrich/Merck
Collagenase A	Sigma-Aldrich/Merck
Collagenase D	Roche
Dimethyl sulfoxide (DMSO)	Sigma-Aldrich/Merck
DMEM medium	Gibco™ /Thermo Fisher Scientific
DNA Gel loading Dye, 6x	New England Biolabs
DNA Typing Grade Agarose	Gibco™ /Thermo Fisher Scientific
DNase I (D) 600 U/mg	Roche
DNase I (D) 3000 U/mg	Worthington biochemical corporation
Ethylenediaminetetraacetic acid (EDTA)	Sigma-Aldrich/Merck
Fetal calf serum (FCS)	Gibco™ /Thermo Fisher Scientific
Fluo4, AM Cell permeant	Thermo Fisher Scientific
Glycerol	Sigma-Aldrich/Merck
Hank's Balanced Salt Solution	Gibco™ /Thermo Fisher Scientific
HEPES, 1 M	Gibco™ /Thermo Fisher Scientific
HIS-Select Nickel Affinity Gel	Sigma-Aldrich/Merck
IEF anode buffer	SERVA
IEF cathode buffer	SERVA

IEF sample buffer	SERVA
IgG Elution butter pH 2.8	Thermo Fisher Scientific
Imidazole	Sigma-Aldrich/Merck
Isoflurane	Sigma-Aldrich/Merck
LB Agar	BD Difco
LB Broth	BD Difco
L-Glutamine, 200 mM	Gibco™ /Thermo Fisher Scientific
L-Histidine	Sigma-Aldrich/Merck
Lipopolysaccharide (LPS), 500x	Sigma-Aldrich/Merck
MEM, non-essential amino acids, 10 mM	Gibco™ /Thermo Fisher Scientific
Nigericin Sodium Salt	Sigma-Aldrich/Merck
NuPAGE™ LDS Sample Buffer, 4x	Invitrogen/Thermo Fisher Scientific
NuPAGE™ Sample Reducing Agent, 10x	Invitrogen/Thermo Fisher Scientific
Papain	Sigma-Aldrich/Merck
Paraformaldehyde (PFA)	Sigma-Aldrich/Merck
Penicillin-Streptomycin	Gibco™ /Thermo Fisher Scientific
Percoll™, 1,130 g/ml	GE Healthcare
Phosphate buffered saline (PBS)	Gibco™ /Thermo Fisher Scientific
Phosphoric acid	Sigma-Aldrich/Merck
Polyethylenimine (PEI), MW 25000	Polysciences, Inc.
Prolong Diamond Antifade Mountant with DAPI	Thermo Fisher Scientific
Protein A Sepharose 4 Fast Flow	GE Healthcare
RPMI 1640	Gibco™ /Thermo Fisher Scientific
Saponin Quillaja	Sigma-Aldrich/Merck
SOC-medium	Sigma-Aldrich/Merck
Sodium Chloride, 0.9%	Braun
Sodium pyruvate, 100 mM	Gibco™ /Thermo Fisher Scientific
Sucrose	Sigma-Aldrich/Merck
TAE-Buffer Ultra-pure DNA Typing Grade, 50x	Thermo Fisher Scientific
TMB substrate	Pierce
Trichloroacetic acid	Sigma-Aldrich/Merck
Trypsin, 10x	Invitrogen/Thermo Fisher Scientific
Tween-20	Sigma-Aldrich/Merck
Violet 17 Dye	SERVA

Eukaryotic cell culture media

Composition

Complete BME	BME medium 250 000 U/ml Penicillin-Streptomycin 10 % FCS
Complete DMEM	DMEM medium 2 mM L-Glutamine 1 mM Sodium pyruvate 10 mM HEPES 1x NEM (non-essential amino acids) 5 % FCS

F17 Complete medium	FreeStyle™ F17 Expression medium 4 mM L-Glutamine 1% FCS 0.5% G418
F17 Feeding Medium	F17 Transfection medium 20% (w/v) Tryptone N1
F17 Transfection medium	F17 Expression medium 4 mM L-Glutamine 0.1% Pluronic
Hank's Balanced Salt Solution	HBSS solution 10 mM HEPES

Bacteria culture media

Composition

LB-Agar	10 g/L Tryptone 5 g/L yeast extract 10 g/L NaCl 15 g/L Agar-agar (pH7)
LB-Medium	10 g/L Tryptone 5 g/L yeast extract 10 g/L NaCl (pH7)
SOC-Medium	8.6 mM NaCl, 2.5 mM KCl, 20 mM MgSO ₄ 20 mM Glucose 2% Tryptone, 0.5% yeast extract

Buffer

Composition

Agarose gel electrophoresis	
Sample buffer 6x	2.5 % Ficoll-400 11 mM EDTA 3.3 mM Tris-HCl 0.017 % SDS
Tris Acetate EDTA Buffer (TAE) 50x	2 M Tris-Acetate 50 mM EDTA in deionized water

Cell preparation

ACK erythrocyte lysis buffer	155 mM NH ₄ Cl 10 mM KHCO ₃ 0.1 mM EDTA pH 7.2 in deionized water
------------------------------	--

Density gradient solution brain	30% Percoll v/v in deionized water
Density gradient solution kidney	40% Percoll v/v in deionized water
Digestion solution brain	DMEM 1 mg/ml Collagenase A 20 U/ml DNase I
Digestion solution kidney	RPMI 0.25 mg/ml Collagenase D 10 U/ml DNase I 5 % FCS
Cell Transfection	
NaCl 300 mM	300 mM NaCl in deionized water
PEI (Polyethylenimine)	7.5 mM 25 kDa linear polyethylenimine 0.333 mg/ml in deionized water at 60°C
ELISA	
Antibody Diluent	1% BSA in PBS
Blocking Buffer	2% BSA in PBS
Stop Solution	0.5 M H ₂ SO ₄
Washing Buffer	0.05% Tween-20 in PBS
Flow Cytometry	
FACS Buffer	0.02% BSA 1 mM EDTA in PBS -/-
Fixation Buffer	2% and 4% PFA in PBS
Protein Purification	
Elution buffer Ni-NTA	50 mM Na ₃ PO ₄ 0.3 M NaCl 250 mM Imidazol (pH 8.8)
Histidine Sucrose Buffer (HSB)	20 mM L-Histidine 0,02% Tween 8% sucrose in deionized water (pH 6.5)
IgG Elution Buffer Protein G	Thermo Fisher Scientific (pH 2.8)
Neutralization Buffer Protein G	1 M Tris (pH 9)
SDS-PAGE	
MES Running Buffer	50 mM MES 50 mM Tris Base 1% SDS 1 mM EDTA (pH 7.3)

Nu PAGE™ LDS Sample Buffer 4x Lithium dodecyl sulfate (pH 8.4)

Nu PAGE™ Sample Reducing Agent 10x 500 mM Dithiothreitol (DTT)
Nu PAGE™ LDS Sample Buffer (4x) Lithium dodecyl sulfate (pH 8.4)

DNA standards**Manufacturer**

GeneRule, 1kB
SmartLadder

Thermo Fisher Scientific
Thermo Fisher Scientific

Protein standards**Manufacturer**

Supermark

Self-made
100 µg/ml BSA
75 µg/ml IgG

Polymerases**Manufacturer**

KOD Hot Start
Pfu Turbo

Novagen
Agilent Technologies

Restriction enzymes**Manufacturer**

BamHI
DpnI

New England Biolabs
New England Biolabs

Plasmid**Specifications**

pCSE2.5_mlgG2cD265A

Variant of pCSE2.5 vector with a mouse IgG2cD265A sequence flanked by a NotI and XbaI restriction sites.

pCSE2.5_His-myc

Variant of pCSE2.5 vector with a hexahistidine tag followed by a c-myc tag flanked by NotI and XbaI restriction sites.

pCSE2.5_SNB

Variant of pCSE2.5 vector with two copies of the SNB tag followed by a c-myc tag flanked by NotI and XbaI restriction sites.

Kit**Manufacturer**

BCA™ Protein Assay kit
Mousse IL1-β ELISA
Nucleo Spin® Gel and PCR Clean-up
Plasmid Maxi Kit
Plasmid Mini Kit

Pierce
Invitrogen Thermo Fisher Scientific
Macherey Nagel
Qiagen
Qiagen

Antibodies

Antigen	Conjugate	Clone	Manufacturer
ASC	unconjugated	rabbit polyclonal IgG	Santa Cruz
CD45	APC-Cy7	30-F11	BioLegend
CD45	PerCP	30-F11	BioLegend
CD11b	APC	M1/70	eBioscience
CD4	BV605	RM4-5	BioLegend
CD16/CD32 (FcγR3/2 block)	unconjugated	2.4G2	BioXCell
CD45	AF700	30-F11	eBioscience
CD4	APC	RM4-5	BioLegend
CD69	FITC	H1.2F3	BD
CD8	BV650	53-6.7	BioLegend
c-myc tag	AF647	9E10	Nolte
Mouse IgG1	BV421	RMG1-1	BioLegend
Mouse IgG2c	biotin	RM223	Dianova
Nanobody	unconjugated	ABH-0077	Ablynx
Nanobody	biotin	ABH-0074	Ablynx
Nanobody	unconjugated	R345 (rabbit polyclonal IgG)	Ablynx
Rabbit IgG (H+L)	PE	none	Dianova
Rabbit IgG (H+L), Fab2	Poly HRP 40	none	Fitzgerald
Streptavidin	Poly HRP 80	none	Fitzgerald
Streptavidin	BV421	none	Biolegend

Prokaryotic cells

XL-2 Blue E. coli	Stratagene
-------------------	------------

Eukaryotic cell lines

HEK293T, untransfected	received from Dr. Carol Stocking (HPI)
HEK293_mP2X7	stably transfected with murine P2X7 (AG Nolte)

Mouse strains

C57BL/6 wt, P2X7KO	UKE, Hamburg
BALB/c wt, P2X7KO	UKE, Hamburg

oligonucleotides

Primer name	Description	Sequence (5'-3')
Not-SNB-SNB-stop-Xba_f	2x SNB-tag replacing primer in pCSE 2.5 forward	GGCCGCACCCAGACCCAGC AACAAAGAGACTGCAGCAGC CCAGACCCAGCAACAAGAG ACTGCAGCAGTGATAAT
Mut-1c81-Q8K_f	1c81 Q8K mutagenesis primer forward	ATGTCCGAGGTGAAATTGGT GGAGTCT
Mut-1c81-Q8K_r	1c81 Q8K mutagenesis primer reverse	AGACTCCACCAATTTACCT CGGACAT
Mut-1c81-Q127K_f	1c81 Q127K mutagenesis primer forward	AACTACTGGGGCAAGGGGA CCCAGGTC
Mut-1c81-Q127K_r	1c81 Q127K mutagenesis primer reverse	GACCTGGGTCCCCTTGCCC CAGTAGTT
Pci-Nbl	Amplification Nbl, insertion PciI site primer forward	GCGCACTACATGTCCGAGG TGCAATTGGTGGAGT
Nbl-20GS-BamHI_rev	Amplification Nbl, insertion 20GS linker, insertion BamHI site, primer reverse	ATGTCCGAGGTGAAATTGGT GGAGTCT
BamHI-15GS-NbII_for	Amplification NbII, insertion BamHI site, insertion 15GS linker, primer forward	ACGCGGATCCCCCGCCACC GCTGCCTCCACCGCCGCTA CCCCCGCCACCGCTGCCTC CACCGCCTGAGGAGACGGT GACCTG
BGH_rev	Sequencing pCSE 2.5, amplification Nb dimer, primer reverse	TCTTGGATCCGGCGGTGGA GGCAGCGGTGGCGGGGGT AGCGGCGGTGGAGGAAGCA TGTCCGAGGTGAAATTG
CMV_fn	Sequencing pCSE 2.5, primer forward	TAGAAGGCACAGTCGAGG

2.2 Methods

2.2.1 Molecular biology methods

Polymerase chain reaction (PCR)

Polymerase chain reaction is a technique to amplify a determined segment of DNA by thermal cycling. Thus, a double stranded DNA-template is denatured to single strands at high temperatures between 90°C to 95°C. Then, the temperature is lowered between 50°C to 65°C to allow oligonucleotides to anneal to the complementary strands of the targeted DNA sequence, thereby flanking the segment that will be amplified. The polymerase incorporates deoxyribonucleotide triphosphates (dNTPs) to the 5' end of the flanked DNA and builds a copy in the 3' direction. This step is called elongation and is performed at temperatures between 69°C to 72°C. The annealing and elongation steps are repeated in many cycles, throughout which newly synthesized DNA fragments become a template for further amplification. The polymerase requires buffers with MgCl₂ for optimal performance. PCR reactions were used for amplification of DNA fragments, site-directed mutagenesis of plasmid DNA, incorporation of restriction sites as well as peptide linkers and tags. The following PCR reactions were used in this project:

Table 1. PCR reaction with KOD polymerase.

Reagent	Volume (μ l)	Final concentration
10x Buffer for KOD polymerase	5	1x
dNTPs (2 mM)	5	0.2 mM
MgSO ₄ (25 mM)	2	1 mM
Forward primer (10 μ M)	2	400 nM
Reverse primer (10 μ M)	2	400 nM
KOD DNA polymerase	1	0.02 U/ μ l
DNA (app. 1 ng)	x	
ddH ₂ O	up to 50 μ l	

Table 2. Standard PCR amplification.

Reaction steps	Temperature (C°)	Time (s)	Cycle
First denaturation	95	120	1
Denaturation	95	30	
Annealing	50-65	15	30
Elongation	70	20-30/kb	
Final elongation	70	300	
On hold	4	∞	

Table 3. Mutagenesis PCR reaction.

Reagent	Volume (μl)	Final concentration
10x Buffer for PfuTurbo high fidelity polymerase	5	1x
dNTPs (2 mM)	5	0.2 mM
Forward primer (100 ng/μl)	1.25 μl	125 ng
Reverse primer (100 ng/μl)	1.25 μl	125 ng
PfuTurbo high fidelity HF	1	2.5 U/μl
plasmid DNA (50 ng/μl)	x	
ddH ₂ O	up to 50 μl	

Table 4. Mutagenesis PCR amplification.

Reaction steps	Temperature (C°)	Time (s)	Cycle
First denaturation	95	60	1
Denaturation	95	30	
Annealing	55	60	16
Elongation	68	240	
Final elongation	68	300	
On hold	4	∞	

Agarose gel electrophoresis of DNA fragments

DNA fragments were separated according to their size by agarose gel electrophoresis. Agarose matrices of 1.5% were prepared in 50 or 100 ml Tris Acetate EDTA (TAE) Buffer with 2.5 or 5 μl of Roti®-Gel stain (Carl Roth GmbH + Co KG), respectively.

Samples were dyed with loading buffer (Thermo Fischer Scientific) for visual tracking during migration and a DNA ladder was used for a comparative analysis of the size of the bands. The migration was performed at 60 – 90 V for 40 – 50 minutes. Using a UV-transilluminator with Video-Image system (BioVision 3000), DNA bands were visualized and photographed for documentation. For purification, a simple UV-transilluminator (Type T1, Biometra) was used for visualization and excision of the bands.

DNA extraction from agarose gel

PCR products or restricted DNA fragments were excised from agarose gels and purified using the PCR clean-up and Gel extraction kit from Macherey Nagel following the manufacturer's protocol. In some cases, PCR products were directly purified. The DNA was eluted with 15 μ l of sterile deionized water.

DNA enzymatic restriction

Enzymes or endonucleases cleave double stranded DNA at determined palindromic sequences. With the aim of cloning, DNA fragments were restricted using the appropriate enzymes and corresponding buffers at the optimal temperature according to the instructions of the manufacturer (New England Biolabs). The restriction conditions and heat inactivation of enzymes was selected using the online tool 'Double Digest Finder' from New England Biolabs (NEB). The restriction reaction was performed in a volume of 20 to 30 μ l considering that 1U of endonuclease cleaves 1 μ l of DNA. The restriction and heat inactivation temperatures were set up in a thermocycler.

Transformation of chemically competent bacteria

Chemically competent bacteria *E. coli* XL-2 Blue (Stratagene) were transformed with plasmid DNA by heat shock. A 100 μ l vial of bacteria stored at -80°C was slowly thawed on ice. Either 1-10 ng of plasmid DNA or ligation product was added to the cells and allowed to incubate for 30 min. The cells were then heat shocked by immersion in a 42°C water bath for 30 s followed by a 2 min incubation on ice. Finally, 900 μ l of pre-warmed SOC medium (37°C) was added and the cell suspension was incubated under shaking at 37 °C for 1 h. Cultures of transformed cells were seeded onto LB agar plates

containing appropriate antibiotics under sterile conditions. Plates were incubated at 37°C overnight and analyzed for presence of clones.

Cultivation of bacteria cultures for plasmid DNA preparation

To carry out a small- or large-scale plasmid preparation, bacteria cultures of either 5 ml or 100 ml of LB containing carbenicillin were inoculated with single clones picked from the transformation plates. Cultures were then incubated overnight at 37°C under shaking. The next day, cells were harvested by centrifugation at 4600 rpm for 20 min and supernatants were discarded. Plasmid DNA was extracted from the cell pellet using QIAprep® Spin Miniprep or Maxiprep Kits (Qiagen) following the manufacturer's protocol.

Quantification of DNA

The concentration of double-stranded DNA was estimated by measuring the absorbance of DNA at 260 nm using the spectrophotometer 'Nanodrop 2000c' (Thermo Fisher Scientific). The absorbance is measured at a wavelength of 260 nm (A_{260}), where DNA displays the peak of light absorption. The DNA concentration was calculated using the conversion relationship A_{260} of 1 = 50 $\mu\text{g/ml}$ of double stranded DNA. Since contaminants such as proteins that absorb light at 280 nm can be present in the DNA preparation, the ratio between A_{260} divided by A_{280} was used to evaluate the DNA purity. Values of $A_{260}/A_{280} = 1.7 - 2.0$ were considered as high quality of the DNA preparation.

Ligation of DNA fragments

Ligation allows the generation of recombinant DNA plasmids. Ligation reactions were performed with the T4 ligase (New England Biolabs) in the corresponding T4 buffer following the recommendations of the manufacturer. The ligase catalyzes the formation of a covalent bond between the complementary ends of a restricted DNA fragment and a restricted vector backbone. Ligation reactions were performed in a final volume of 20 μl using the molar ratio 1:3 of vector backbone to insert. The reactions were incubated either at 16°C overnight or at room temperature (RT) for 3 h. The enzyme was heat-inactivated at 65°C for 10 min.

DNA sequencing

For sequencing of DNA samples, the services of Seqlab (Göttingen) and Eurofins (Ebersberg) were used. Seqlab required 500 - 700 ng of DNA with 20 pmol of sequencing primer in a total volume of 7 μ l of sterile deionized water. For sequencing performed by Eurofins, 50 - 100 ng / μ l of DNA were submitted in a volume of 17 μ l sterile deionized water containing 10 μ M sequencing primer. The DNA sequences were analyzed with the program 4Peaks (Nucleobytes).

Gene synthesis

Gene synthesis is a methodology that permits the generation of artificial double stranded DNA fragments without the need of a pre-existing DNA template as starting point. Approaches are based on chemical synthesis of oligonucleotides and therefore, there is no limitation in the size or type of nucleotide. The desired nucleotide sequence was designed in silico, flanked by appropriate restriction sites for sub-cloning into the expression vector pCSE2.5 and optimized for expression in human eukaryotic cells using the online tool 'Gene Optimizer TM' by Thermo Fischer Scientific. The same company synthesized the DNA fragments and provided them cloned into the pMA-T vector in a lyophilized form.

Cloning of nanobody expression constructs

The pCSE2.5 expression vector was kindly provided by Thomas Schirrmann, Univ. Braunschweig (Jager et al., 2013). In this vector, the nanobody coding sequence is flanked by NcoI and NotI restriction sites and followed by the coding sequence for a peptide tag or hinge and Fc domains, a stop codon, and an XbaI site. Dimeric half-life extended nanobodies were cloned by PCR (Danquah, 2012; Danquah et al., 2016). Thus, in a first PCR reaction, the desired nanobody was amplified using primers that introduced a NcoI restriction site at the 5'-end of the sequence and a 20 amino acid Gly-Ser linker followed by a BamHI site at the 3'-end. In a second PCR, the same nanobody was amplified using a primer that placed a BamHI site followed by a 15 amino acid Gly-Ser linker at the 5'-end and a NotI site at the 3'-end. The PCR products were double digested and subsequently connected via the linker in a three-step ligation into an empty pCSE2.5 backbone carrying the His6x-myc tag, that was previously restricted by compatible enzymes. In order to fuse the half-life extension module to a

dimeric nanobody construct, the coding sequence for the albumin-specific nanobody Alb8 was amplified by PCR using primers to introduce a NotI restriction site followed by a 9 amino acid Gly-Ser linker at the 5'-end of the sequence and a His6x-myc tag followed by a stop codon and XbaI restriction site at the 3'-end. This PCR product was double digested, and the resulting insert was cloned via NotI and XbaI into the pCSE2.5 vector carrying a dimeric nanobody construct. To generate the SNB tag (Schaffer et al., 2010) in a tandem duplicate, complementary oligonucleotide sequences of two copies of the SNB tag followed by a stop codon were designed in silico. These overlapping were flanked by NotI and XbaI restriction sites. After denaturation and hybridization (2 min at 95°C, 2 min at 37°C) these oligonucleotides generated a double stranded insert that was ligated into the pCSE2.5 backbone, previously digested with NotI and XbaI. Nanobody 1c81-dim^{sh} HLE was designed in silico, chemically synthesized by Thermo Fischer Scientific and sub-cloned into the pCSE2.5 vector carrying a tandem SNB-tag. Nanobody 1c81-dim^s HLE was cloned and produced by Ablynx. Following restriction digestion of nanobody 13A7 with NcoI and NotI, the resulting insert was cloned into the pCSE2.5 backbone bearing the sequence of mouse IgG2c with the mutation D265A.

Site-directed mutagenesis

Point mutations were introduced in the DNA sequence of nanobody 1c81 by PCR-mutagenesis. This technique allows site-specific mutation of any double stranded plasmid. Therefore, two oligonucleotide primers both carrying the desired mutations were designed. The PCR was performed using the pCSE2.5 vector with the inserted wildtype sequence of 1c81 as a template. During the amplification, the high-fidelity polymerase PfuTurbo incorporated the primers into both single DNA strands. Therefore, the resulting PCR product contained a mixture of mutated and non-mutated parental plasmid DNA. To remove the parental plasmid DNA, the PCR product was treated for 1 h at 37°C with the restriction enzyme DpnI, which specifically cleaves methylated DNA derived from a dam⁺ *E. coli* strain. The mutated plasmid DNA was then transformed into *E. coli* XL-2 Blue.

2.2 Cell biology methods

The culture of cells was performed under sterile conditions in a Laminar flow bench (Gelaire type BSB4). Media was purchased sterile and prepared solutions were sterilized either by filtration through a 0.22 μM filter using Stericup or Steriflip vacuum filter (Merck) or autoclaved at 121°C for 20 min.

Cell culture of eukaryotic cells

Adherent HEK293 cell lines were cultivated in complete DMEM medium with 5% FCS using T-25, T-75 and T-225 culture flasks with filter caps (Nunc™ EasYFlasks™, Thermo Fisher Scientific). Sub-cultivation or harvesting required washing of cells with PBS followed by a short incubation with a sufficient volume of trypsin (Invitrogen) to cover the surface of the flask. Addition of FCS-containing DMEM medium inactivated the trypsin and the cell suspension was centrifuged at 1200 rpm for 8 min. Cell pellets were resuspended in a suitable volume of medium and routinely split in a 1:3 - 1:5 ratio every two or four days according to the density. HEK293 cells stably transfected with mouse P2X7 were maintained by addition of 10 $\mu\text{g}/\text{ml}$ blasticidin (InvivoGen). Cells were cultured in a steam-saturated incubator at 37°C with 5% CO₂.

Determination of cell numbers using Neubauer chamber

A 10 μl aliquot of the cell suspension was diluted 1:10 with trypan blue (0.4% in PBS) to analyze cell viability. The determination of cell numbers was carried out using a Neubauer counting chamber (LaborOptik). For this chamber, the cell number per ml is calculated as follows: mean of the cell number in major quadrants $\times 10^4 \times$ dilution factor.

Cryopreservation of eukaryotic cells

For cryopreservation, approximately one million cells were resuspended in 1 ml chilled freezing medium (10% DMSO in FCS) and transferred into cryogenic vials (Nunc Cryotube™). Cells were gradually frozen by short-term storage at -80°C followed by long-term storage in liquid nitrogen.

Transient expression of nanobodies in HEK293-6E cells

Recombinant nanobodies cloned into the expression vector pCSE2.5 were produced by transient transfection of adherent HEK293-6E cells. HEK293-6E cells were cultured in Gibco™ FreeStyle F17 complete medium (Thermo Fisher Scientific) with 1% FCS using semi-adherent cell culture flasks (Nunc™ EasYFlasks™, Thermo Fisher Scientific). Before transfection, the culture medium was exchanged to transfection medium (FCS-free F17 medium). The cells were transfected with the DNA using the transfection reagent PEI (Polysciences Inc.). For the transfection of cells in a culture volume of 30 ml in a T-225 flask, a mixture of 20 µg of plasmid DNA and 80 µg of PEI was prepared in 150 mM NaCl, thoroughly mixed by vortex and incubated at RT for 20 min. The mixture was added dropwise to the cells and the cells were cultured at 37°C with 5% CO₂ in the incubator. Twenty-four hours after transfection, cells are supplemented with 500 µl of F17 feeding medium (20% w/v Tryptone). Five days later, supernatants with secreted proteins were harvested by centrifugation at 4000 rpm for 10 min and stored at 4°C. To obtain high yields, the production was scaled up to 90 ml.

Preparation of peritoneal macrophages

C57BL/6 mice were sacrificed by cervical dislocation. Using scissors and forceps, the skin overlying the peritoneum was removed to expose the inner skin lining the peritoneal cavity and 5 ml of an ice-cold solution of 0.5 mM EDTA in PBS were injected slowly into the peritoneal cavity. Following a short massage on the abdomen, the solution containing macrophages was withdrawn, transferred into a 15 ml tube and the volume was completed with RPMI 5% FCS. Cells pellets were collected by centrifugation at 1500 rpm for 5 min, resuspended in RPMI 5% FCS and immediately used in experiments. Peritoneal macrophages were prepared by Dr. Björn Rissiek, Dept. of Neurology, UKE.

Preparation of microglia-astrocyte co-cultures

Neonatal C57BL/6 mice were sacrificed by decapitation. Brains were dissected, placed onto petri dishes and immersed in ice-cold HBSS medium. Under the microscope, the olfactory bulb, cerebellum and meninges were removed using forceps. Then, a suspension from brain tissue in HBSS was prepared by mincing brain tissue with

scissors. The suspension was washed with HBSS by centrifugation at 1500 rpm for 5 min and the supernatant was carefully removed using serological pipettes. The cell pellet was resuspended in 4 ml of a digestion solution with 0.5 mg/ml papain (Sigma) and 10 μ g/ml DNase (Roche), dissolved in HBSS with 10 mM HEPES. Following a 30 min incubation at 37°C under shaking, the enzymatic reaction was stopped by addition of BME medium supplemented with 10% FCS and then, cell pellets were collected by centrifugation. Complete disruption of the cell pellet was accomplished by pipetting up and down 5 ml of 10% FCS-BME medium with a Pasteur pipette having a narrow opening diameter. The cell suspension was filtered through a 70 μ M strainer (EASY strainer, GBO), centrifuged and the cell pellet was resuspended in warm 10% FCS-BME medium. Five ml of this suspension were plated into T-75 flasks and filled up to 10 ml with 10% FCS-BME medium. Cells were cultured at 37°C with 5% CO₂ in the incubator for 21 days. Twice a week, cells were fed by exchanging an aliquot of the culture medium with fresh medium. After 21 days in culture, the cells differentiated in a mixture composed of 20-30 % microglia and 60-70% astrocytes. Microglia-astrocyte co-cultures were prepared with assistance of Mrs. Larissa Jank, Dept. Neurology, UKE.

Preparation of brain cells

Following nanobody administration to C57BL/6 or BALB/c mice and perfusion, brains were dissected, rinsed with PBS in 50 ml falcon tubes and placed into petri dishes. With a scalpel, the olfactory bulb and cerebellum were removed, and brains were immersed in 5 ml digestion solution in 50 ml falcon tubes, and then using scissors, brains were cut into small pieces. The resulting suspension was incubated under shaking at 37°C for 30 min and sieved through a 40 μ M cell strainer to dissociate the tissue (EASY strainer, GBO). The volume was completed up to 50 ml with FACS Buffer, sieved once again and centrifuged at 1500 rpm for 5 min. Brain cells were separated by density gradient centrifugation, therefore the cell pellet was resuspended in 5 ml of 30% Percoll in PBS and centrifuged at 1400 rpm at 14°C for 20 min without acceleration and deceleration. Three phases were distinguished: a brain cell pellet at the bottom followed by the Percoll solution and fat at the top. The fat was removed, the Percoll phase decanted and the cells were resuspended in 1 ml of Erythrocyte lysis Buffer (ACK). Following incubation at RT for 3 min, 10 ml of FACS Buffer were added

to stop the lysis and wash cells by centrifugation at 1500 rpm for 5 min. The pellet was then resuspended in 1 ml FACS Buffer and immediately used for experiments.

Preparation of kidney cells

Following nanobody administration to C57BL/6 or BALB/c mice and perfusion, kidneys were dissected and placed into petri dishes to remove fat and the adrenal glands using scalpel and forceps. Clean kidneys were then transferred to a gentleMACS™ tube filled with digestion solution and cut into small pieces using scissors. The tissue was dissociated in the gentleMACS™ dissociator. Thus, sample rotated for 15 min at 37°C followed by rapid whirl for 45 sec using manufacturer's program mSpleen1.01. Samples rotated further for 15 min at 37°C followed by final whirl for 45 sec using manufacturer's program mLung2.01). Cell suspension was transferred to a 15 ml falcon tube, the volume was completed up to 15 ml with PBS and sieved through a 70 μ M cell strainer (EASY strainer, GBO). The cell suspension was centrifuged at 1500 rpm for 5 min and the cell pellet was resuspended in 5ml of 40% Percoll in PBS. To separate renal cells, a density gradient was generated by centrifugation at 1400 rpm at 14°C for 20 min without acceleration and deceleration. Then, the Percoll phase was decanted and the cells resuspended in 3 ml of Erythrocyte lysis Buffer (ACK). After 3 min incubation at RT, 10 ml of FACS Buffer were added to stop the lysis and wash cells by centrifugation at 1500 rpm for 5 min. The pellet was then resuspended in 1 ml FACS Buffer and immediately use for experiments. Renal cells were prepared by Dr. Nicole Schwarz and Mr. Marten Junge, Institute of Immunology, UKE.

2.3 Immunology methods

Ca²⁺ influx assay

Mouse P2X7 stably expressing HEK cells were loaded with the Ca²⁺ indicator Fluo4 AM cell-permeant (Invitrogen™) at a final concentration of 4 μ M and incubated at RT for 20 min in the dark followed by a second incubation at 37°C for 15 min. The excess of dye was washed-out with PBS by centrifugation at 1500 rpm for 5 min. Cell pellets were resuspended in PBS containing Ca²⁺ and Mg²⁺ and transferred into a 96 well black-optical plate. Nanobodies were serially diluted using $\sqrt{10}$ as a dilution factor and 100 nM as initial concentration, and then incubated with the cells for 30 min on ice. An

ATP solution was added to a final concentration of 1.5 mM ATP and the intracellular Ca^{+2} was measured at 37°C every minute over 20 min by fluorimetry.

Inflammasome assembly assay (ASC speck detection) by microscopy

Mouse peritoneal macrophages from C57BL/6 mice were resuspended in RPMI and seeded onto poly-L lysine coated coverslips at a density of 300 000 cells/ml. To allow sufficient attachment, macrophages were incubated overnight at 37°C with 5% CO_2 in an incubator. Before experiment, all solutions were kept at 37°C. Cells were washed with RPMI, stimulated with a 1 $\mu\text{g}/\text{ml}$ LPS (Sigma) in RPMI at 37°C for 3,5 h and further incubated for 30 min in presence or absence of a nanobody solution in RPMI to a final concentration of 200 nM. Then, a solution of either ATP or nigericin (Sigma) was added to a final concentration of 1.5 mM or 10 μM respectively and following a 30 min incubation at 37°C, cells were fixed with 4% PFA, washed with PBS and permeabilized with permeabilization buffer. Cells were incubated with a 500-fold diluted primary rabbit α -ASC antibody (Santa Cruz) for 1 h and then stained with a 1:200-fold diluted secondary PE-conjugated α -rabbit antibody for 45 min. Both antibodies were diluted in permeabilization buffer and following each incubation time, 3 washing steps were carried out. Coverslips were mounted with the Prolong Diamond Antifade mounting medium containing DAPI and images were obtained by means of a fluorescence microscope equipped with a digital camera (EVOS, FL). ASC specks were quantified per field of vision containing at least 100 cells. Six fields of vision were counted per sample.

IL1- β release assay

In vitro differentiated mixed glial cultures were re-plated onto 12 well plates at a density of 3×10^5 cells/ml and cultured at 37°C with 5% CO_2 in an incubator. Three days after, cells were sequentially incubated at 37°C with LPS (1 $\mu\text{g}/\text{ml}$) (Sigma) for 4 h and then for 30 min with or without 1: $\sqrt{10}$ titrated nanobody solutions (top concentration 100 nM). An ATP solution was added to the cells to a final concentration of 1.5 mM and immediately after 30 min incubation at 37 °C, the plates were placed on ice. Cell supernatants were collected in clean Eppendorf® tubes and centrifuged at 5000 rpm for 10 min to remove cell debris. Clarified supernatants were stored at -20°C. The concentration of IL1- β in the supernatant was determined using the kit mouse IL1- β

ELISA (Invitrogen) following the instructions of the manufacturer. Thus, plates are coated with a capture antibody, incubated with either the cell supernatants or the mouse IL1- β standard and detected with a biotinylated detector antibody followed by a conjugate avidin-HRP that reacts with the substrate TMB giving a blue-colored product. The reaction was stopped with 0.5 mM H₂SO₄ and the absorbance was measured by photometry with Plate reader Victor 3 1420 (Pekin Elmer).

Flow cytometry

Flow cytometry is a powerful technique that is based on the passage of single cells in a liquid stream through a laser. The laser excites fluorescently labeled cells as well as certain cell components that emit an optical signal. This optical signal is processed by optical detectors coupled to photomultipliers converting these signals into electronic pulses that can be visualized and interpreted by software. Thus, flow cytometry allows a multiparametric analysis of the physical properties of cells such as size, cytoplasmic granularity as well as detection of cell antigens or markers present either in the surface or cytoplasm and nucleus. Usually, cells are labeled with fluorochrome-conjugated antibodies directed against cell surface antigens and intracellular antigens. The intensity of the fluorescent signal is proportional to the number of the targeted antigens. Fluorochromes are molecules that are excited by light sources such as laser and emit a fluorescent signal at a characteristic range of wavelengths. Interestingly, the fluorescent emission of some fluorochromes overlaps on the light spectrum; therefore, the primary signal that spills into the secondary one must be corrected. This process is called compensation and is calculated by the flow cytometry software. Flow cytometry was performed on FACS Canto II and Celesta (BD Bioscience).

P2X7 occupancy assay on microglia and renal T helper (Th) cells by in vivo administered nanobodies

P2X7 occupancy assay is determined by measuring the degree to which the administered nanobody binds to P2X7 *in vivo*. For the purpose of this project, dose response analyses of P2X7 occupancy on microglia and renal Th cells were carried out following administration of nanobodies *in vivo* by different routes. When injected bivalent half-life extended nanobodies, the experimental procedure is detailed as follows: Cell suspensions prepared from brain and renal tissue were incubated in

presence or absence of saturating nanobody (0.5 μg) at 4°C for 30 min. To remove the excess of nanobody, cells were washed twice with FACS Buffer by centrifugation at 1500 rpm for 5min. Cells were then incubated at 4°C for 30 min with 0.2 μg of mAb77, a mouse monoclonal IgG1 that recognizes the albumin-specific nanobody (Alb8) (Ablynx). After one washing step, brain cells were stained with a cocktail of fluorochrome-conjugated antibodies specific for microglial phenotypic markers (CD45, CD11b) and renal cells were stained with an antibody-mix specific for the following markers: CD45, CD8, CD4 and CD69. Both cocktails contained a BV421-conjugated α -mouse IgG1 antibody, in order to detect mAb77. After a 20 min incubation at 4°C, cells were washed with FACS Buffer, fixed with PFA 2%, resuspended in FACS Buffer and analyzed by flow cytometry using FACS Celesta. When injected bivalent Fc-fused nanobodies the procedure is basically the same as described above except for the detection of the P2X7-bound mouse IgG2c-fused nanobody. Thus, cells were stained with a biotinylated α -mouse IgG2c antibody followed by streptavidin BV421-conjugated.

Following transduction of AAV-encoding nanobodies the same procedure as above was performed.

P2X7 functional assay on microglia and renal T helper (Th) cells following in vivo administration of nanobodies

In parallel with the *in vivo* P2X7 occupancy assay, the effect of the nanobody bound *in vivo* to P2X7 on microglia and renal Th cells was analyzed. Hence, nanobody capacity to block P2X7 was assessed using the ATP-induced pore formation assay, which reflects the uptake of the DNA-staining dye DAPI into cells. Cells were treated as detailed above (2.2.3.5.), the sole difference is that the mix of fluorochrome-conjugated antibodies does not contain the α -mouse IgG1 antibody labeled with BV421 because this fluorochrome emit light in the same wavelength range as DAPI. Following staining, cells were washed with FACS Buffer, resuspended in RPMI and an ATP solution in RPMI was added to a final concentration of either 0.5 mM for brain cells or 0.125 μM for renal cells. Cells were then incubated at 37°C for 10 min, washed and resuspended in ice-cold FACS Buffer. Cells were immediately analyzed by flow cytometry using FACS Celesta.

Cell-based P2X7 binding assay

HEK cells stably expressing mouse P2X7 were trypsinized, washed with FACS Buffer by centrifugation at 1500 rpm for 5 min and incubated with 0.5 μ g of nanobody at 4°C for 30 min. Following a washing step, and when testing dimeric half-life extended nanobodies, binding to P2X7 expressing HEK cells was detected as detailed above (2.2.3.5.), using mAb77 followed by α -mouse IgG1 secondary antibody conjugated to BV421. When testing monomeric nanobodies carrying the c-myc tag, cells were stained with a c-myc tag specific antibody conjugated to AF647 at 4°C for 30 min, washed, resuspended in FACS Buffer and analyzed by flow cytometry using FACS Canto II.

Determination of the concentration of nanobodies in serum by ELISA

At the time of analysis of *in vivo* P2X7 occupancy assays, blood was drawn from the injected mice and collected into heparinized tubes. To sediment erythrocytes, blood was centrifuged at 4000 rpm for 10 min and the serum was transferred carefully into clean Eppendorf® tubes.

ELISA 96 well plates (Nunc™ MaxiSorp™) were coated overnight at 4 °C with 100 ng/well of mAb77, a mouse monoclonal IgG1 that recognizes the albumin-specific nanobody Alb8. Then, plates were washed 3 times with PBS-Tween 0.05% and blocked with 2% BSA in PBS at RT for 1 h. After 3 washing steps, plates were incubated at RT for 1 h with 100-fold serially diluted serum samples side by side with a standard of known nanobody concentrations. The standard was prepared by making $\sqrt{10}$ -fold serial dilution of the targeted purified nanobody starting with a concentration of 10 nM. Plates were then incubated at RT for 1 h with 100 ng/well of either the biotinylated mouse monoclonal antibody mAb74 or the rabbit polyclonal antibody pAbR345. Both antibodies were selected for binding to nanobodies and were provided by Ablynx. After 3 washing steps, the following HRP conjugates (1:5000 in PBS-BSA) were added to the plates for 1 h at RT: streptavidin poly-HRP (80) to detect biotinylated mAb74 and α -rabbit IgG (H+L) poly-HRP (40) to detect pAbR345. After 3 washing steps, the substrate TMB was added to the plates. 3-5 min after the formation of a visible blue-colored product, the reaction was stopped by the addition of 0.5 mM H₂SO₄. The optical density was measured by photometry with the plate reader Victor 3 1420 (Perkin Elmer).

2.2.3 Protein biochemistry methods

Immobilized metal affinity chromatography (IMAC)

Nanobodies carrying a His₆x-tag were purified by metal affinity chromatography (IMAC) using Ni-NTA resins. The separation is based on the formation of a covalent bond between Histidine and Ni⁺² ions from a charged resin (Sigma-Aldrich/Merck). This resin is built using NTA (Nitrilotriacetic acid) as a chelating agent to immobilized Ni into an agarose matrix. Harvested HEK cell supernatants containing the secreted proteins were loaded onto columns of Ni-NTA matrix and the flow-through was collected. For 90 ml of HEK cell supernatant, 2 ml columns were packed (for smaller or larger supernatant volumes column sizes were scaled up or down accordingly). The columns were then washed with 20 ml washing buffer to remove non-specifically bound proteins. The elution of bound proteins was accomplished by the addition of elution buffer containing 250 mM imidazole collecting four elution fractions. An aliquot of the HEK cell supernatant, flow through, wash and the elution fractions were size-fractionated by SDS-PAGE in order to analyze the purification process.

Immobilized affinity chromatography (protein A)

The Fc domain of conventional as well as heavy chain antibodies has an intrinsic affinity to protein A. Similarly, some nanobodies such as 1c81 and its variants bind to protein A with high affinity. The binding of nanobodies to protein A can be predicted by the presence of certain amino acids in the FR sequences and must be confirmed experimentally. The purification of these proteins from HEK cell supernatants was performed as above using protein A columns packed with the resin 4 Fast Flow Protein A sepharose (GE Healthcare).

Desalting and concentration of protein elution fractions

The collected elution fractions were desalted and concentrated using Amicon Ultra Centrifugal filter columns (Millipore) with suitable molecular weight cut-off. To this end, the elution fractions were pooled and transferred to the filter columns. By multiple cycles of centrifugation at 4000 rpm the Elution Buffer was exchanged to PBS or Histidine-Sucrose Buffer (HSB). The protein solution was then concentrated by further centrifugation. HSB is broadly used to provide high stability to antibody formulations

and does not alter the biophysical characteristics of the proteins (Baek et al., 2017). Nanobody 1c81 and its variants were stored in HBS buffer to maintain low aggregation levels.

Quantification of proteins

Protein solutions were quantified by means of the BCA protein assay kit (Pierce™, Thermo Fisher Scientific) following the recommendation of the manufacturer. The principle is based in the formation of a colored product that is directly proportional to the protein concentration. Thus, amino acids in the protein sequence such as Cysteine, Tyrosine and Tryptophane reduce Cu^{2+} ions in an alkaline solution. The reduced cations (Cu^{1+}) react with bicinchoninic acid (BCA) to form a purple-colored complex that absorbs light at 562 nm. The absorbance was measured using the photometer plate reader Victor 3 1420 (Perkin Elmer). The concentration was determined using a standard curve generated from known titrated amounts of bovine gamma globulins (BGG) (Pierce™).

Sodium dodecyl sulfate polyacrylamide gel electrophoresis

SDS-PAGE is an analytical method to separate proteins by their molecular weight under the influence of an electric field. The anionic detergent Sodium Dodecyl Sulfate (SDS) is used to denature proteins and to confer a negative net charge so that they migrate towards the anode in an electric field. All protein separations by SDS-PAGE were performed under reducing conditions. Therefore, the samples were mixed with a buffer containing SDS and 10% reducing agent (LDS sample Buffer, NuPAGE™) and incubated at 70°C for 15 min. Subsequently, the samples were loaded onto precast 10 - 12% NuPAGE Bis - Tris polyacrylamide gels (NuPAGE™). The protein electrophoresis was carried out in MES running Buffer (Invitrogen) at 200 V, 110 mA for 40 min.

Coomassie brilliant blue staining

Protein bands in SDS-PAGE gels were visualized by Coomassie blue staining. Coomassie brilliant blue is a non-polar anionic dye that binds proteins in a non-specific manner. The Novex® colloidal blue staining kit was used following the protocol provided by the manufacturer. Gels were stained overnight and the excess of dye was

removed by washing in deionized water. Gels were dried between cellophane foil for documentation using a drying solution (Gel-Dry, Novex®).

Non-equilibrium pH Gel Electrophoresis (NEPHGE)

Non-equilibrium pH gel electrophoresis (NEPHGE) is a technique to resolve proteins with acid isoelectric points as well as extremely basic isoelectric points. During NEPHGE, proteins migrate through the gel towards the cathode at different rates according to their isoelectric points (O'Farrell et al., 1977). Eight μg of purified proteins were mixed with IEF-sample Buffer (SERVA®) in a 1:1 ratio and loaded onto precast ampholytes-based gels suitable for the resolution of proteins in the pH range of 3.5 – 10 (SERVAGel™ IEF3-10). For NEPHGE, the polarity of the electrophoresis system was exchanged. Thus, the cathode and the anode buffers (SERVA®) were filled in the opposite chambers and these chambers were connected to the opposite electrodes. The migration of proteins by NEPHGE was carried out at 200V for 90 min. Then, gels were stained following the instructions of the manufacturer and all steps were performed under shaking. Gels were fixed in 20% (w/v) trichloroacetic acid for 30 min, stained with SERVA Violet 17 (SERVA®) for 10 min, rinsed shortly with deionized water and the unspecific staining was removed with 3% phosphoric acid. For proper preservation, gels were incubated overnight in 30% ethanol – 5% glycerol and dried in a drying solution (Gel-Dry, Novex®).

2.2.5 Animal experiments

Mice were bred at the animal facility of the UKE. All animal experiments and methods were performed in accordance with the relevant guidelines and regulations and with approval of the Hamburger Behörde für Gesundheit und Verbraucherschutz, Veterinärwesen/Lebensmittelsicherheit. Treatments of mice and preparation of cells from mice were performed with assistance of Dr. Nicole Schwarz and Marten Junge Institute of Immunology, UKE, Dr. Sahil Adriouch, Univ. Rouen, France, and Dr. Björn Rissiek and Dr. Ehsan Javidi, Dept. of Neurology, UKE.

Administration of nanobodies

For *in vivo* dose response analyses of P2X7 occupancy, $\sqrt{10}$ -fold nanobody dilutions were prepared either in PBS or HSB and administered to C57BL/6 or BALB/c mice via

the intravenous route. Following injection of 100 μ l of the nanobody solution circulation was allowed for 4 h, 18 h or 48 h depending on the experiment. Mice were intravenously injected with 2 μ g in 100 μ l of a fluorochrome-conjugated α -CD45 antibody. After 3 min, mice were terminally anesthetized before for perfusion.

Mice were anesthetized in an induction chamber with 4% isoflurane. After shaving the scalp, mice were mounted in the Hamilton stereotaxic apparatus. The head was fixed by placing very carefully ear bars into the ear canals and the nose was placed into a mask adaptor to maintain anaesthesia by inhalation of 1.7% of isoflurane. Before surgery an eye-ointment was applied to protect the eyes. Then, the skull was disinfected, and a 1.5 cm midline sagittal incision of the scalp was made in order to expose the periosteum. The syringe and needles were attached to the stereotaxic frame and the arm was adjusted to 1.1 mm laterally and 0.55 mm posterior to the bregma (intersection point of the sagittal suture with the anterior suture). At these coordinates, a 1 mm burr hole was drilled with a micro drill and simultaneously a saline solution was applied to dissipate the heat. A gaslight syringe was loaded with the nanobody solution and attached to the stereotaxic injector. The needle was advanced through the burr hole, 2.3 mm deep into the striatum and 5 μ l of the nanobody solution was injected over 5 min. The needle was left in place for 10 min to minimize backflow and then withdrawn slowly over 2 min. The scalp incision was sutured, and the mouse was transferred to a warmed chamber for recovery. Pre- and postoperative analgesics (1mg/ml tramadol) were administrated in the drinking water and if necessary 0.05 mg/kg of buprenorphine was injected subcutaneously. Intracranial surgical procedures were performed by Dr. Ehsan Javidi, Dept. Neurology, UKE. Nanobody-encoding AAV1 vectors were produced by Virovek, Hayward, USA. For muscle transduction, mice were anesthetized, hind legs were shaved and 10^{11} viral genomes in 50 μ l of PBS were injected per mouse in the gastrocnemius muscles. Muscle transductions were carried out by Dr. Sahil Adriouch, Univ. Rouen, France.

Transcardial perfusion

Once confirmed unresponsiveness of mice, they were fixed on an adapted shallow tray. To expose the heart, using curved blunt scissors and forceps, a first lateral incision beneath the rib cage was made, followed by an incision in the diaphragm and a large cut along the entire length of the rib cage up to the collarbone. Before perfusion,

blood was drawn by heart puncture. Immediately afterwards, a perfusion needle was placed into the left ventricle of the heart close to the ascending aorta and then, a small incision was made on the right atrium of the heart using iris scissors to make an outlet for the perfusion solution. When necessary, the heart can be clamped to secure the needle and prevent leakage. Immediately, the perfusion pump was enabled and 50 ml of a PBS solution containing heparin (10 U/ml) were infused at a rate of 10 ml/min.

3. Results

The results section is divided in three chapters. The first chapter describes the molecular engineering of P2X7-antagonistic nanobodies (Nbs) resulting in bivalent, half-life extended constructs with optimized physicochemical properties. Furthermore, their expression in a mammalian expression system was quantitatively and qualitatively analyzed and the physicochemical properties of the purified nanobodies such as purity, stability and isoelectric point (pI) were characterized. In the second chapter, the different nanobody formats were functionally characterized, focusing on the specificity and the potency to block gating of P2X7. In the third chapter, I describe a new technique to detect cell-bound nanobodies by flow cytometry. By this, we were able to measure at various time points the degree of P2X7 occupancy on microglia and renal T helper (Th) cells following systemic and intracerebro-ventricular administration of different doses of the engineered nanobodies. Furthermore, I evaluated the efficacy of the nanobody that bound *in vivo* P2X7, to block the ATP-mediated DAPI uptake. Finally, by AAV-mediated gene transfer technology, muscle cells were induced to continuously express engineered nanobodies *in vivo*, and the level of P2X7 occupancy and blockade on microglia and renal Th cells was evaluated six months after intramuscular injections of nanobody-encoding AAV.

3.1 Nanobody (Nb) engineering

This chapter describes the cloning, sequence optimization, and reformatting of P2X7-antagonistic nanobodies. Moreover, the production of the engineered nanobodies is qualitatively and quantitatively analyzed and the chemical characterization is performed. The nanobodies used in this study were previously generated in the Koch Nolte lab at the University Medical Center Hamburg-Eppendorf in collaboration with Ablynx, Belgium (Danquah, 2012; Danquah et al., 2016).

3.1.1 Cloning and reformatting of P2X7-antagonistic nanobodies

In order to generate nanobodies against the P2X7 ion channel, llamas were immunized either with P2X7-transfected HEK cells or by a cDNA-prime-protein boost strategy (Eden et al., 2017). Immunization with P2X7-encoding expression vectors allows the presentation of the antigen in its native conformation to the immune system. The

selection of nanobodies was performed by means of the phage display technology. Two rounds of panning on P2X7-expressing cells yielded, among others, nanobodies 13A7 and 1c81. 13A7 showed specific binding to mouse P2X7 (mP2X7) whereas 1c81 showed binding to both, mP2X7 and human P2X7 (hP2X7). Both nanobodies effectively blocked gating of P2X7 ion channel (Danquah, 2012) and 13A7 showed therapeutic benefit in experimental glomerulonephritis and allergic contact dermatitis (Danquah et al., 2016).

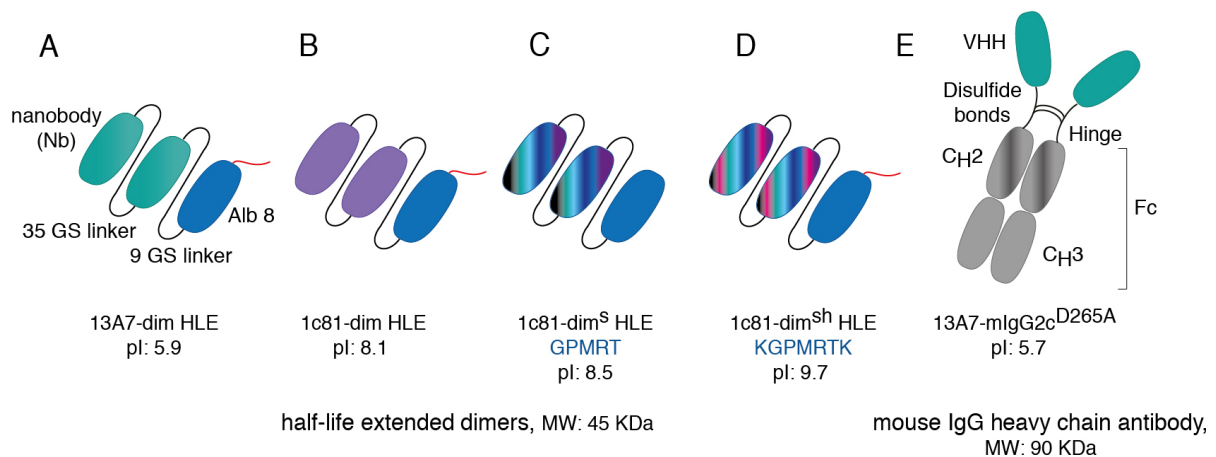


Figure 5. Schematic diagram of bivalent, engineered, half-life extended P2X7-antagonistic nanobodies. Homodimers (dim) of mouse P2X7-antagonistic nanobodies 13A7 (light green) **(A)** and variants of 1c81 (colored) **(B-D)** are fused to an α -Albumin nanobody, Alb8, resulting in bi-specific heterotrimeric nanobodies with an extended half-life (HLE). Nanobody domains are connected through a 35 or 9 Gly-Ser peptide linker (black curved line). Mutations (GPMRT) that provide stability to 1c81 are shown by colored stripes (1c81^s) **(B-D)**. Additional mutations (KK) that increase the isoelectric point (pI) are depicted by pink stripes (1c81^{sh}) **(D)**. In **(E)** the reconstituted 13A7 (light green) mouse IgG2c heavy chain format (13A7-Fc) is shown, a black bent line represents the hinge region and the CH2 and CH3 domains of the Fc region are depicted in grey. The CH2 domain carries the mutation D265A that abolish binding to the Fc γ receptors and it is illustrated by dark gray stripes. C-terminal tags in A, B and D are indicated by a red curved line. Dimeric HLE 13A7 and 1c81 carry the His6x followed by the c-Myc tag **(A, B)** and 1c81-dim^{sh} HLE **(D)** bears two copies of the SNB tag. The approximate molecular weights of a single nanobody domain, HLE-dimer, and heavy chain antibody are 15 kDa, 45 kDa, and 90 kDa, respectively. The calculated isoelectric point (pI) is shown for each construct.

The work of this thesis focuses on nanobodies 13A7 (Fig. 5A, 5E) and 1c81 (Fig. 5B-D). Following the observation that 1c81 precipitates in solution at high concentrations, the sequence of 1c81 was optimized in order to improve solubility. Five amino acid replacements were introduced in the framework regions using amino acids found in non-aggregating nanobodies (K10G, A14P, S77T, L82M, K83R) (Ablynx), yielding a

stabilized construct of 1c81, designated 1c81^s (Fig. 5C). Moreover, since nanobodies with a basic isoelectric point (pI) reportedly displayed enhanced passage across the blood brain barrier (BBB) (Li et al., 2012; Li et al., 2016), two basic residues (Q3K and Q105K) were introduced in the framework region 1 and 4 and two copies of a basic peptide-tag, the SNB tag (Schaffer et al., 2010), were genetically fused to the C-terminus. The SNB tag is a 10-amino acid long peptide (PRPSNKRLQQ) derived from the synaptobrevin protein of *C. elegans*. The construct of 1c81 containing both, the stabilizing replacements and the pI high modifications was designated 1c81^{sh} (Fig. 5D). The pI of each nanobody construct was calculated from its amino acid sequence. The values ranged from 8.1 to 9.7 for the 1c81 constructs and from 5.7 to 5.9 for the 13A7 constructs (Fig. 5).

Because P2X7 is a homotrimeric ion channel, increasing avidity by nanobody dimerization can enhance binding and improve functional potencies (Stortelers et al., 2018). To this end, 13A7 and 1c81 variants were genetically fused via a flexible 35 amino acid long peptide linker (Fig. 5A-D). Since a long *in vivo* half-life is desired for potential therapeutic applications, the albumin-specific nanobody Alb8 (Tijink et al., 2008) was fused via a flexible 9 amino acid long linker to the P2X7-nanobody dimers in order to prevent renal clearance (Fig. 5A-D). These half-life extended nanobody dimers were designated Nb-dim-HLE, 13A7-dim-HLE and 1c81-dim-HLE carry a COOH-terminal hexahistidine tag (His6x) tag followed by a c-Myc tag (Fig. 5A-B); 1c81-dim^s HLE (Fig. 5C) is tagless, and 1c81-dim^{sh}-HLE carries two copies of the SNB tag in place of the His6x-cmyc tags.

As an alternative approach to reducing kidney clearance, the molecular size of 13A7 was increased by genetically fusing nanobody 13A7 to the hinge and Fc domains of mouse IgG2c, thereby reconstituting the bivalent heavy chain antibody format, designated 13A7-mIgG2c^{D265A}. Substitution of residue D265 by alanine is known to abolish binding to Fcγ receptors (FcγR), thereby avoiding Fc-mediated effector functions such as phagocytosis or complement activation (Baudino et al., 2008) (Fig. 5E). While a bivalent HLE-extended P2X7-specific nanobody dimers and a Nb-hinge-Fc fusion protein each are composed of three Ig domains having a size of 45 kDa (Fig. 5A-E), the covalent linkage of a pair of Nb-hinge-Fc fusion proteins via two disulfide bonds in the hinge region yield a P2X7-specific heavy chain antibody of ~90 kDa (Fig. 5E).

3.1.2 Expression, purification and chemical characterization of the engineered nanobodies

The engineered nanobodies shown in Fig. 5 were produced as secretory proteins in a mammalian expression system to ensure proper folding and glycosylation. HEK-6E cells were transiently transfected with nanobody expression constructs. After five-six days, the recombinant nanobodies were purified from the cell-supernatant by affinity chromatography on either immobilized metal affinity resin or protein A sepharose beads. Purification was monitored by SDS-PAGE analysis of aliquots of the cell supernatant, column flow through, the last column wash and four sequential elutions (Fig. 6A). Eluted proteins were desalted by buffer exchange via gel filtration in a histidine-sucrose buffer (HSB) or phosphate-buffered saline (PBS). Production yields typically were 1 - 10 mg per 100 ml of transfected HEK-6E cells. SDS-PAGE analysis of purified and rebuffed proteins confirmed the integrity and high purity of the engineered nanobodies (Fig. 6B). For intracerebroventricular injections nanobodies were highly concentrated (20 - 50 mg/ml) via centrifugation filters with a cut-off of 10 kDa.

To experimentally determine the pI of the engineered bivalent HLE nanobodies, a non-equilibrium pH gradient electrophoresis (NEPHGE) (O'Farrell et al., 1977) was performed. The results of the pH-gradient gel stained with Violet (SERVA®) show pI values consistent with the calculated pI values (Fig. 6C).

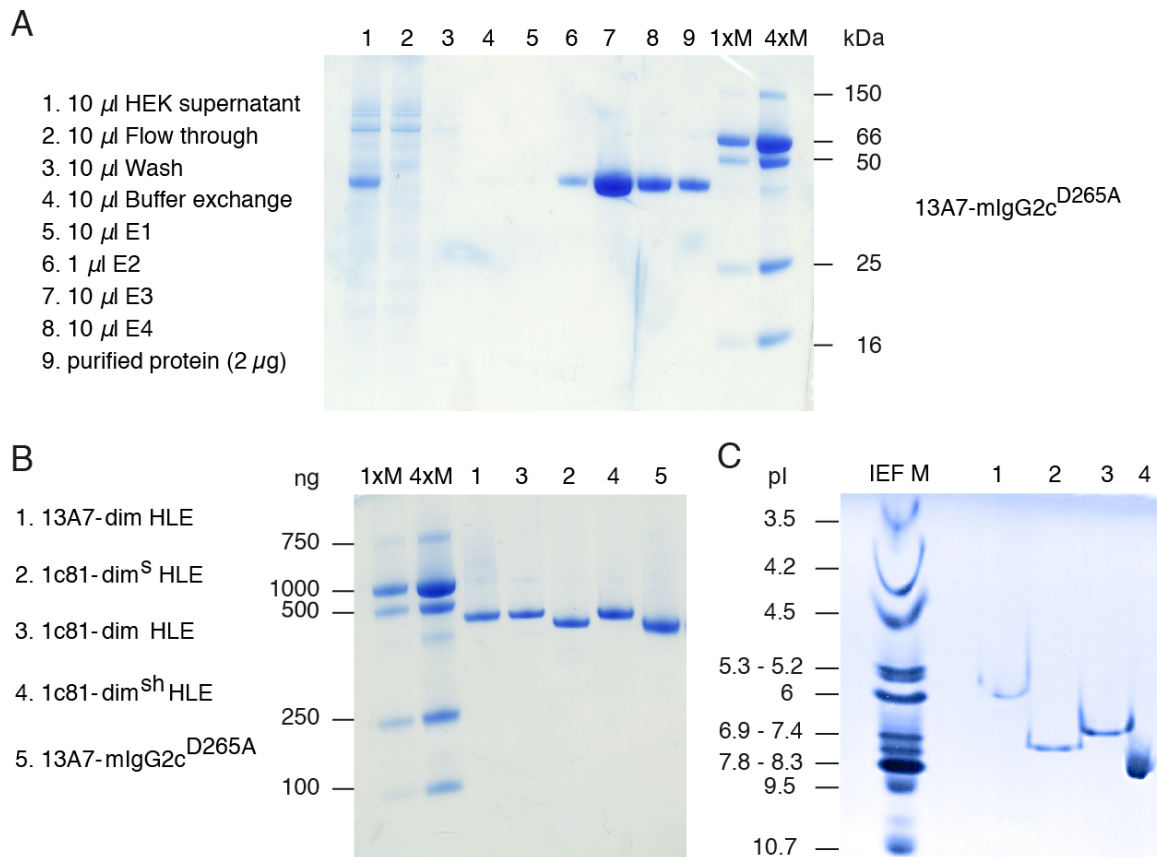


Figure 6. Expression, purification and chemical characterization of engineered nanobodies. (A) Example of a nanobody purification procedure. 13A7 fused to mouse IgG2c^{D265A} (13A7-mIgG2c^{D265A}) was expressed in transiently transfected HEK cells and purified from the cell-supernatant by protein A-based affinity chromatography. Re-buffering and concentration of the purified protein was performed using centrifugation filters with a Mw cut-off of 10 kDa. Proteins in the collected fractions were separated by SDS-PAGE and stained with Coomassie brilliant blue. Wells were loaded with 10 μ l aliquots of the following samples: lane 1: supernatant of transfected HEK cells (90 ml total volume), lane 2: unbound protein fraction (flow-through), lanes 3, 4: column washes (20 ml and 15 ml total volume), lanes 5-8: elutions 1-4 (2.5 ml each), lane 9: purified protein (2 μ g), lanes 10 and 11 were loaded with marker proteins at 1x and 4x amounts/lane respectively: 64 kDa: 1 and 4 μ g BSA, 50 kD: 0.5 and 2 μ g IgGH, 25 kDa: 0.25 and 1 μ g IgGL, 16 kDa: 0.1 and 0.4 μ g lys. (B) SDS-PAGE analysis of purified nanobodies used for *in vivo* injections. Coomassie-stained SDS-PAGE gel loaded with 2 μ g/lane of affinity purified nanobodies. Bivalent half-life extended nanobodies (lanes 1-4), bivalent heavy chain antibody (13A7-mIgG2c^{D265A}) (lane 5), 1-4x protein markers as in (A). His-tagged 13A7-dim HLE (lane 1) was purified using Ni-NTA-columns, all other nanobodies (lane 2-4) were purified using protein A-columns. (C) Determination of the isoelectric point (pI) of nanobodies by non-equilibrium pH gel electrophoresis (NEPHGE). A Serva® pH-gradient gel (pH3-pH10), loaded with 8 μ g/lane of bivalent HLE nanobodies was stained with Serva® Violet, SERVA® pI marker for isoelectric focusing electrophoresis. Lane 1: marker proteins of known pI.

3.2 *In vitro* targeting of P2X7 with engineered bivalent P2X7-antagonistic half-life extended nanobodies

In this chapter, I will present the results of *in vitro* functional characterization of the engineered P2X7-antagonistic nanobodies with respect to their binding specificity and their inhibitory potency of ATP-induced P2X7 downstream effects. The results confirm that P2X7-specific nanobodies bind P2X7 with high specificity and block ATP-induced Ca^{+2} influx, inflammasome assembly, and release of IL-1 β .

3.2.1 Monovalent and bivalent formats of nanobodies bind P2X7 with high specificity

In order to determine whether the engineered bivalent P2X7-antagonistic nanobodies bind specifically to mouse P2X7, HEK cells were co-transfected with expression constructs for either mouse (m) P2X1, P2X4 or P2X7 and green fluorescent protein (GFP). One day post transfection, cells were analyzed by flow cytometry. As controls, AF647-conjugated-antibodies specific for P2X1 (CR30), P2X4 (RG96A246) and P2X7 (Hano44). These antibodies showed exclusive binding to their respective P2X receptor (Fig. 7A). Cell-bound monomeric nanobodies were detected by staining with α -c-Myc tag antibody conjugated to AF647 (Fig. 7B). To detect dimeric HLE nanobodies cells were first incubated with an α -Alb8 mouse monoclonal antibody (mAb77) followed by an α -mouse IgG1 conjugated to BV421 (Fig. 7C). The results confirmed that all 13A7 and 1c81 nanobodies bound specifically to mP2X7 but not to mP2X1, mP2X4, or untransfected cells. Staining controls with unrelated nanobodies did not show any unspecific staining of untransfected cells or transfected cells.

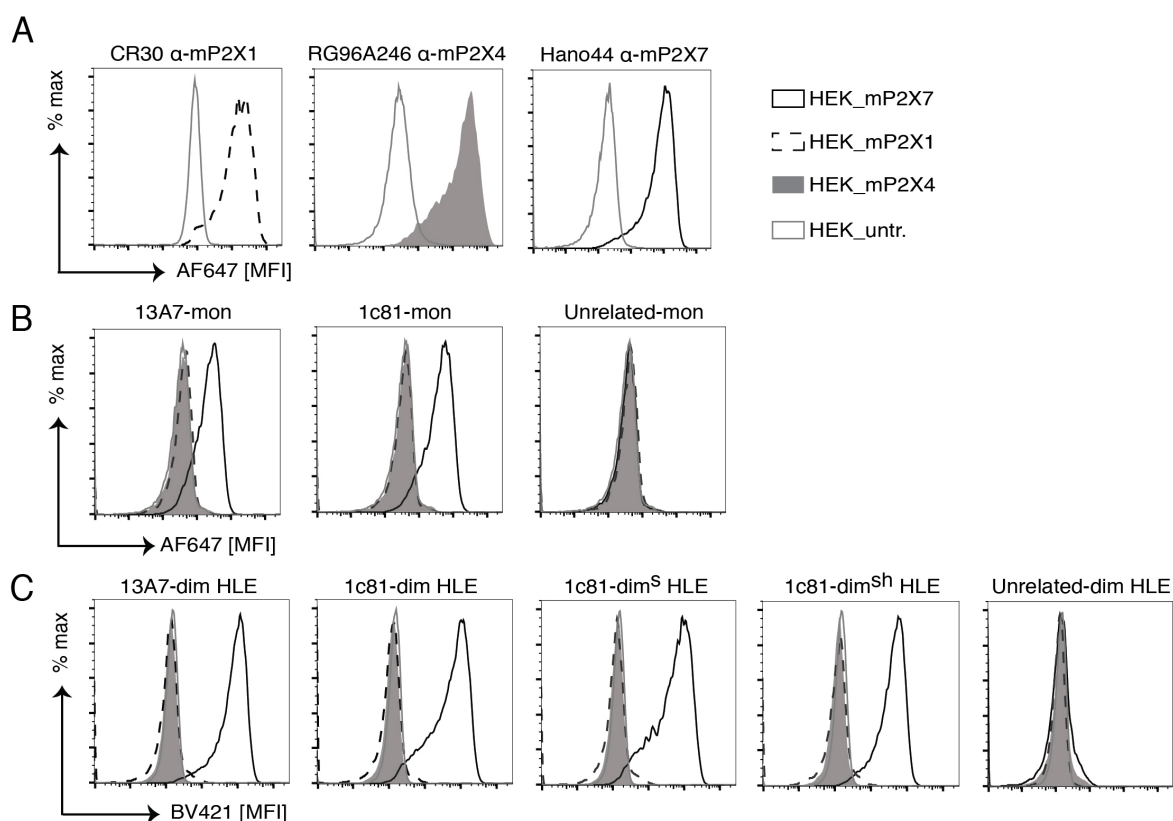


Figure 7. Monovalent and bivalent formats nanobodies bind with high specificity to P2X7. Flow cytometry analysis showing the reactivity of different formats of nanobodies to mouse P2X purinoreceptors. HEK cells were co-transfected with expression plasmids encoding green fluorescent protein (GFP) and either mouse P2X1, P2X4 or P2X7 and harvested 2 days post transfection. Untransfected HEK cells were used as control. **(A)** Expression controls were performed with the indicated AF647-conjugated antibodies directed against mouse P2X1 (CR30), mouse P2X4 (RG96A246) and mouse P2X7 (Hano44). Each histogram shows an overlay of untransfected and transfected HEK cells (the latter gated on GFP+ cells). **(B, C)** Cells were incubated with the indicated monovalent (B) or bivalent nanobodies (C). Cell-bound monovalent nanobodies were detected with c-Myc tag-specific antibody 9E10 conjugated to AF647. Bound bivalent HLE nanobodies were detected with Alb8-specific antibody mAb77 followed by an α -mouse IgG1 secondary antibody conjugated to BV421.

3.2.2 Bivalent P2X7-specific nanobodies block ATP-induced Ca^{2+} influx more potently than their monovalent counterparts

Binding of ATP to P2X7 induces gating of the channel, resulting in a sustained influx of Ca^{2+} and Na^+ , and an efflux of K^+ . To verify that P2X7-specific nanobodies block the ATP-induced Ca^{2+} influx, HEK cells stably expressing mouse P2X7 were loaded with the fluorescent Ca^{2+} indicator Fluo4 and treated with 1.5 mM ATP at 37 °C for 20 min in the presence of titrated amounts of P2X7-specific nanobodies in monovalent and bivalent formats (Fig. 8A). The fluorescence intensity of Fluo-4, reflecting the

intracellular Ca^{2+} concentration, was analyzed by fluorimetry. The results show, that both, monovalent and bivalent P2X7-specific nanobodies block ATP-induced Ca^{2+} influx in a dose-dependent manner. Bivalent 13A7 and 1c81 constructs blocked P2X7 with similar nanomolar potencies (IC_{50} : 0.9 - 3.1 nM) (Fig. 8 A-B), whereas the monovalent nanobodies showed 7-fold lower potencies (IC_{50} 14 - 14.2 nM) (Fig. 8A). It is worth noting that the mutations inserted into 1c81 to increase the stability and isoelectric points did not diminish the blocking potency of this nanobody (Fig. 8B).

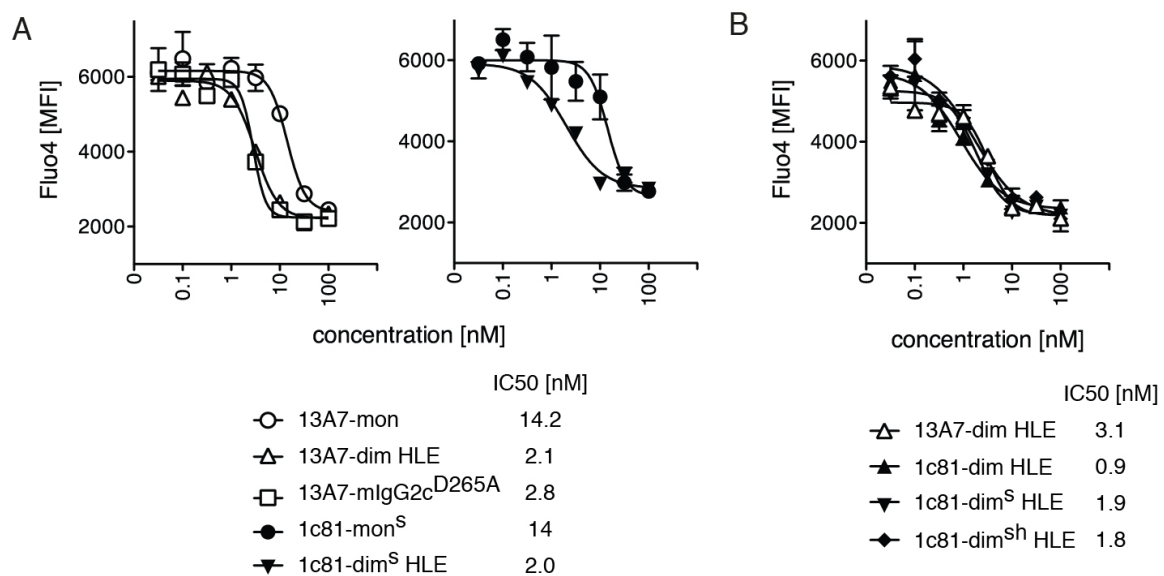


Figure 8. Bivalent P2X7-specific nanobodies block ATP-induced influx of Ca^{2+} more potently than their monovalent counterparts. HEK cells stably transfected with mouse P2X7 were loaded with Fluo4 and incubated in 96 well plates with 1: $\sqrt{10}$ serial dilutions of monovalent (A, B) and bivalent nanobodies (B) for 30 min before addition of ATP to a final concentration of 1.5 mM. Fluo4 fluorescent intensity was measured with a fluorimetric plate reader over 20 min at 37 °C. An increase in Fluo4 signals reflects the influx of Ca^{2+} . The graphs show average endpoint measurements (n = 3) +/- SD at 20 min. IC_{50} values were calculated with Prism software. A lower IC_{50} value corresponds to a higher blocking potency.

3.2.3 Dimeric half-life extended P2X7-specific nanobodies effectively block ATP-induced release of IL-1 β by endotoxin-primed primary microglia

Microglia are resident innate immune cells in the central nervous system (CNS) that express high levels of P2X7. Gating of P2X7 by ATP triggers an efflux of K^+ , which in turn triggers inflammasome activation and the processing and release of IL-1 β . In order to assess whether P2X7-specific dimeric HLE nanobodies block IL-1 β release in microglia, mixed glial cell cultures were primed with endotoxin (LPS, 1 $\mu\text{g}/\text{ml}$) for 4 h at 37 °C. Titrated amounts of dimeric HLE P2X7-specific nanobodies were applied, the

incubation continued for 30 more min before addition of ATP (1.5 mM) and further incubation for 30 min at 37°C. Cell supernatants were collected and the levels of secreted IL-1 β were determined by ELISA (Fig. 9). The results show that all tested nanobodies effectively block ATP-induced IL1- β release from LPS-primed microglial cells in a dose-dependent manner (IC50 values ranging from 0.6 to 3.3 nM).

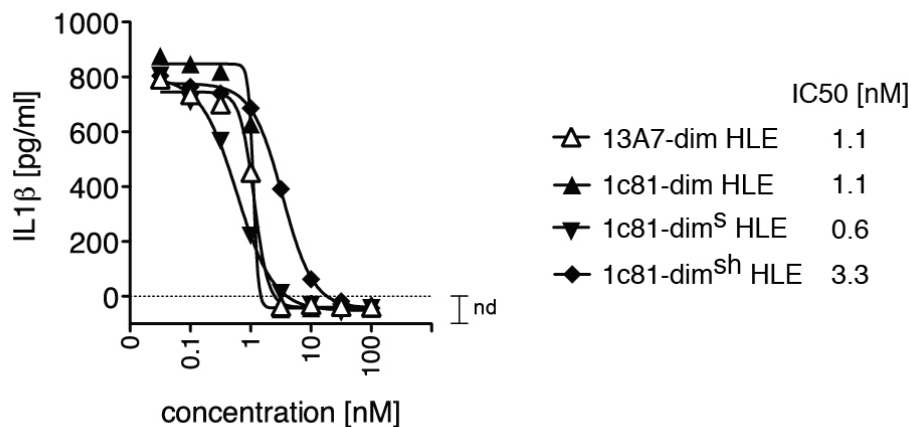


Figure 9. Bivalent half-life extended P2X7-specific nanobodies effectively block ATP-induced release of IL-1 β by endotoxin-primed mouse microglia. Neonatal mouse brain cells were cultured for 14 days and then re-plated onto 12 well plates at a density of 3×10^5 cells/ml and then cultured for 7 more days. At the time of analysis, the cells differentiated in vitro in a mixture composed of 20-30% microglia and 60-70% astrocytes. Cells were primed for 4 h with LPS (1 μ g/ml). Bivalent HLE nanobodies (1: $\sqrt{10}$ serial dilutions) were added and the incubation continued for 30 min before addition of ATP (to a final concentration of 1.5 mM). 30 min later, cell supernatants were harvested and analyzed for IL-1 β by ELISA. IC50 values were calculated with Prism software.

3.2.4 Dimeric half-life extended P2X7 nanobody 13A7 blocked ASC speck formation in endotoxin-primed peritoneal macrophages

Macrophages are innate immune cells that, after having been activated by pathogens or cellular debris, can release pro-inflammatory cytokines such as IL1 β . Macrophages, just as microglia, express P2X7 and P2X7 activation by ATP-binding leads to inflammasome assembly, processing and release of IL1- β . The inflammasome assembly involves oligomerization of the inflammasome adaptor protein ASC (apoptosis-associated speck-like protein containing a caspase recruitment domain CARD). In order to evaluate whether P2X7-specific nanobodies can block ATP-induced inflammasome assembly, ASC speck formation was monitored by fluorescence microscopy in LPS-primed peritoneal macrophages.

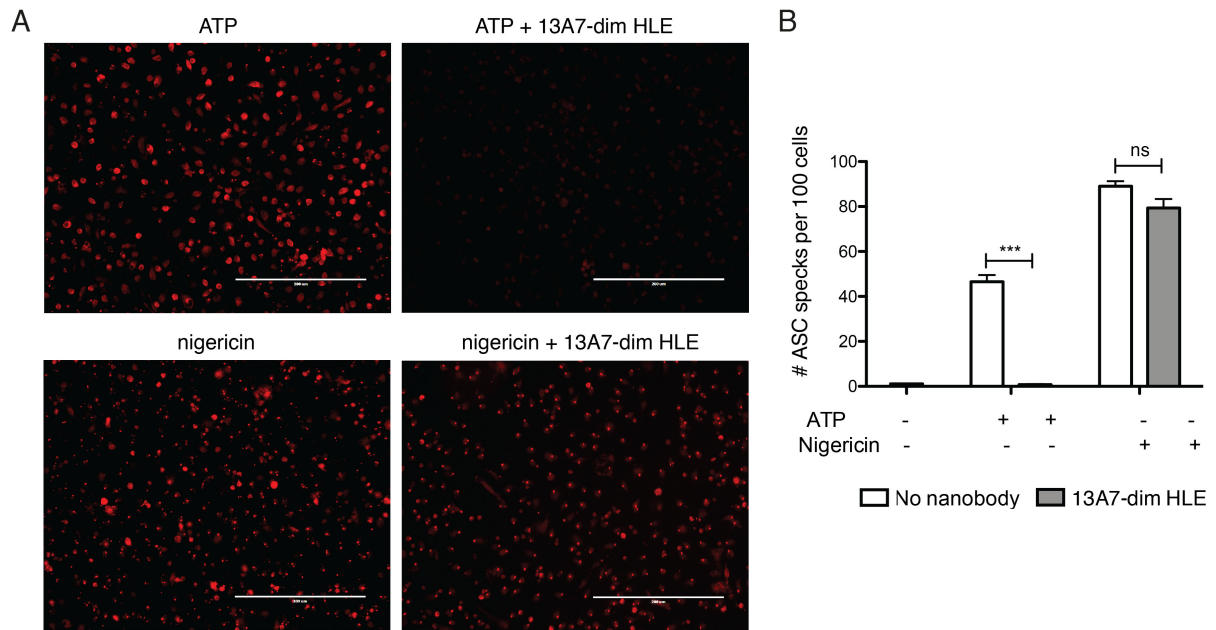


Figure 10. Bivalent half-life extended P2X7-specific nanobody 13A7 blocks ATP-induced activation of the inflammasome by endotoxin-primed mouse peritoneal macrophages. (A) The activation of the inflammasome in peritoneal macrophages was monitored by fluorescence microscopy. Mouse peritoneal macrophages were seeded onto coverslips overnight. Cells were treated for 4 h with LPS in the absence or presence of 13A7-dim HLE nanobodies, before addition of ATP or nigericin and further incubation for 30 min at 37°C. Cells were fixed with paraformaldehyde and ASC-specks were visualized using an α -mouse ASC rabbit antibody followed by a secondary PE-conjugated α -rabbit IgG antibody. (B) The number of ASC specks per field of vision was quantified. Data are averages \pm SD (n = 6 fields of vision).

Mouse peritoneal macrophage were seeded onto poly-L lysine coated coverslips overnight and following 4 h of LPS priming (1 μ g/ml) at 37 °C, they were incubated with 13A7-dim HLE for 30 min and treated with ATP for at 37 °C for 30 min. Cells were fixed, permeabilized and ASC specks were detected with an ASC-specific rabbit antibody followed by a PE conjugated rabbit-IgG-specific antibody. Nuclei were stained with DAPI. Images were obtained with a fluorescence microscope and specks were quantified by counting six fields of vision each containing at least 100 cells (Fig. 10A-B). In addition, as P2X7-independent control, ASC speck formation was analyzed after treatment with nigericin (10 μ M), a K⁺ ionophore and potent activator of the inflammasome (Fig. 10A-B). The results show that 13A7-dim HLE effectively blocked ATP-induced but not nigericin-induced ASC speck formation, indicating that 13A7-dim HLE specifically blocked the P2X7-dependent pathway of inflammasome assembly (Fig. 10B).

The results of this chapter show that the capacity of bivalent P2X7-antagonistic nanobodies to block ATP-induced effects in P2X7-transfected HEK cells and primary cells was preserved after various modifications introduced by nanobody engineering to increase the stability, isoelectric point, half-life and molecular size of the constructs.

3.3 *In vivo* targeting of the P2X7 ion channel with engineered bivalent P2X7-antagonistic half-life extended nanobodies

The following chapter describes the *in vivo* pharmacological characterization of bivalent HLE P2X7-antagonistic nanobodies. Tissue penetration of intravenously injected nanobodies requires passage across the vascular endothelium. It has been reported that intravenously injected conventional antibodies (150 kDa) penetrate peripheral tissue but do not achieve effective penetration into the brain (0.1 – 0.7% of the injected dose was found in the brain) (Abuqayyas and Balthasar, 2013; Bousquet and Janin, 2014; Rubenstein et al., 2003). To test the hypothesis that engineered P2X7-specific nanobodies can effectively reach P2X7 on immune cells in various tissues, experiments were designed to evaluate the ability of nanobodies to penetrate brain parenchyma and peripheral tissues, in this instance renal tissue, following intravenous (iv) or intracerebroventricular (icv) administration. To this end, the degree of P2X7 occupancy on microglia and renal T helper (Th) cells was monitored by flow cytometry after injection of these nanobodies in various doses. In parallel, the capacity of the injected nanobodies to block ATP-induced pore formation was evaluated by monitoring the ATP-induced uptake of the cell-impermeant dye, 4,6-Diamidin-2-phenylindol (DAPI). As an alternative to nanobody injections, the capacity of endogenously synthesized nanobodies to reach P2X7 on immune cells in the brain and kidney was analyzed 6 months after transduction of mouse muscle cells by means of a single intramuscular injection of AAV-encoding nanobodies.

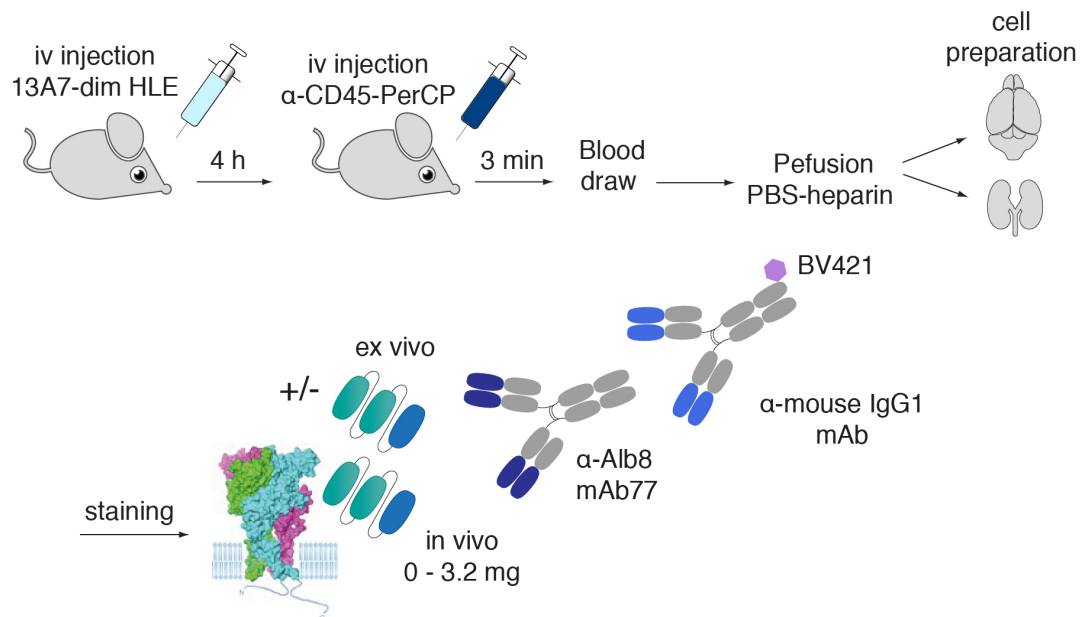


Figure 11. Experimental strategy to assess occupancy of cell surface P2X7 achieved by systemically injected bivalent HLE-nanobodies. The schema illustrates the experimental set up used to monitor occupancy of P2X7 by injected nanobodies. Bivalent HLE nanobody dimers were injected intravenously into C57BL/6 mice. Circulation was allowed for 4 h. To stain intravascular leukocytes, a PerCP-conjugated CD45-specific antibody was injected intravenously 3 min before sacrifice. At the time of sacrifice a sample of blood was obtained to measure levels of soluble unbound nanobodies in serum and mice were perfused with PBS-heparin to remove erythrocytes and unbound circulating nanobodies. Brain and kidneys were gently homogenized in the presence of collagenase and leukocytes were enriched using Percoll density gradient centrifugation. Aliquots of the cell suspension were incubated either with a saturating dose of the injected HLE nanobody dimer to assess the maximal level of occupancy of cell surface P2X7 (+ *ex vivo*) or without exogenously added nanobodies to assess the *in vivo* occupancy of P2X7 attained by the injected nanobody (*in vivo*). Cell surface-bound Nb-dim HLE were detected with Alb8-specific mAb77 followed by BV421-conjugated alpha-mouse IgG1 antibody. Cells were counterstained with fluorochrome-conjugated antibodies specific for microglia (CD11b and CD45) or renal T cells (CD45, CD4, CD8 and CD69).

The experimental strategy to assess the degree of P2X7 occupancy by the injected HLE-nanobody dimers is illustrated schematically in Fig. 11. Circulation of the engineered nanobodies was allowed for 4 h. In order to distinguish vascular from parenchymal resident immune cells, mice were injected with a alpha-CD45 PerCP conjugated antibody 3 min before sacrifice to solely stain CD45+ cells in the vasculature (Anderson et al., 2014). An aliquot of blood was collected to determine the level of unbound nanobodies in circulation and mice were then perfused with PBS-heparin to remove unbound soluble nanobodies in serum and erythrocytes. Dissected brains and kidneys were digested with collagenase, a cell suspension was prepared using tissue strainers, and leukocytes were enriched by means of a Percoll density gradient centrifugation. Cell bound HLE nanobodies were then detected by flow

cytometry using a monoclonal antibody directed against the HLE unit, i.e. the albumin-specific nanobody Alb8. Hence, cells were incubated sequentially with the α -Alb8 mouse IgG1 monoclonal antibody (mAb77, provided by Ablynx) followed by an α -mouse IgG1 conjugated to BV421 (Fig. 11). Cells were counterstained with fluorochrome-conjugated antibodies specific for microglia (CD11b and CD45) or renal T cells (CD45, CD4, CD8 and CD69). In order to assess the maximal possible occupancy of P2X7 by the HLE nanobodies, an aliquot of cells was incubated *ex vivo* with a saturating dose of the same nanobody construct that had been injected *in vivo* followed by the same staining protocol.

3.3.1 Full occupancy of P2X7 on microglia can be achieved by a high dose of intravenously injected 13A7-dim HLE

In vivo brain penetration and efficacy of intravenously injected 13A7-dim HLE at different doses were evaluated 4 hours after injection into wildtype C57BL/6 mice by determining the degree of P2X7 occupancy on microglia and the effect on P2X7 function achieved by the injected dose of nanobody using the flow cytometry set up described in Fig. 11. In a first experiment, we intravenously administered 32 μ g to 3.2 mg of 13A7-dim HLE in a $\sqrt{10}$ serial dilution series into C57BL/6 mice. Intravascular leukocytes were stained by injection of a CD45-specific mAb, 3 min before sacrifice. A sample of blood was taken at the time of sacrifice to measure unbound circulating 13A7-dim HLE. To assess the degree of P2X7 occupancy, we measured *in vivo* binding of 13A7-dim HLE on microglia using the α -Alb8 mAb77 (Fig. 12).

Cells were counterstained *ex vivo* with a second α -CD45 APC-Cy7 conjugated antibody to distinguish CD45+ cells from the brain tissue along with an α -CD11b antibody to mark microglia (Fig. 12A). We gated on this population and analyzed P2X7 staining. As a control that displays full degree of occupancy, an aliquot of cells was spiked (+ *ex vivo*) with a saturating amount of 13A7-dim HLE. As negative control, mice that had received an injection of saline solution (0 mg Nb) were used (Fig. 12B).

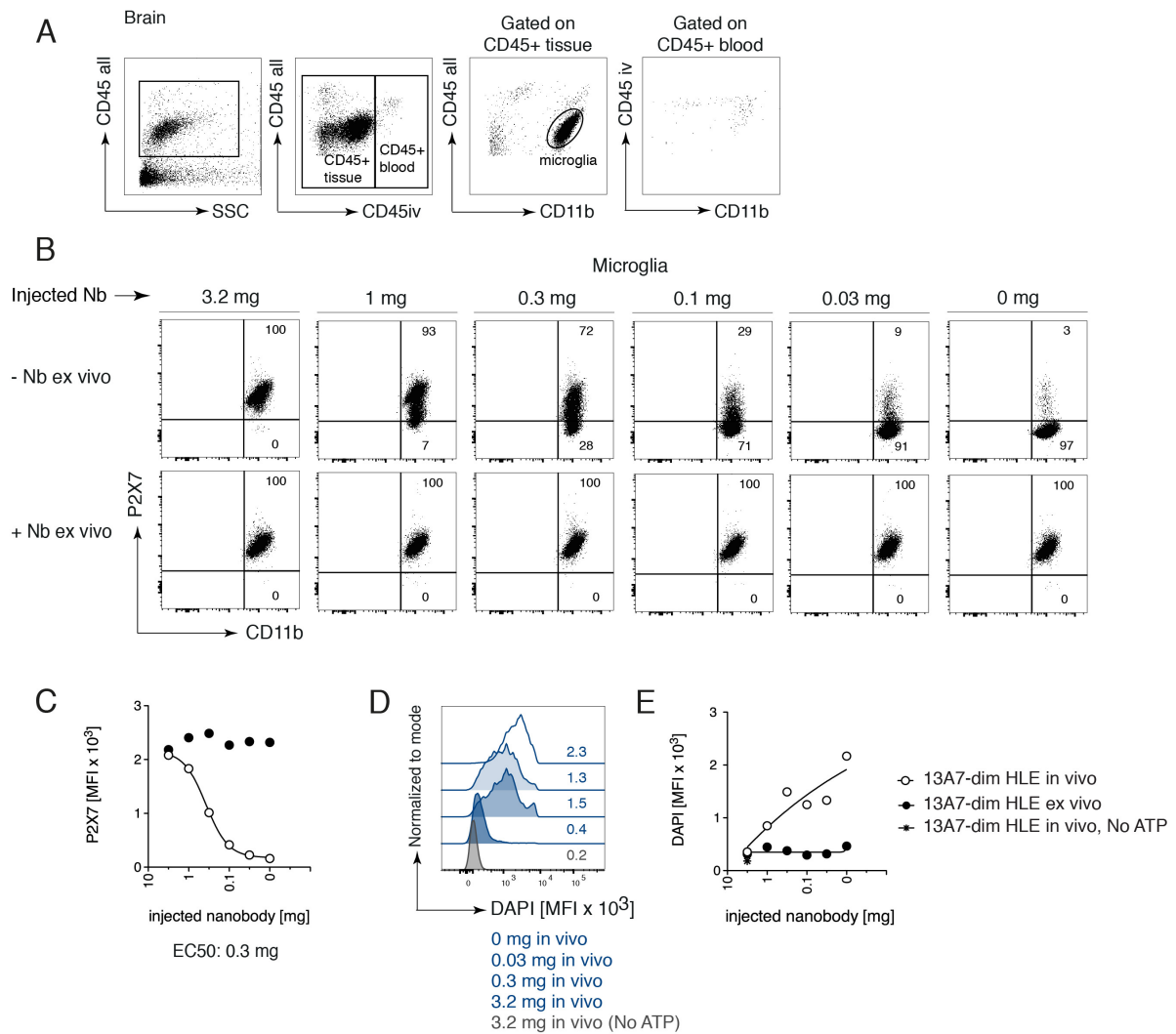


Figure 12. Full occupancy of P2X7 on microglia is achieved only by a high dose (3.2 mg) of intravenously injected 13A7-dim HLE. Titrated amounts of 13A7-dim HLE were injected intravenously into C57BL/6 mice. Mice were sacrificed 4 h later and brain microglia were analyzed for occupancy of cell surface P2X7 as illustrated schematically in Fig. 11. **(A)** Microglia were identified by sequential gating of CD45^{int} and CD11b^{high} cells and by excluding intravascular cells (stained by the iv injected α -CD45). **(B)** Flow cytometry dot plots of gated microglia illustrating the relative occupancy of cell surface P2X7 achieved by the injected nanobody (top, -Nb *ex vivo*) vs. the maximal occupancy achieved after *ex vivo* addition of saturating nanobody (bottom, +Nb *ex vivo*). **(C)** Graph displaying the mean fluorescence intensity (MFI) of P2X7 staining on CD11b+ microglia vs. the dose of injected nanobody. Open circles = staining obtained by the injected nanobody *in vivo*, closed circles = maximal staining achieved after addition of nanobody *ex vivo*. **(D)** To assess whether the injected nanobodies were able to block ATP-induced activation of P2X7, microglia were treated for 10 min with 0.5 mM ATP at 37°C in the presence of the DNA staining dye DAPI. The DAPI mean fluorescence intensity of CD11b+ microglia were measured by flow cytometry and is shown here as overlaid histograms. **(E)** Graph displaying ATP-induced DAPI uptake (MFI) by CD11b+ microglia vs. the dose of injected nanobody. Open circles = samples analyzed after nanobody injection *in vivo*, closed circles = maximal staining achieved after addition of nanobody *ex vivo*.

The results show that at 4 h after injection, 13A7-dim HLE occupied P2X7 on microglia in a dose dependent manner (Fig. 12B-C). The calculated effective dose required to occupy half of the total available P2X7 on microglia (EC50) is 0.3 mg. Full occupancy was achieved with the highest dose of 3.2 mg (150 mg/Kg), whereas low doses of 32 μ g (1.5 mg/Kg) resulted in only barely detectable levels of HLE-nanobodies bound to P2X7 on microglia (Fig. 12B-C)

To assess the effect on P2X7 function achieved by the nanobody bound *in vivo* we measured ATP-induced DAPI uptake in microglia by flow cytometry. Cells were loaded with DAPI and incubated with 0.5 mM ATP at 37 °C for 10 min and washed before flow cytometry (Fig. 12D-E). The results show a dose dependent inhibition of ATP-induced DAPI uptake by microglia. However only the highest dose 3.2 mg (150 mg/Kg) was sufficient to completely block P2X7-mediated DAPI uptake 4 h after intravenous injection (Fig. 12D-E). The intermediate dose of 100 μ g (5 mg/Kg) achieved partial occupancy (Fig. 12B-C) and blockade of P2X7 (Fig. 12E).

3.3.2 Complete occupancy of P2X7 on renal T helper Th cells is achieved by a 300-fold lower dose of intravenously injected 13A7-dim HLE

In a second experiment, we intravenously administered a lower dose range of 13A7-dim HLE (1 – 200 μ g) into C57BL/6 mice in order to evaluate penetration into the kidney parenchyma. To measure the degree of P2X7 occupancy achieved by the injected nanobody we focused on renal CD4+ T helper (Th) cells that reside deep in kidney tissue, recently described as tissue resident memory T cells (Trm). These cells express CD69, a marker of tissue residency, and high levels of P2X7, allowing a convenient, robust analysis of nanobody penetration through the peripheral endothelium into the kidney parenchyma.

The levels of 13A7-dim HLE bound *in vivo* to P2X7 on Th cells were measured by flow cytometry using the detection system illustrated in Fig. 11. Again, a staining control of maximal P2X7 occupancy was set up using *ex vivo* addition of an excess of 13A7-dim HLE and a negative occupancy control was set up using a PBS-injected mouse (Fig. 13).

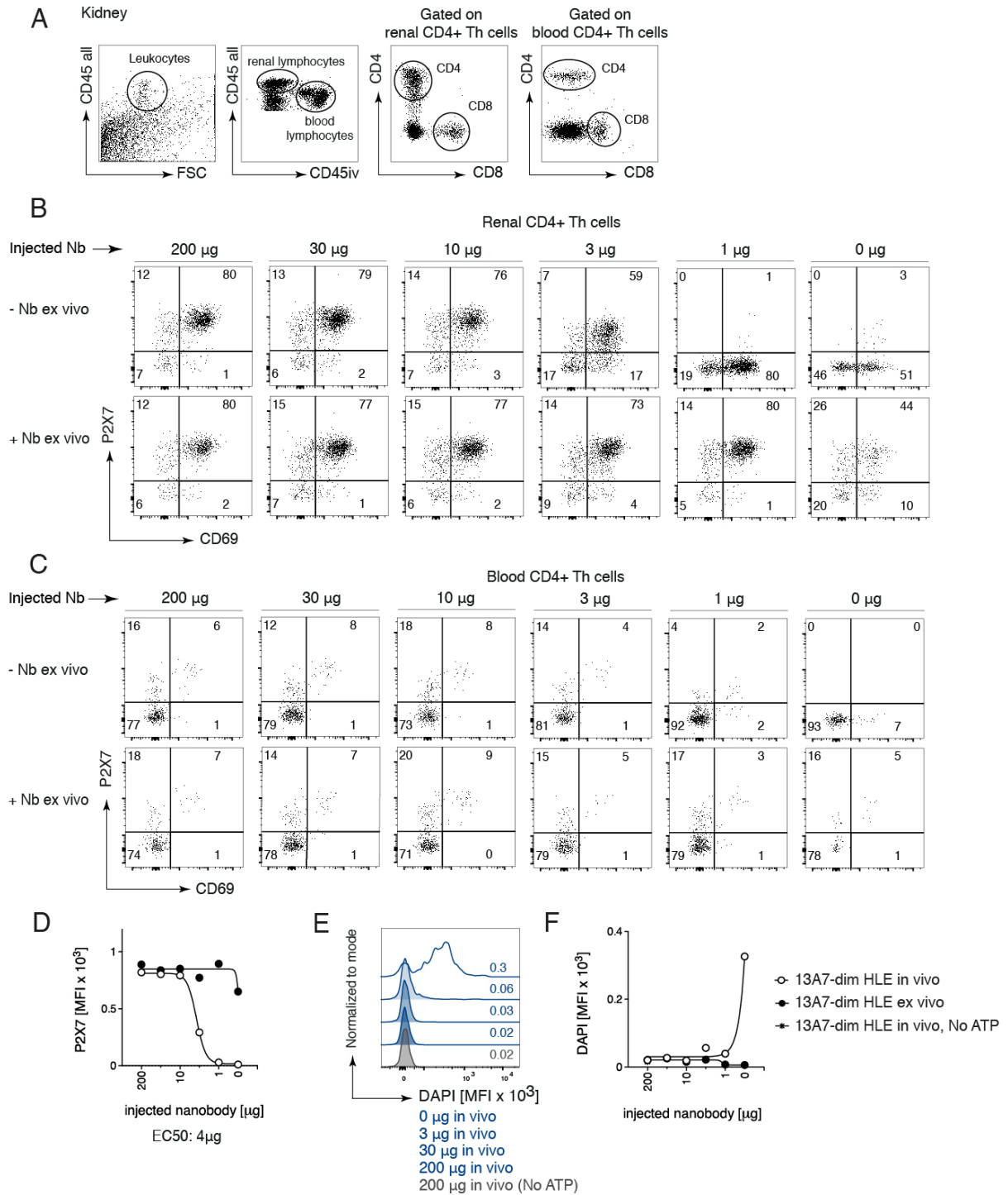


Figure 13. Full occupancy of P2X7 on renal CD4+ T cells is achieved already by low doses ($> 10 \mu\text{g}$) of intravenously injected 13A7-dim HLE. Titrated amounts of 13A7-dim HLE were injected intravenously into C57BL/6 mice. Mice were sacrificed 4 h later and renal T cells were analyzed for occupancy of cell surface P2X7 as illustrated schematically in Fig. 11. **(A)** Parenchymal and vascular leukocytes were identified respectively by gating of cells stained or not by the iv injected α -CD45. Helper T cells were identified by positive staining with α -CD4. Cells were counterstained with fluorochrome labeled antibodies against CD8 (as a marker of cytotoxic T cells) and CD69 (as a marker of tissue residency). **(B, C)** Flow cytometry dot plots of parenchymal **(B)** and intravascular **(C)** Th cells illustrating relative occupancy of P2X7 obtained by the injected nanobody (top, -Nb ex vivo) vs. the maximal occupancy of P2X7 achieved after ex vivo addition of an excess of nanobody (bottom, +Nb ex vivo). **(D)** Graph

illustrating the degree of P2X7 staining on parenchymal CD4 T cells vs. the dose of injected nanobody. Open circles = staining obtained by the injected nanobody *in vivo*, closed circles = maximal staining achieved after addition of nanobody *ex vivo*. (E) Overlaid histograms of total Th cells showing the level of DAPI uptake (MFI) obtained 4 h following injection of the indicated dose of 13A7-dim HLE after treatment with 125 μ M ATP. Corresponding graph depicting DAPI (MFI) values plotted against injected nanobody dose. (F) Graph illustrating ATP-induced DAPI uptake (MFI) in parenchymal CD4+ T cells vs. the dose of injected nanobody. Open circles = samples analyzed after nanobody injection *in vivo*, closed circles = maximal staining achieved after addition of nanobody *ex vivo*.

Blood leukocytes were stained with a PerCP-conjugated α -CD45 injected 3 min before sacrifice. Kidneys were homogenized in digestion solution by means of the tissue dissociator gentleMACS[®]. Then a cell suspension was prepared using appropriate tissue strainers and leukocytes were enriched by Percoll density gradient centrifugation. Renal leukocytes were discriminated by staining with a second AF700-conjugated α -CD45 antibody. Addition of a cocktail of α -CD4, α -CD8 and α -CD69 antibodies allowed distinction of T helper (Th) CD4+ cells, from T cytotoxic (Tc) CD8+ cells (Fig. 13A). We gated on CD4+ T lymphocytes and analyzed P2X7 staining in the CD69+ population within the renal compartment and compared to that of the CD69+ population within the blood compartment, which correspond to lymphocytes that remained within the vasculature and were not removed after perfusion (Fig. 13B-D). The results show that even low doses (10 μ g, 0.5 mg/Kg) of intravenously injected 13A7-dim HLE (Fig. 13B-D) were sufficient to completely occupy P2X7 on Th cells in the renal tissue (CD69+) as well as in Th cells from the vasculature (CD69-). Injection of 3 μ g (0.2 mg/Kg) resulted in full P2X7 occupancy on intravascular Th cells not expressing CD69, however this injected dose only achieved partial P2X7 occupancy on parenchymal Th cells expressing CD69 (Fig. 13B-D). The calculated half-maximal effective dose for occupancy of P2X7 on parenchymal kidney T cells (EC50) is 4 μ g (Fig. 13B-D).

To assess the functional effect of the bound nanobody (13A7-dim HLE) on ATP-induced pore formation by renal Th cells, DAPI uptake by CD4+ gated cells was measured by flow cytometry following ATP treatment (0.125 mM) at 37 °C for 10 min (Fig. 13E-F). The results show that injected doses of 13A7-dim HLE of 10 μ g or more achieved complete blockade of the ATP-induced DAPI uptake 4 h after intravenous administration (Fig. 13E-F).

3.3.3 Unbound soluble 13A7-dim HLE are detected in the serum in a dose-dependent manner 4 h after intravenous administration

To quantify the levels of soluble, unbound 13A7-dim HLE remaining in the serum at the time of analysis (4 h after injection), blood was drawn at the time of sacrifice by heart puncture. Serum was analyzed for soluble 13A7-dim HLE using a sandwich ELISA as illustrated in Fig. 14.

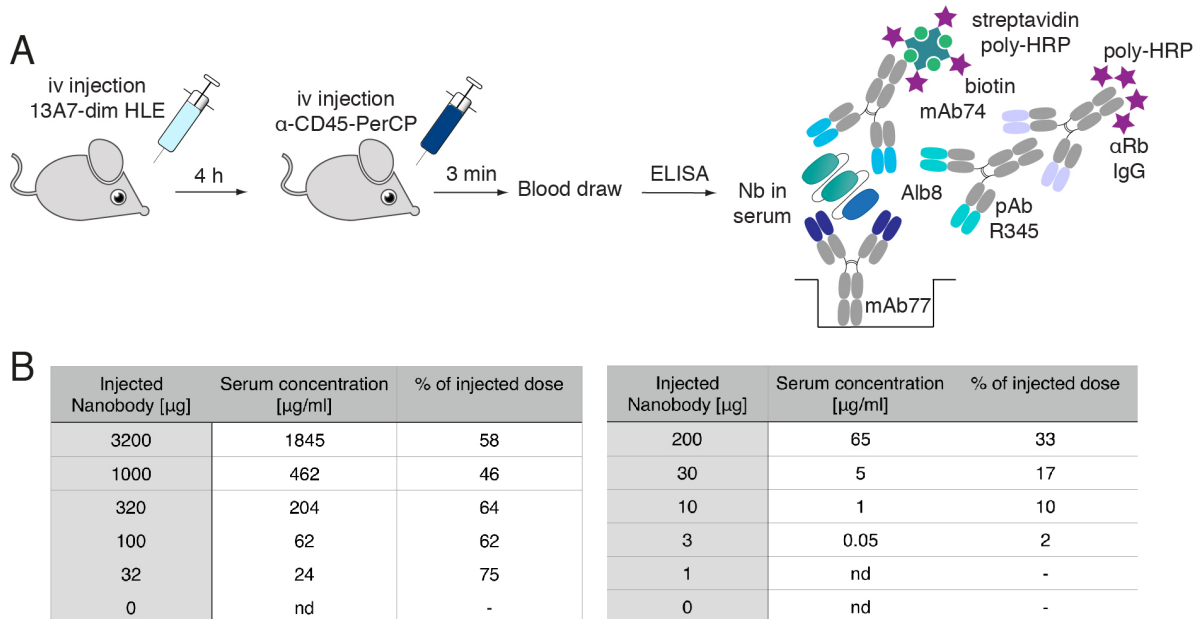


Figure 14. The concentration of unbound 13A7-dim HLE in serum 4 h after intravenous injection correlates with the administered dose. (A) Schematic diagram of the experimental set up: Four hours after intravenous injection of titrated concentrations of 13A7-dim HLE (0 - 3.2 mg), mice were anesthetized, and a blood sample was drawn by heart puncture. Serum was collected after blood clotting and the serum concentration of unbound nanobody was determined by sandwich ELISA. The Alb8-specific antibody mAb77 was used as catcher. As detector, we used either a biotinylated pan-nanobody-specific antibody mAb74 followed by poly-HRP conjugated streptavidin (for injected doses between 3.2 mg and 32 μg) or a pan-nanobody-specific rabbit antibody (pAbR345) followed by a poly-HRP conjugated rabbit IgG-specific secondary antibody. **(B)** Tables illustrating the calculated serum concentration (in $\mu\text{g}/\text{ml}$) of unbound nanobody 13A7-dim HLE vs. the dose of the injected nanobody. nd = not detectable (same as background).

The Alb8-specific mAb77 was immobilized on ELISA plates to capture HLE- nanobody dimers present in diluted sera from injected mice. Captured HLE nanobodies were detected with either biotinylated mAb74, a nanobody-specific mouse monoclonal antibody, or pAbR345, a nanobody-specific rabbit polyclonal antibody. A high sensitivity was achieved by using polymers of horseradish peroxidase (poly HRP) conjugated to respectively, either streptavidin or rabbit specific antibody (both provided

by Ablynx) (Fig. 14A). The results show that the concentrations of 13A7-dim HLE circulating in serum 4 h after injection correlate with the injected dose. Sera of mice injected with doses of 13A7-dim HLE between 32 μg and 3.2 mg/ml contained 20 $\mu\text{g}/\text{ml}$ to 1.8 mg/ml of this nanobody 4 h after injection (Fig. 14B). Considering that a 20 g mouse has a total serum volume of ~ 1 ml, these results demonstrate that the concentration of nanobody in serum was more than half of the injected dose 4 h after injection. Sera of mice injected with doses of 13A7-dim HLE between 3 and 200 μg contained 0.05-65 $\mu\text{g}/\text{ml}$ of this nanobody 4 h after injection, i.e. concentrations of less than half of the injected dose (Fig. 14B).

3.3.4 Full occupancy of P2X7 on microglia can be achieved by a high dose of intravenously injected 1c81-dim^{sh} HLE

It has been reported that nanobodies with a more basic isoelectric point display enhanced passage across the blood brain barrier (BBB) (Li et al., 2012; Li et al., 2016). We therefore analyzed the capacity of bivalent HLE 1c81 variants with different isoelectric points (pIs) (8.5 - 9.7) to penetrate into the brain and occupy P2X7 on microglial cells. Moreover, to investigate whether the molecular size has an influence on brain penetration, we performed parallel *in vivo* dose response experiments with a heavy chain antibody format of the P2X7-antagonistic nanobody 13A7 (90 kDa vs. 45 kDa of HLE-nanobody dimers). Thus, we injected titrated doses (32 μg - 3.2 mg) of 1c81^{sh}-dim HLE, 1c81^s-dim HLE and 13A7mIgG2c^{D265A} and analyzed the degree of P2X7 occupancy on microglia 4 h after intravenous injection. Cell bound dimeric HLE variants of 1c81 were detected as described above using α -Alb8 mAb 77. Cell bound heavy chain antibody 13A7-mIgG2c^{D265A} was detected by means of a sequential staining with biotinylated α -mouse IgG2c and BV421-labelled streptavidin (Fig. 15A). Again, we assessed the blocking effect of the *in vivo* bound nanobody by measuring the uptake of the ATP-induced DAPI.

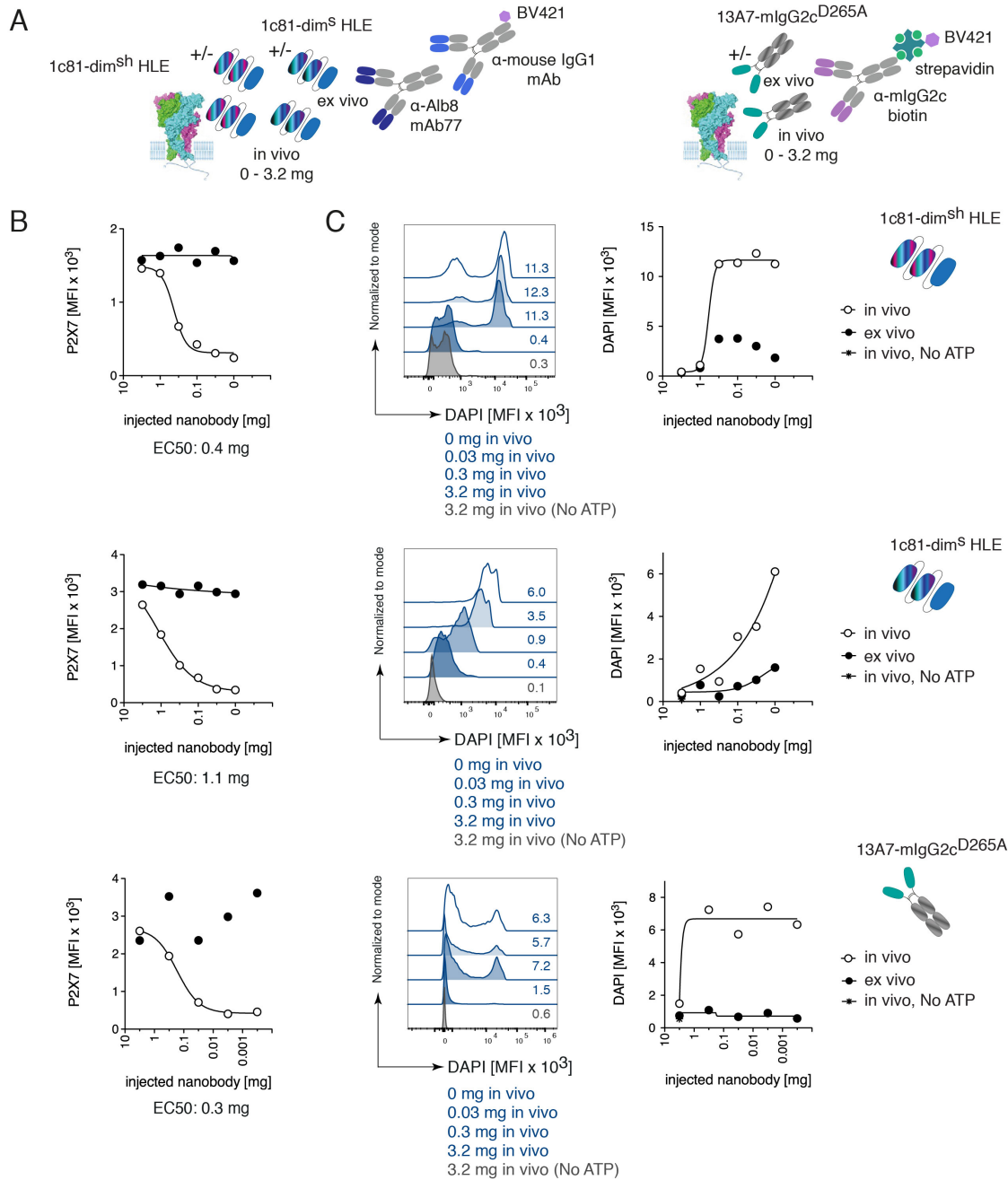


Figure 15. Full occupancy of P2X7 on microglia is achieved only by a high dose (> 1 mg) of intravenously injected 1c81-dim HLE and 13A7-mlgG2c. Three independent experiments were performed following the experimental setup illustrated in Fig. 11 to assess the occupancy of cell surface P2X7 on brain microglia achieved by intravenously injected bivalent nanobodies 1c81-dim^{sh} HLE, 1c81-dim^s HLE and 13A7-mlgG2c^{D265A}. **(A)** Schematic diagram illustrating the strategy used to detect cell bound nanobodies. Bivalent HLE nanobody dimers were detected as before using Alb8-specific mAb77 and BV421-conjugated α -mouse IgG1. Bound 13A7-mlgG2c^{D265A} was detected using biotinylated α -mouse IgG2c and BV421-conjugated streptavidin. **(B)** Graphs illustrating the degree of P2X7 staining on CD11b+ microglia vs. the dose of the indicated injected nanobody. Open circles = staining obtained by the injected nanobody (*in vivo*), closed circles = maximal staining achieved after addition of nanobody (*ex vivo*). **(C)** Overlaid histograms and graphs illustrating the blockade of ATP-induced DAPI uptake by microglia achieved by the injected nanobodies. Open circles = samples analyzed after nanobody injection (*in vivo*), closed circles = maximal staining achieved after addition of nanobody (*ex vivo*).

The results show that injection of the highest dose of 3.2 mg (150 mg/Kg) resulted in near maximal occupancy for all three tested constructs (Fig. 15B). The high pI HLE-nanobody dimer appeared slightly more effective than the lower pI counterpart (calculated EC50 or 0.4 mg vs. 1.1. mg) (Fig. 15B). Remarkably, the heavy chain antibody 13A7-mIgG2c^{D265A} also achieved high occupancy (calculated EC50 or 0.3 mg) (Fig. 15B). Taken together, these findings indicate that intravenous injection of a high dose (3.2 mg) of these nanobodies results in brain penetration, reflected by full occupancy of P2X7 on microglia, irrespective of the format. Consistently, at the highest injected dose of 3.2 mg (150 mg/Kg) all three constructs effectively blocked ATP-induced DAPI uptake 4 h after intravenous administration (Fig. 15C). Of note, the high pI variant 1c81-dim^{sh} effectively blocked ATP-induced DAPI uptake even at a lower injected dose of 1 mg (50 mg/Kg) (Fig.15C).

3.3.5 AAV-based *in vivo* production of 13A7-dim HLE results in an extensive and durable occupancy of P2X7 in microglia

Gene transfer technology using adeno-associated viral vectors (AAV) allows long-term expression of antibodies and other proteins *in vivo* (Brady et al., 2017). Because high doses of intravenously injected nanobodies were required to penetrate into the brain and fully occupy P2X7 on microglia, the AAV-based endogenous production of P2X7-blocking nanobodies may be an alternative to intravenous injections of nanobodies. In order to test this hypothesis, AAV-encoding 13A7-dim HLE were intramuscularly injected into wild type C57BL/6 mice. 190 days after intramuscular transduction, the level of P2X7 occupancy achieved by the endogenously produced nanobody on brain microglia and renal T helper Th cells was analyzed by flow cytometry using the detection system described in Fig. 11. Moreover, concentrations of soluble unbound nanobody dimers in serum were measured by ELISA. The experimental procedure is illustrated schematically in Fig. 16A, the gating strategy used for flow cytometry analyses of brain cells is shown in Fig. 16B (a small population of CD45^{high} CD11b^{high} cells; possibly representing infiltrating monocytes or macrophages, were excluded from the analysis).

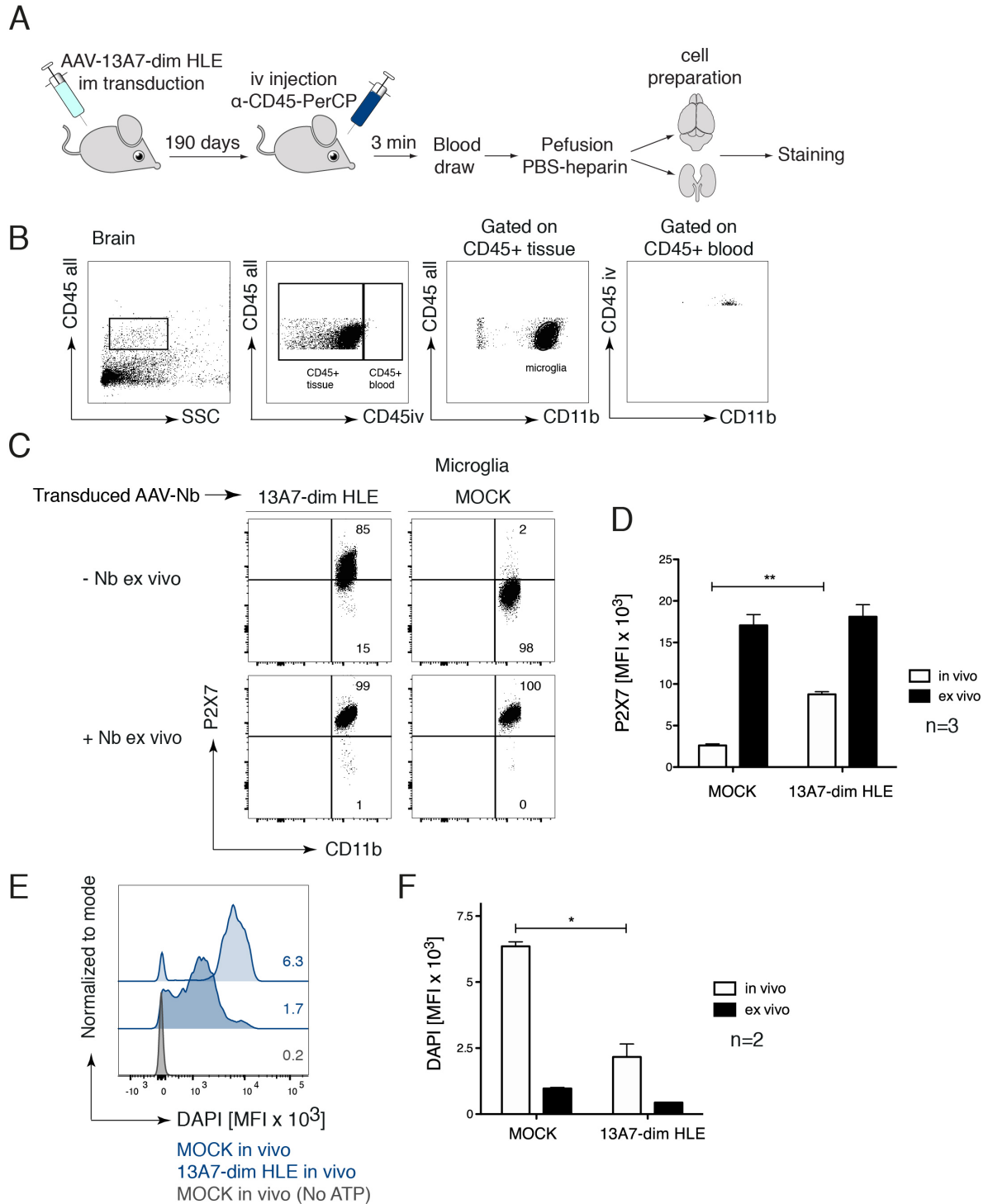


Figure 16. 190 days after intramuscular injection of 13A7-dim-HLE encoding AAV vectors, endogenously produced nanobodies are bound to P2X7 on microglia. (A) Schematic diagram of the experimental set up: AAV encoding 13A7-dim HLE (1×10^{11} viral genomes) were injected into the gastrocnemius muscle of C57BL/6 mice. 190 days later, occupancy of P2X7 on brain microglia was assessed following the strategy shown in Fig. 11. **(B)** Microglia were identified by sequential gating of $CD45^{int}$ and $CD11b^{high}$ cells and by excluding intravascular cells (stained by the iv injected α -CD45). **(C)** Flow cytometry dot plots of gated microglia illustrating the relative occupancy of cell surface P2X7 achieved by the endogenously produced nanobody (top, - Nb *ex vivo*) vs. the maximal occupancy achieved after *ex vivo* addition of saturating nanobody (bottom, + Nb *ex vivo*). **(D)** Bar diagrams

illustrating the level of P2X7 staining (mean fluorescence intensity, MFI) achieved on microglia by the endogenously produced nanobody vs. maximal staining achieved by 13A7-dim HLE added *ex vivo*. Data are shown for three mice that were injected with AAV-encoding P2X7-specific nanobodies vs. three mock-injected mice. P values were calculated by two-way ANOVA, followed by Bonferroni post-test. **(E)** Overlaid histograms illustrating the blockade of ATP-induced DAPI uptake in microglia achieved by the endogenously produced 13A7-dim HLE. **(F)** Bar diagrams illustrating the blockade of ATP-induced DAPI uptake in microglia achieved by endogenously produced nanobodies vs. exogenously added nanobodies. Data are shown for two mice that were injected with AAV-encoding P2X7-specific nanobodies vs. two mock-injected mice. P values were calculated by two-way ANOVA, followed by Bonferroni post-test.

The results of the flow cytometry analysis show that *in vivo* produced 13A7-dim HLE achieved extensive but not full occupancy of microglia (Fig. 16C, D). Consistently, the sustained *in vivo* expression of 13A7-dim HLE led to a significant partial blockade of the ATP-induced DAPI uptake in microglia (Fig. 16E, F).

Fig. 17 shows the results of the corresponding analyses of renal Th cells. The strategy used to gate parenchymal and intravascular kidney leukocytes is illustrated in Fig. 17A. The results show that P2X7 occupancy was essentially complete on both tissue resident (CD69+) and intravascular (CD69-) T helper cells in the kidney (Fig. 17B-D). The results of the ELISA assay reveal serum concentrations of 13A7-dim HLE in the three mice analyzed ranging from 25 $\mu\text{g/ml}$ to 48 $\mu\text{g/ml}$ (Fig. 18). These concentrations corresponded to those obtained 4 h after intravenous injection of doses of 13A7-dim HLE between 32 μg and 100 μg (see above, Fig. 14B).

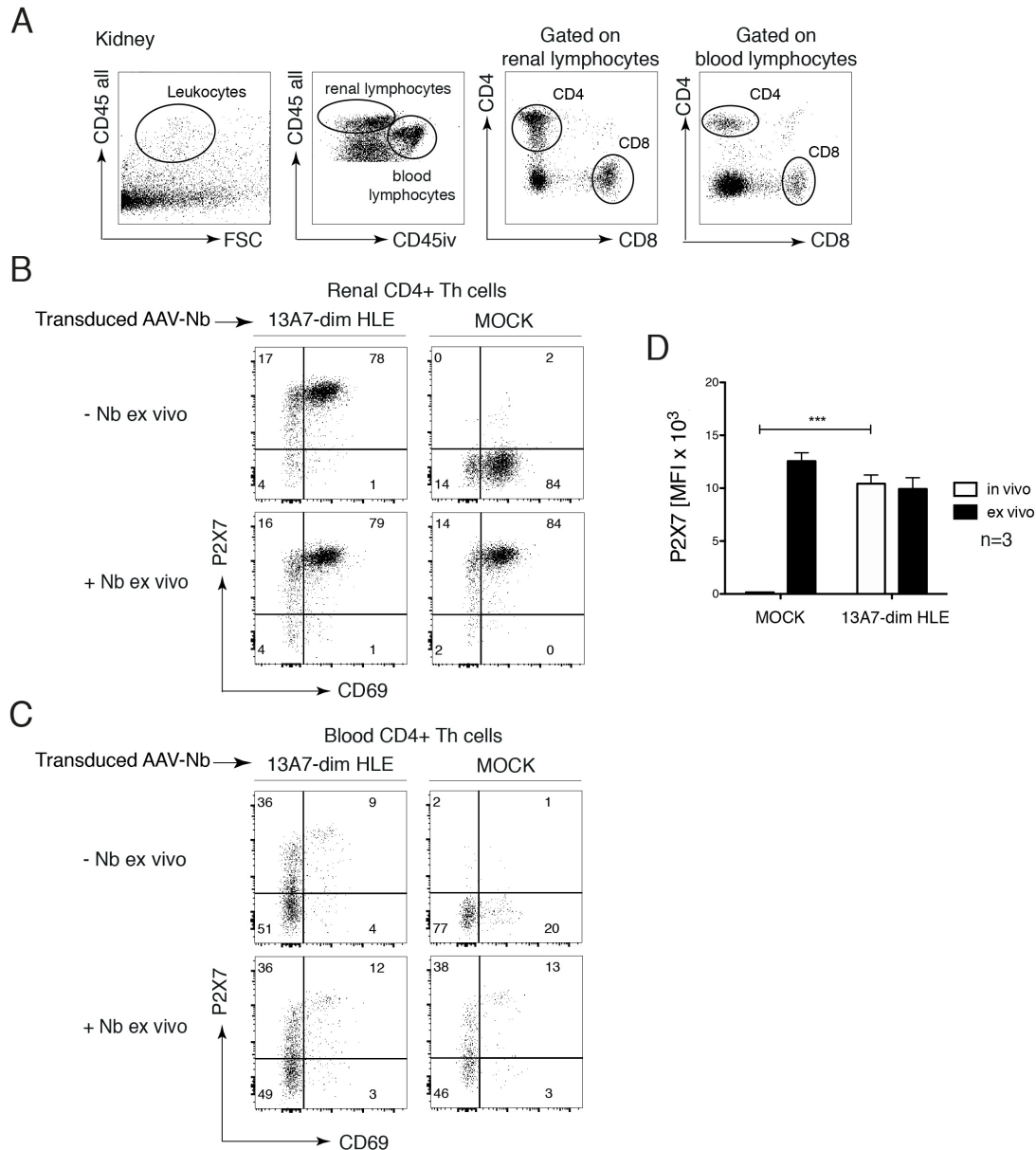


Figure 17. 190 days after intramuscular injection of 13A7-dim-HLE encoding AAV vectors, endogenously produced nanobodies are bound to P2X7 on renal CD4+ T cells. AAV encoding 13A7-dim HLE were injected into the gastrocnemius muscle of C57BL/6 mice as described in Fig. 16. 190 days later, occupancy of P2X7 on renal T cells was assessed by flow cytometry following the strategy shown in Fig. 11. **(A)** Parenchymal and vascular leukocytes were identified respectively by gating of cells stained or not by the iv injected α -CD45. Helper T cells were identified by a positive staining with α -CD4. Cells were counterstained with fluorochrome labeled antibodies against CD8 (as a marker of cytotoxic T cells) and CD69 (as a marker of tissue residency). **(B, C)** Flow cytometry dot plots of parenchymal **(B)** and intravascular **(C)** Th cells illustrating relative occupancy of P2X7 obtained by the endogenously produced nanobody (top, -Nb *ex vivo*) vs. the maximal occupancy of P2X7 achieved after *ex vivo* addition of an excess of the same nanobody (bottom, +Nb *ex vivo*). **(D)** Bar diagrams illustrating the level of P2X7 staining (mean fluorescence intensity, MFI) achieved on parenchymal Th cells by the endogenously produced nanobody vs. maximal staining achieved by the nanobody added *ex vivo*. Data are shown for three mice that were injected with AAV-encoding P2X7-specific nanobodies vs. three mock-injected mice. P values were calculated by two-way ANOVA, followed by Bonferroni post-test.

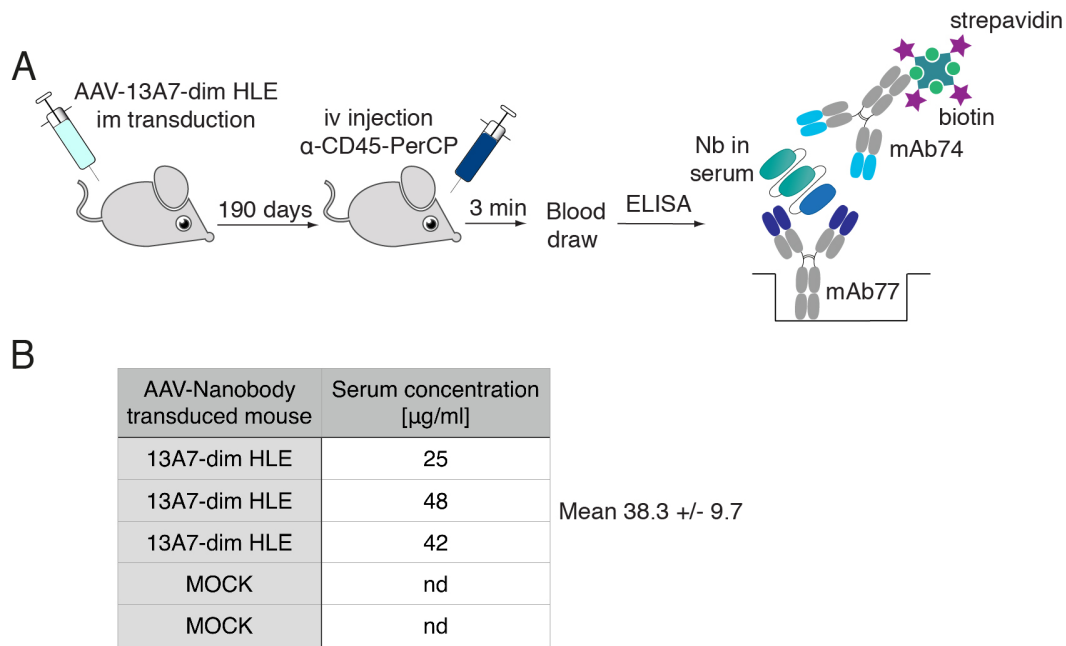


Figure 18. The concentration of 13A7-dim HLE in serum 6 months after injection of AAV is similar to that seen 4 hours after intravenous injection of 30 μg 13A7-dim HLE. (A) Schematic diagram of the experimental set up: AAV encoding 13A7-dim HLE were injected intramuscularly as illustrated in Fig 16A. 190 days later, mice were sacrificed and the concentration of soluble unbound nanobody in serum was determined by sandwich ELISA using mAb77 as catcher. Bound 13A7-dim HLE was detected using biotinylated mAb74 followed by HRP-conjugated streptavidin. **(B)** Table illustrating the calculated serum concentration (in $\mu\text{g}/\text{ml}$) of unbound nanobody 13A7-dim HLE in three AAV-injected and two mock-injected mice. nd = not detectable (same as background).

3.3.6 Intracerebroventricular (icv) injection of 1c81-dim^{sh} HLE allows a 100-fold reduction of the iv dose to achieve full P2X7 occupancy on microglia

The results obtained so far indicate that the BBB restricts the access of intravenously administered nanobodies into the CNS. Intracerebroventricular administration of drug molecules bypasses the BBB. To evaluate the efficacy of this route of injection for P2X7-blocking nanobodies, we carried out a dose response analysis with 1c81-dim^{sh} HLE and assessed the degree of P2X7 occupancy on microglia. The experimental set up is illustrated schematically in Fig. 19A. Titrated quantities of nanobody (10 - 240 μg in 5 μl saline) were injected directly into the ventricles of the brain using a stereotaxic apparatus.

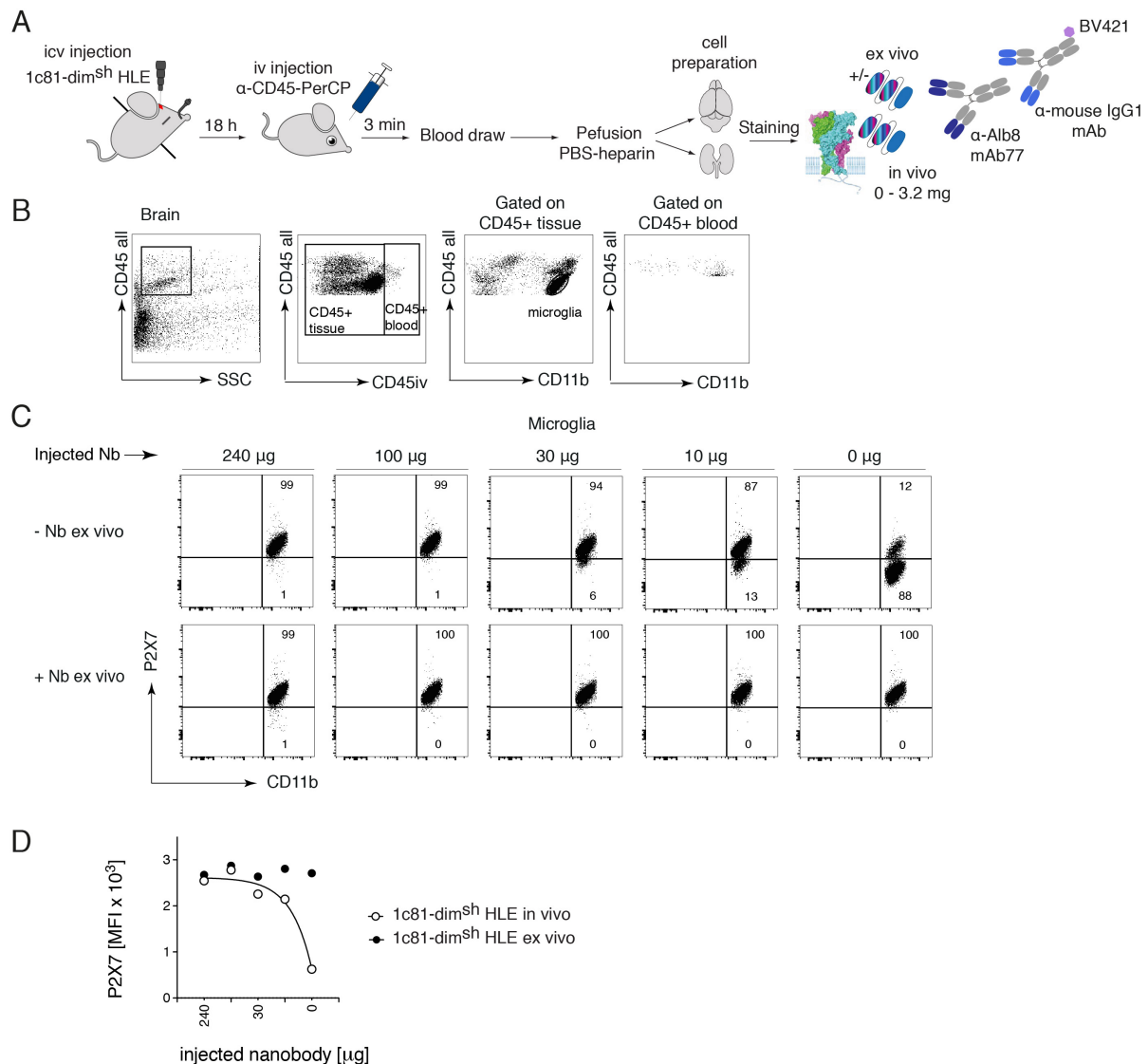


Figure 19. Full occupancy of P2X7 on microglia is achieved by a low dose ($> 10 \mu\text{g}$) of icv injected 1c81-dim^{sh} HLE. (A) Schematic diagram of the experimental set up: Titrated doses of 1c81-dim^{sh} HLE were injected intracerebroventricularly into C57BL/6 mice (in $5 \mu\text{l}$ saline). 18 h later and 3 min before sacrifice; a PerCP-conjugated CD45-specific antibody was injected intravenously to stain intravascular leukocytes. Brain cells were prepared and the degree of P2X7 occupancy on microglia was assessed by flow cytometry as detailed in Fig. 11. **(B)** Microglia were identified by sequential gating of CD45^{int} and CD11b^{high} cells and by excluding intravascular cells (stained by the iv injected α -CD45). **(C)** Flow cytometry dot plots of gated microglia illustrating the relative occupancy of cell surface P2X7 by the injected nanobody (top, -Nb ex vivo) vs. the maximal occupancy achieved after ex vivo addition of saturating nanobody (bottom, +Nb ex vivo). **(D)** Graph showing the level of P2X7 staining on microglia vs. the dose of injected nanobody. Open circles = staining obtained by the injected nanobody (in vivo), closed circles = maximal staining achieved after addition of nanobody (ex vivo).

Brain microglia were analyzed for P2X7 occupancy by the infused nanobody 18 h after icv injection using flow cytometry (Fig. 19). The gating strategy is shown in Fig. 19B (The small population of CD45^{high} CD11^{high} cells was again excluded from the analysis

as they may represent recent vascular immigrants). The results show that doses of 100 μg (5 mg/Kg) or more sufficed to fully occupy P2X7 on microglia (Fig. 19C). Remarkably, lower doses of 30 μg (1.5 mg/Kg) or 10 μg (0.5 mg/Kg) also resulted in extensive P2X7 occupancy on microglia. The calculated EC50 is $< 10 \mu\text{g}$. Some background staining of P2X7 was observed on cells of the PBS-injected control mouse (0 μg) (Fig. 19C-D).

To assess whether any of the icv injected nanobodies leaked into peripheral circulation, renal T cells were also analyzed for occupancy of P2X7 18 h after icv injection of nanobodies (Fig. 20) and serum was analyzed by ELISA for soluble unbound nanobodies (Fig. 21). Surprisingly, the results show a substantial degree of P2X7 occupancy on kidney-resident T cells 18 h after icv-administration at all doses of 1c81-dim^{sh} HLE analyzed (Fig. 20B-D).

Soluble unbound nanobody circulating in the serum at the moment of analysis (18 h) were analyzed by sandwich ELISA as described before (Fig. 21A). The measured concentration of 1c81-dim^{sh} HLE in serum was 1.3 $\mu\text{g/ml}$ after icv injection of the highest dose (240 μg) (Fig. 21B). This concentration was comparable to that measured 4 h after intravenous injection of 10 μg 13A7-dim HLE (see Fig. 14B above). For lower icv-injected doses, the measured serum levels of nanobody were near the detection limit, between 0.1 $\mu\text{g/ml}$ to 0.4 $\mu\text{g/ml}$ (Fig. 21B).

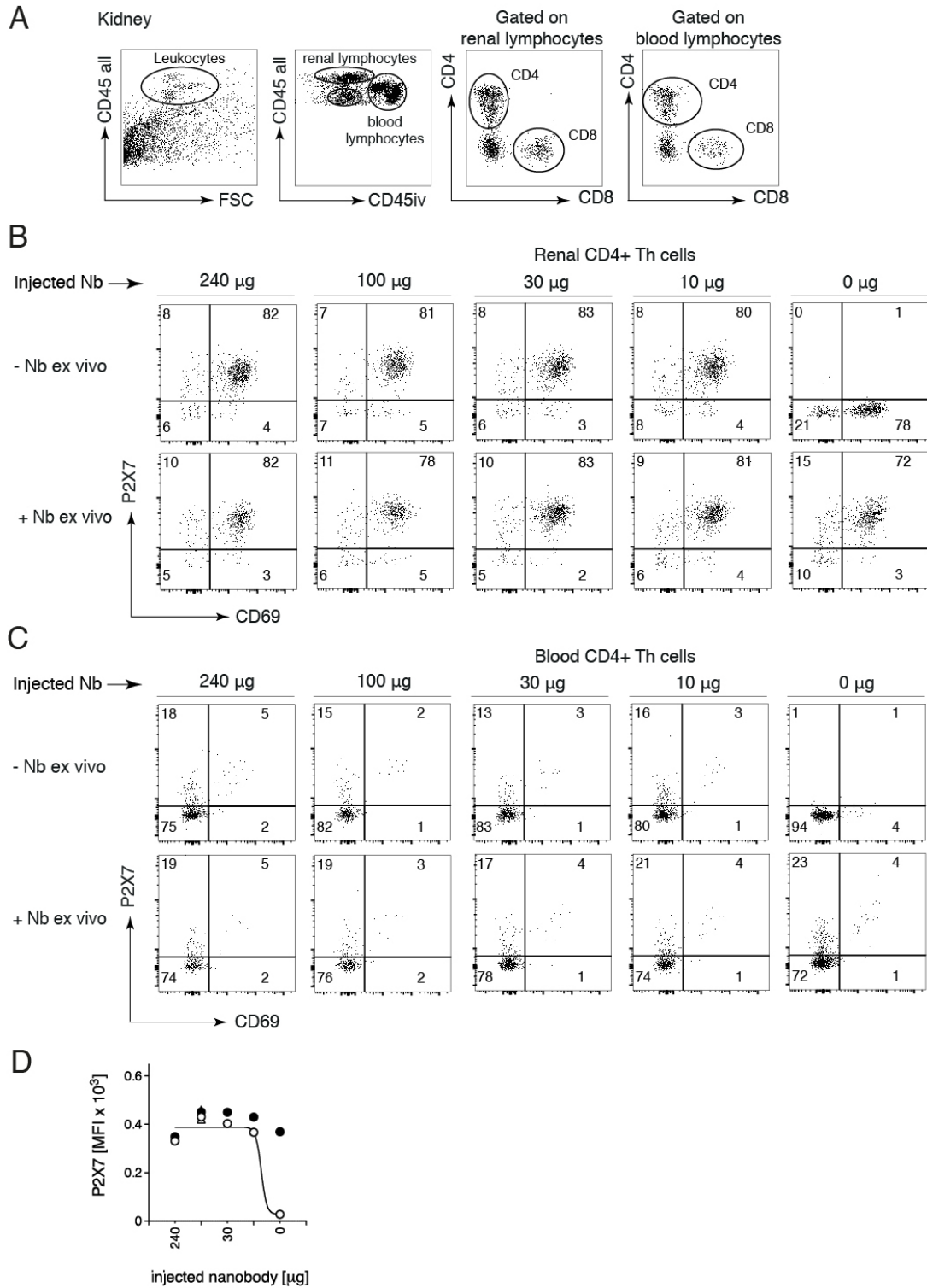


Figure 20. Full occupancy of P2X7 on renal CD4+ T cells is achieved by a low dose (> 10 μ g) of icv injected 1c81-dim^{sh} HLE. Titrated doses of 1c81-dim^{sh} HLE were injected intracerebroventricularly into C57BL/6 mice (in 5 μ l saline) as illustrated schematically in Fig. 19. Mice were sacrificed 18 h later and renal T cells were analyzed for occupancy of cell surface P2X7. **(A)** Parenchymal and vascular leukocytes were identified respectively by gating of cells stained or not by the iv injected α -CD45. Helper T cells were identified by positive staining with α -CD4. Cells were counterstained with fluorochrome labeled antibodies against CD8 (as a marker of cytotoxic T cells) and CD69 (as a marker of tissue residency). **(B, C)** Flow

cytometry dot plots of parenchymal **(B)** and intravascular **(C)** Th cells illustrating relative occupancy of P2X7 obtained by the injected nanobody (top, - Nb *ex vivo*) vs. the maximal occupancy achieved after *ex vivo* addition of saturating nanobody (bottom, + Nb *ex vivo*). Graph illustrating the degree of P2X7 staining on parenchymal CD4⁺ T cells vs. the dose of injected nanobody. Open circles = staining obtained by the injected nanobody *in vivo*, closed circles = maximal staining achieved after addition of nanobody *ex vivo*.

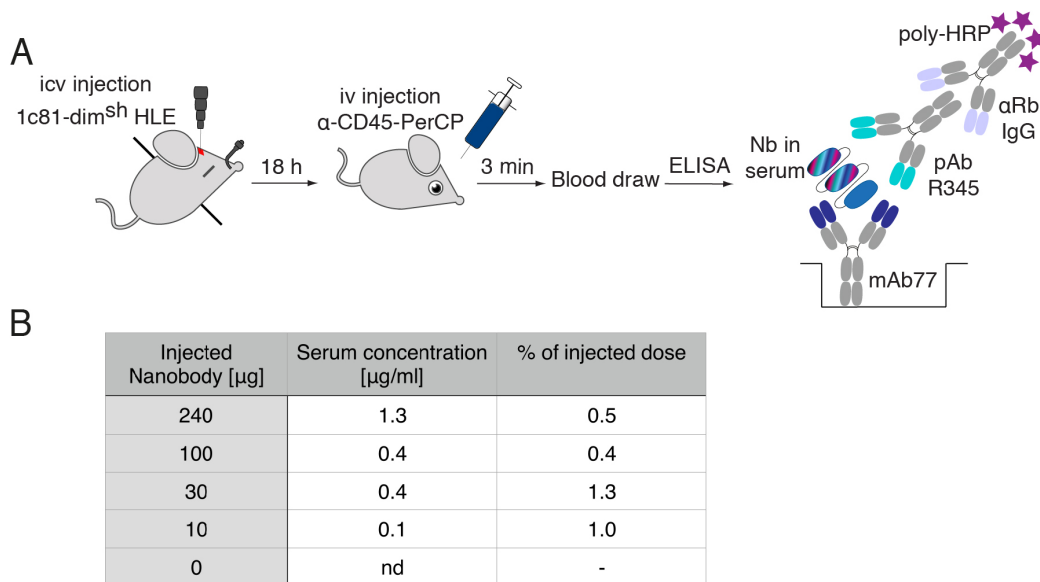


Figure 21. Only very low concentrations of unbound 1c81-dim^{sh} HLE (< 2 μg/ml) can be detected in serum 18 h after icv administration. (A) Schematic diagram of the experimental set up: 18 h after icv instillation of titrated quantities of 1c81-dim^{sh} HLE (Fig. 14A), mice were sacrificed and the concentration of soluble unbound nanobody in serum was determined by sandwich ELISA using mAb77 as catcher. Bound 1c81-dim^{sh} HLE was detected using pAb R345 followed by HRP-conjugated α-rabbit IgG. **(B)** Table illustrating the calculated serum concentration (in μg/ml) of unbound nanobody 1c81-dim^{sh} HLE vs. the dose of icv injected nanobody. nd = not detectable (same as background).

3.3.7 A low dose of bivalent HLE nanobodies achieved full occupancy of P2X7 on microglia 48 h following icv administration

Finally, we assessed whether full occupancy of P2X7 on microglia by 13A7-dim HLE and 1c81-dim^{sh} HLE could be achieved even 48 h after administration via the icv route. For this, we icv-injected 50 μg of each nanobody construct into mice and analyzed P2X7 occupancy on microglia 48 h later by flow cytometry (Fig. 22). The results show that both nanobodies, indeed, still achieve full occupancy of P2X7 on microglia 48 h after icv administration (Fig. 22B).

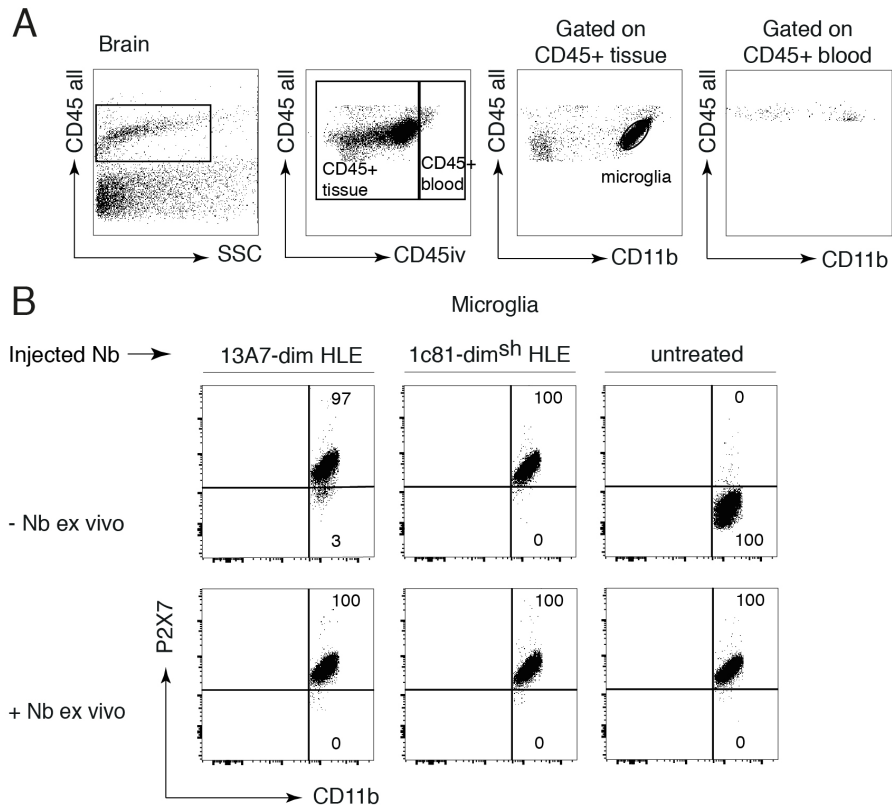


Figure 22. 48 h following icv administration, a low dose of bivalent HLE nanobodies achieved full occupancy of P2X7 in microglia. Two mice were injected icv with 50 μg of either 13A7-dim HLE or 1c81-dim^{sh} HLE. 48 h later, the degree of P2X7 occupancy on microglia was evaluated by flow cytometry as detailed in Figs. 7 and 14. **(A)** Microglia were identified by sequential gating of CD45^{int} and CD11b^{high} cells and by excluding intravascular cells (stained by the iv injected α -CD45). **(B)** Flow cytometry dot plots of gated microglia illustrating the relative occupancy of cell surface P2X7 by the injected nanobody (top, - Nb *ex vivo*) vs. the maximal occupancy achieved after *ex vivo* addition of saturating nanobody (bottom, + Nb *ex vivo*).

4. Discussion

The present study evaluated the ability of engineered P2X7-antagonistic nanobodies to penetrate *in vivo* the blood brain barrier (BBB) and peripheral endothelial barriers to engage P2X7 on tissue resident immune cells of the brain and kidney that express high levels of P2X7, i.e. brain microglia and renal T helper cells. The results confirm that nanobodies, as small single domains, represent excellent modules for engineering: bivalent P2X7-antagonistic nanobodies with an extended half-life were sequence optimized in order to improve solubility and isoelectric point (pI). *In vitro* assays confirmed that the functional potency of the engineered nanobodies was not compromised by engineering. A flow cytometry methodology was established to determine the level of P2X7 occupancy achieved by these nanobodies on microglia and renal T helper cells (Th) *in vivo*. The results show that penetration of the engineered nanobodies from the circulatory compartment into peripheral tissue is 100-fold more efficient than penetration into brain tissue. In the following section, the obtained results will be discussed in detail, considering in particular the developability of nanobodies as therapeutic proteins or research tools.

4.1 Engineering and production of P2X7-antagonistic nanobodies

Nanobodies 1c81 and 13A7, generated in the Koch-Nolte lab, are potent antagonists of mouse P2X7. These nanobodies effectively inhibit both, ATP and NAD⁺ induced activation of P2X7 *in vitro*.

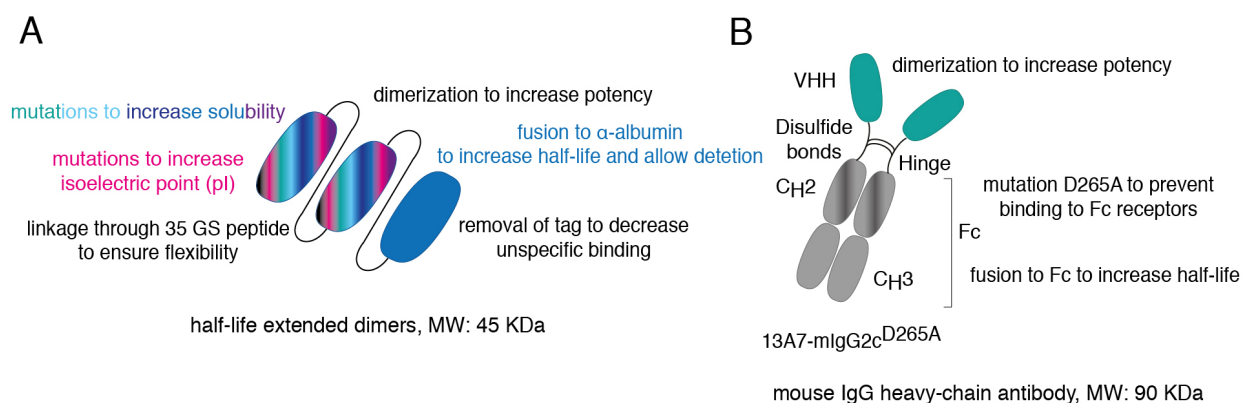


Figure 23. Schematic representation of the engineered bivalent P2X7-specific nanobodies analyzed in this thesis. (A) Modifications introduced into constructs of Nb 1c81 as heterotrimeric constructs connected by flexible linkers and lacking an Fc domain. **(B)** Modifications introduced into a heavy chain construct of Nb 13A7.

Dimers of these nanobodies were generated to increase binding affinity and thereby potency (Fig. 23). These dimers were then fused to an albumin-specific nanobody to increase their *in vivo* half-life. The resulting trimeric constructs have a size of 45 kDa and each nanobody domain is connected to the next one via a 35 Gly-Ser linker to ensure flexibility (Fig. 23A). To test whether brain penetration depends on the pI (Li et al., 2012; Li et al., 2016), two positions in the framework region 1 and 4 (FR1, FR4) of nanobody 1c81 were mutated into positively charged residues. Five additional mutations were introduced to increase solubility and the C-terminal hexahistidine tag was removed to decrease unspecific binding. Nanobody 13A7 in turn was fused to the hinge, C_H2 and C_H3 domains of mouse IgG2c, yielding bivalent heavy chain antibody of ~ 90 kDa with reduced passage across the glomerular filtration barrier. The substitution D265A was introduced into the C_H2 domain to prevent binding to Fc receptors and prevent undesired Fc-mediated effector functions, including complement and cell dependent cytotoxicity (CDC, ADCC) (Fig. 23B).

Nanobody ID	stability	isoelectric point (pI)	C-terminal tag
13A7-dim HLE	high solubility	5.9	His-myc
13A7-mIgG2c ^{D265A}	high solubility	5.7	Fc portion
1c81-dim HLE (wt)	poor solubility	8.1	His-myc
1c81 ^{sh} -dim HLE	high solubility	8.5	SNB tag
1c81 ^s -dim HLE	high solubility	9.7	tagless

Table 5. Physicochemical properties of the engineered nanobodies. The nanobody ID indicates the name and format of the P2X7-specific nanobody, i.e. as nanobody dimers (dim) or heavy chain antibody (mIgG2c). Mutations to increase solubility (s), isoelectric point (h), and to abolish Fc-receptor binding (D265A) are indicated in superscript. The stability in solution was assessed by analyzing the turbidity of highly concentrated nanobody solutions. The calculated isoelectric point and the C-terminal tags are also indicated.

Table 5 summarizes the physicochemical properties of the resulting bivalent half-life extended P2X7-antagonistic nanobodies. The nanobody ID indicates the format and specifies the mutations that were introduced. Only 1c81-dim HLE (wt) is tagless, 1c81-dim^{sh} HLE has two copies of a high pI peptide tag (SNB-tag) to further increase the pI. These nanobody constructs were successfully produced and purified from transiently transfected HEK-6E cells in high yields and purity. Physicochemical analyses showed improved solubility at high concentration of the stabilized variants of 1c81 (1c81^s and

1c81^{sh}) compared to the parental 1c81-dim HLE (wt), indicating that we succeeded in optimizing 1c81 solubility. The pI determined by isoelectric focusing gel electrophoresis was consistent with the theoretical calculation.

The specificity and functional potency of the engineered nanobodies was characterized *in vitro*. Dimeric half-life extended nanobodies has shown to bind P2X7 with high specificity. That is, nanobodies bound to HEK cells transfected with P2X7 and did not show any detectable binding to HEK cells transfected with P2X1 or P2X4, the closest paralogs of P2X7 and untransfected cells. With respect to nanobody function, the bivalent half-life extended P2X7-specific nanobodies effectively blocked ATP-induced Ca²⁺ influx in P2X7 expressing HEK cells at nanomolar potencies (IC₅₀ between 0.9 and 3.1 nM). A comparison of the blocking potencies between the monovalent and the bivalent format of P2X7-specific nanobodies, revealed a 10-fold increase in the potency of the bivalent version, supporting the hypothesis that dimerization increases potency. The release of IL1-β by LPS-primed primary microglia was also blocked with high potency, with IC₅₀ values ranging between (0.6 - 3.3 nM). Moreover, 13A7-dim HLE effectively antagonized inflammasome activation in primary macrophages at a concentration of 100 nM.

4.2 Potential advantages and limitations of engineered nanobodies

	engineered nanobodies	lipidized small molecules
size	45 KDa	> 1KDa
specificity	high	variable, usually low
potency	high	variable, usually low
off-target effects	none	P1, P2, kinases, ATPases, deshydrogenases
<i>in vivo</i> half-life	adjustable by fusion to albumin-specific nanobody	short
metabolites	non-toxic biodegradable	potentially toxic
tissue penetration	efficient in periphery	variable

Table 6. Potential advantages and limitations of P2X7-antagonistic nanobodies vs. lipidized small molecules inhibitors. Adapted from (Menzel et al., 2018).

Table 6 summarizes potential advantages and limitations of the engineered nanobody constructs vs. small molecule drugs.

Small-lipophilic P2X7 inhibitors developed for CNS indications have shown benefit in different models of neuropathic pain. However, these compounds display moderate P2X7-blocking potencies, conversion to toxic metabolites, and rapid clearance. Engineered nanobodies pose an attractive alternative to address these issues. First, they block P2X7 with a high potency. Second, owing to their high specificity, they lack off-target effects. Third, since they are biodegradable, they are less toxic for *in vivo* applications. Finally, their extended *in vivo* half-life can ensure a prolonged P2X7 engagement. Nevertheless, since the BBB excludes large-sized molecules, the size of the engineered nanobodies (45 kDa) might limit their penetration into tissue, in particular brain tissue. While an increase in the pI of the nanobody might facilitate permeation into the brain by interaction with the negatively charged glycocalyx at the surface of the BBB, it might also increase stickiness to untargeted endothelia and cell membranes that are also composed by glycocalyx. Moreover, it has been shown that the glomerular filtration rate increases upon increasing pI and decreasing size (Venkatachalam and Rennke, 1978), which could cause a faster filtration of the high pI nanobodies. The half-life extension module is expected to counteract this effect.

4.3 Occupancy of P2X7 brain microglia and renal T cells by intravenously injected nanobodies

The efficacy of nanobodies to engage their target P2X7 at sufficient levels and thereby exert their blocking effect depends on their *in vivo* tissue penetration. We hypothesized that our engineered nanobodies would traverse readily across peripheral endothelial barriers; but that the passage across the brain endothelium would be limited. To test these hypotheses, a new flow cytometry methodology was established to measure occupancy of P2X7 by injected nanobodies on tissue resident immune cells. Thus, following intravenous administration of nanobodies to C57BL/6 mice, the level of occupancy of P2X7 on cells of the immune system that reside in the brain (microglia, CD45+/CD11b-) and kidney (Th, CD45+/CD69+) was analyzed and related to the maximal occupancy achieved by *ex vivo* addition of the same nanobody. This method permits an assessment of tissue penetration of nanobodies by providing a quantitative measure of P2X7 occupancy by nanobodies on specific cell populations by flow cytometry.

It was important to take into account that blood may contain excess of unbound nanobody that could potentially bind to P2X7 on tissue resident cells upon tissue disruption during cell preparation. To avoid this, an extensive transcordial perfusion was performed in this study. While transcordial perfusion effectively eliminates serum and erythrocytes, vascular leukocytes reportedly are not effectively removed by perfusion (Anderson et al., 2014). In order to distinguish parenchymal leukocytes from intravascular leukocytes, we used a strategy to specifically stain intravascular leukocytes (Anderson et al., 2014) by injecting a fluorochrome-conjugated α -CD45 antibody 2-3 minutes prior to sacrifice and counterstaining, *ex vivo*, all leukocytes with a second fluorochrome-conjugated α -CD45 antibody after tissue disruption.

Using intravenous (iv) and intracerebroventricular (icv) routes of administration, the engineered nanobodies were injected to C57BL/6 mice in titrated doses and the degree of P2X7 occupancy was determined on both resident microglia and parenchymal Th cells of the kidney, recently described as tissue resident memory T cells (Trm).

Nanobody ID	pI	route of injection	effective dose to achieve full P2X7 occupancy (EC) (mg/kg)	
			Brain (microglia)	Kidney (Th cells)
13A7-dim HLE	5.9	intravenous	150	1.5
13A7-mlgG2c	5.7	intravenous	150	1.5
1c81-dim ^S HLE	8.5	intravenous	150	-
1c81-dim ^{sh} HLE	9.7	intravenous	150	1.5
		intracerebroventricular	1.5	0.5

Table 7. Assessment of target engagement of engineered P2X7-antagonistic nanobodies in brain microglia vs. renal Trm cells.

Table 7 summarizes the effective dose to achieve the maximal P2X7 occupancy (EC) 4h after iv and 18h after icv injections. The results show that 100-fold higher doses were required to fully occupy P2X7 on microglia than on renal Trm cells after iv injections. Consistently, an effective blockade of ATP-mediated DAPI uptake by microglia was achieved only with the highest dose of iv injected nanobodies analyzed (150 mg/kg), whereas in case of renal Trm cells, administration of 0.15 mg/kg of 13A7-dim HLE already sufficed to achieve an effective blockade of P2X7. These results

indicate that intravenously injected nanobodies translocate effectively through the renal endothelium but not the brain endothelium, suggesting that the less restrictive nature of the peripheral endothelium facilitates nanobody penetration.

These findings are consistent with studies on monoclonal antibodies, which also were found to barely cross the BBB after intravenous injection. Thus, in a preclinical study in mice, 0.7% of the injected dose of a radiolabeled monoclonal IgG1 antibody was quantified in the brain (Abuqayyas and Balthasar, 2013). In humans, after intravenous injection of rituximab (Rubenstein et al., 2003) and trastuzumab (Bousquet and Janin, 2014), the concentration of these antibodies in the cerebrospinal fluid (CSF) were at most 0.1% of the serum concentration. However, it has been reported that when cerebrovascular endothelial cells are exposed to a highly concentrated solution, cell shrinkage and subsequently widening of inter-endothelial tight junctions occurs making room for the bulk flow of the circulatory compartment to gain access into the brain (Rapoport, 2000).

Remarkably, neither the isoelectric point nor the size of the bivalent nanobody constructs analyzed here seemed to markedly improve *in vivo* targeting of P2X7 on microglia. Although, in case of 1c81, increasing the pI showed a slight tendency to achieve a higher P2X7 occupancy on microglia than its lower pI counterpart. In fact, similar EC values to achieve P2X7 occupancy on microglia following iv administration were observed with bivalent half-life extended nanobodies with low and high pIs and with small and larger sizes (Table 7). These results suggest that an increase in the pI does not enhance brain penetration in case of the bivalent half-life extended nanobodies analyzed here, unlike previous studies conducted by (Li et al., 2012; Li et al., 2016). In a first study, these authors demonstrated that iv injection of a high pI nanobody specific for the glial fibrillary acidic protein (GFAP) traversed the BBB, penetrated astrocytes and bound its intracellular target. Moreover, *in vitro*, large-sized nanobody-constructs showed a decreased passage across an *in vitro* blood brain barrier model (Li et al., 2012). In a second publication from the Lafaye's lab, they report the generation of two nanobodies, each respectively directed against extracellular amyloid deposits (α -A β) and intracellular tau neurofibrillary tangles (α -tau), the two core lesions of Alzheimer's disease (AD). The pI of these nanobodies was found to be basic. Four hours after intravenous administration in a mouse model of AD, the nanobodies crossed gradually the BBB, diffused into the brain and engaged their

respective targets. The authors proposed that nanobodies characterized by a high pI putatively cross the BBB by hijacking the adsorptive-mediated transcytosis pathway (AMT) (Li et al., 2016). The injected nanobody doses in these studies were also rather high (2 mg of α -GFAP, 1 mg of α -tau and 200 μ g of α -A β per mouse). The discrepancy between these findings and our results may be explained by the different sizes of the injected nanobodies. Thus, Li injected monomeric nanobodies (15 kDa), three times smaller than those used in our study (bivalent half-life extended nanobodies, 45 kDa). It is possible that penetration of nanobodies may depend on size and other intrinsic features of a nanobody in addition to pI.

On the other hand, with the icv route a \sim 100-fold lower dose of nanobody was required (1.5 mg/kg) to achieve effective occupancy of P2X7 on microglia than by the iv route (Table 7). Surprisingly, icv injections resulted also in occupancy of P2X7 on renal Trm cells. A possible explanation for this observation is that due to the rapid bulk motion of the CSF, the nanobody is transferred from the CSF into the bloodstream by convection (Christy and Fishman, 1961; Fishman and Christy, 1965; Pardridge, 2012). Physiologically, the fast rate of bulk flow of the CSF within the ventricular compartments creates a pressure that induces adsorption of the CFS onto the arachnoid villi and subsequently passage into the systemic circulation (Fig. 24). Moreover, the concentration gradient of the nanobody in the CSF vs. the bloodstream might facilitate its transport into the blood circulation.

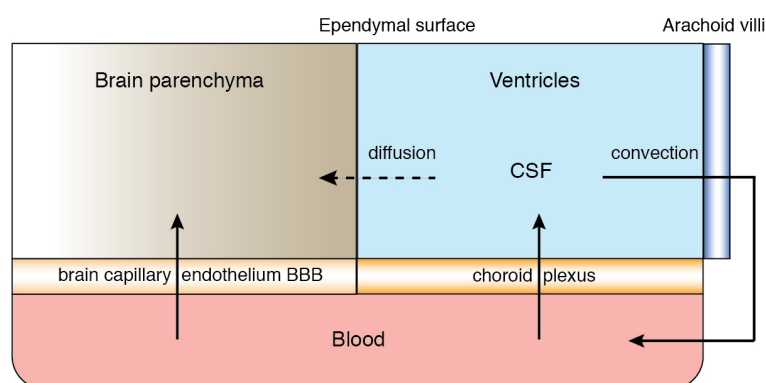


Figure 24. Transport of drug molecules following intracerebroventricular (icv) injection. Following icv injection, distribution of drugs into the brain parenchyma is limited by the slow rate of solute diffusion from the CSF across the ependymal surface. On the other hand, a rapid rate of bulk flow of the CSF allows its exit from the ventricles into the systemic circulation through the arachnoid villi. Adapted from Drug transport across the blood brain barrier (BBB) by (Pardridge, 2012).

A major disadvantage of this neurosurgical-based approach is its invasive nature, which could alter the characteristics of the tissue. Another limitation could be the slow rate of diffusion into the brain parenchyma from the site of injection. In case of icv infusions into the rat brain, the concentration of injected drugs was found to decrease up to 10-fold with each mm of distance away from the injection site (Pardridge, 2012). In this study, constructs 13A7-dim HLE and 1c81-dim^{sh} diffusion was allowed to proceed for 18 to 48 h following nanobody icv-infusion. The results show that after both time points, a full P2X7 occupancy was achieved, suggesting durability of the target engagement up to 48 h. It will be interesting to analyze the kinetics of nanobody redistribution after icv injections in more detail.

4.4 Occupancy of P2X7 brain microglia and renal T cells by endogenously produced nanobodies

The delivery of nanobodies by means of AAV-mediated gene transfer *in vivo* may be an attractive alternative to intravenous or intracerebroventricular injections. Accordingly, we transduced muscle cells of C57BL/6 mice with a single injection of 13A7-dim HLE-encoding AAV1. After 190 days, we measured brain and kidney penetration of the endogenously produced nanobody by determining the degree of P2X7 occupancy on microglia and renal Trm cells. The results showed that a single injection of nanobody-encoding AAV1 led to long-term *in vivo* production of the encoded nanobody and a complete P2X7 occupancy on renal Trm cells and extensive P2X7 occupancy on brain microglia. The concentration of the nanobody in serum at this time was equivalent to the concentration obtained 4 h after an intravenous injection of 30-100 μg . The results further indicate that the nanobody-encoding transgene was efficiently expressed and secreted by transduced muscle cell in sufficient amounts to translocate through the peripheral endothelium and to engage all available P2X7 on renal T cells. These results indicate that this delivery system is efficient in the periphery. However, it might be necessary to adjust the conditions of the AAV-mediated nanobody delivery *in vivo* in order to achieve full P2X7 engagement on microglia. To this end, it will be interesting to determine whether higher doses, other AAV-isotypes, and/or local delivery of AAVs result in improved occupancy of P2X7 on microglia.

One limitation of AAV mediated gene transfer is the immunogenicity of the viral capsid to many host species. Thus, preexisting AAV-neutralizing antibodies and CD8+ T cells directed to AAV capsid antigens can diminish the transduction rates and cause rejection of AAV-transduced cells. In therapeutic applications, this may require treatment with immunosuppressant drugs (Ertl, 2017). Interestingly, the AAV9 serotype results in transduction of neurons following intravenous injection of juvenile mice, however at lower efficiency in adult mice (Foust et al., 2009). Since it is possible to adjust the tropism of the AAVs by modifying the capsid, (Deverman et al., 2016) it may be possible to select AAVs for improved penetration into the brain after intravenous injection.

4.5 Other strategies to improve penetration of nanobodies through the BBB

An elegant strategy to overcome the BBB is the engineering of brain shuttles (Fig. 25).

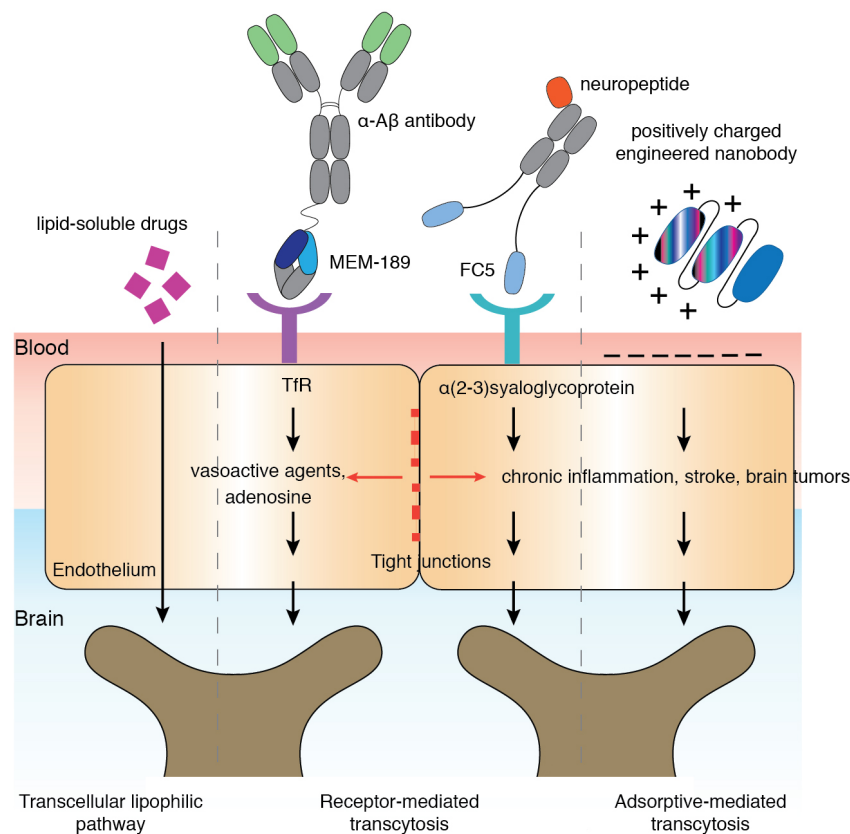


Figure 25. Strategies for facilitating transport of biologics across the BBB. Receptor-mediated transcytosis pathways can be hijacked using receptor-specific antibodies to deliver covalently associated biologics across the BBB into the brain. Adapted from Astrocyte-endothelial interactions at the blood brain barrier by (Abbott et al., 2006).

Brain shuttles are bi-specific molecules in which one module consists of an antibody, antibody fragment or nanobody that engages a transcytosis receptor on the BBB and the second module is any kind of cargo-molecule that recognizes a therapeutic target within the CNS. Brain shuttles undergo receptor-mediated transcytosis (RTM) across the BBB, thereby allowing transport of cargo from the circulatory compartment into the brain parenchyma (Stanimirovic et al., 2014). Antibodies or antibody-fragments with specificity for the transferrin (TfR) receptor have been developed as BBB carriers. Roche showed in a mouse model of Alzheimer's disease that an α -A β monoclonal antibody (mAb) fused to a single α -TfR antigen binding fragment (Fab) was transported into the brain parenchyma and cleared β -amyloid plaques. Moreover, the authors showed that monovalent binding of the TfR facilitated transcellular transport, whereas a higher avidity bivalent binding mode led to lysosome sorting (Niewoehner et al., 2014) (Fig. 25). A possible limitation may be that in the periphery, binding of the TfR by this brain shuttle cause first infusion reaction mediated by the Fc portion of the α -A β antibody. However, the authors did not observe any sign of first infusion, probably due to steric hindrance in the Fc binding to the Fc receptors (FcR) (Weber et al., 2018). The same group designed highly potent BACE 1 peptide inhibitors that were conjugated to the mentioned brain shuttle targeting the TfR and demonstrated to reduce brain A β plaques in mice following intravenous injection (Ruderisch et al., 2017). Recently, brain shuttles based on shark single domain antibodies specific for the TfR-1 showed efficient transport of therapeutic antibodies into the brain parenchyma (Greenwood et al., 2017).

Nanobodies can also serve as BBB carriers. Thus, nanobodies FC5 and FC44, which were selected to bind and internalized human cerebrovascular endothelial cells (HCEC) in a vitro BBB model, were detected in the brain parenchyma following intravenous administration into mice (Muruganandam et al., 2002). In another study, FC5 was engineered as a monovalent and bivalent fusion with a human Fc domain. The bivalent fusion showed increased rate of transcytosis across an *in vitro* BBB model and enhanced brain exposure after systemic dosing in rats. In the Hargreaves model of inflammatory pain, systemic injection of FC5-Fc fusion protein chemically conjugated with impermeable neuropeptides potentially improved the pharmacological potency. Similarly, optimized nanobody-based cyclic peptides that target the LDL

receptor improved transport of poor brain penetrating small molecule drugs and therapeutic antibodies (Zhang et al., 2013).

Finally, as mentioned above, the cationization of biologics to increase brain penetration is a strategy to use judiciously, since it has shown to be efficient only under certain conditions. For instance, sufficient target engagement in the CNS by injected basic nanobodies seems to correlate with a reduced size and high dose (Li et al., 2012; Li et al., 2016).

Another invasive strategy to deliver molecules into the brain is to transiently open the BBB by means of vasoactive agents. Such agents are infused via the intracarotid artery inducing an osmotic pressure and thereby reversibly disrupting the BBB by shrinkage of the vascular endothelial cells, vasodilatation and contraction of the interendothelial tight junctions to an estimated radius of 200 Å. This effect is reversible in a short time. This procedure has been used for the delivery of a broad range of water-soluble drugs including large molecules such as antibodies (Rapoport, 2000) (Fig. 25). The disadvantage is that in both animal models and humans, the use of this procedure induced neuropathologic side effects such as vasculopathy and seizures (Pardridge, 2005). A leaky BBB also allows entry of plasma proteins such as albumin that are toxic to brain cells (Nadal et al., 1995). A similar strategy uses agonists of the adenosine receptors (AR), such as adenosine, to mediate opening of the BBB. Thus, activation of the ARs, expressed on the vascular endothelial cells, induce BBB permeability in a transient manner that depends on the half-life of the agonist. To use this strategy, we should consider that since adenosine is generated through the ATP catabolism by CD39 and CD73, the availability of adenosine requires a tight regulation of these enzymes. As a perspective, a better understanding of the signaling cascades leading to BBB opening may open new pathways for delivering biologics to the brain (Bynoe et al., 2015).

It is important to consider that the delivery of drug molecules to the brain may be facilitated when the BBB is compromised, as in pathophysiological conditions. For instance, a loss of the BBB integrity was observed during the pathogenesis of disorders such as Multiple sclerosis (MS), stroke and brain cancer.

4.6 Perspectives

This work represents the first attempt to optimize P2X7-antagonistic nanobodies by genetic engineering with the goal of increasing brain penetration. A robust flow cytometry methodology was established to assess brain penetration by determining the level of target occupancy on specific cell populations. Thereby, we could define experimentally the conditions that allow brain penetration of injected nanobodies. It would be valuable to complement these results by visualization of P2X7 occupancy on native brain and renal tissues to provide information about the cellular localization of P2X7-bound nanobodies as well as the areas of high binding density following *in vivo* administration, e.g. by measuring P2X7 occupancy on tissue sections by microscopy. Since biological specimens are tridimensional, it would be interesting to achieve volumetric imaging of P2X7 occupancy in whole organs or thick tissue samples in order to obtain further information on the specific localization of the P2X7-bound nanobody within the tissue structure. For deep tissue imaging, emerging tissue clearing techniques may present a path to obtain sharp images (Richardson and Lichtman, 2015).

Even after sequence optimization, much higher doses of nanobodies were required to achieve maximal occupancy of P2X7 after administration by the intravenous route than by the intracerebroventricular route. To ensure clinical efficacy of P2X7-antagonistic nanobodies for the treatment of CNS disorders in which P2X7 plays a pivotal role, further optimization steps will be required to enhance brain penetration and to achieve sufficient target engagement. For example, a TfR-based shuttle system might be used to deliver P2X7-antagonistic nanobodies to the brain. The results of this thesis provide a basis for rational design and validation of improved brain penetrating nanobodies.

5. Abstract

P2X7 is a homotrimeric ion channel expressed by immune cells. In LPS-primed myeloid cells such as monocytes and microglia, gating of P2X7 by ATP induces assembly of the inflammasome, leading to the release of mature interleukin IL-1 β . Moreover, P2X7 activation leads to macropore formation in the plasma membrane. Nanobodies (Nbs) are a novel class of therapeutic proteins based on the antigen-binding domains of heavy chain antibodies that naturally occur in Camelids. Nanobodies offer advantages over conventional antibodies: **(1)** as soluble single domains they are easily reformatted into bi- and multispecific reagents, and **(2)** their small size facilitates tissue penetration. The Koch-Nolte lab has generated Nbs that specifically antagonize P2X7 and show benefit in animal models of inflammation. The extent to which these nanobodies reach P2X7 on the surface of tissue resident immune cells *in vivo* is not yet known.

The goal of this study was to determine whether P2X7-antagonistic Nbs penetrate peripheral endothelial barriers and the highly restrictive blood brain barrier (BBB) to reach and bind P2X7 on tissue resident immune cells. P2X7-specific Nbs were sequence optimized to improve solubility and to raise the isoelectric point (pI), were dimerized by genetic fusion to increase binding affinity, and were genetically fused to an albumin-specific Nb to extend their *in vivo* half-life. Following the verification of the P2X7 antagonistic effects of the engineered Nbs *in vitro*, Nbs were intravenously (iv) or intracerebroventricularly (icv) injected at different doses into mice and the degree of P2X7 occupancy on brain microglia and renal T helper (Th) cells was evaluated by flow cytometry at different time points after administration. In parallel, the efficacy of the injected nanobodies to block ATP-mediated pore formation was analyzed. Following iv injections of nanobodies, a 100-fold higher dose was required to fully occupy P2X7 on brain microglia (150 mg/kg) than that on renal parenchymal Th cells (1.5 mg/kg). In contrast, 100-fold lower doses were sufficient to achieve full occupancy on microglia following icv administration of the same Nbs. In an alternative approach, muscle cells of mice were transduced with Nb-encoding AAV-vectors to induce long term *in vivo* expression of the engineered Nbs. The results showed that the endogenously produced Nbs (almost) fully occupied P2X7 on microglia and renal parenchymal Th cells 6 months after im injection of AAVs.

6. Zusammenfassung

P2X7 ist ein homotrimerer Ionenkanal, der von Immunzellen exprimiert und durch extrazelluläres ATP geöffnet wird. Dies führt auf LPS-stimulierten Monozyten und Microglia zur Ausbildung des NALP3 Inflammasoms, der Prozessierung und Freisetzung des proinflammatorischen Zytokins IL1- β , und zur Ausbildung von Poren in der Plasmamembran. Nanobodies, die Antigen-bindenden Domänen der Kameliden Schwerekettenantikörper, weisen einige Vorteile gegenüber konventionellen Antikörpern auf: als lösliche Einzeldomänen können sie leicht in bi- oder multispezifischem Format produziert werden und ihre geringe Größe erleichtert die Gewebepenetration. Die Arbeitsgruppe Koch-Nolte Labor am UKE hat P2X7-antagonisierende Nanobodies entwickelt, die bei entzündlichen Erkrankungen im Tiermodell therapeutische Wirkung zeigen. Allerdings ist bisher unklar, inwieweit diese Nanobodies den P2X7 Rezeptor auf der Oberfläche von Gewebe-residenten Immunzellen in vivo erreichen.

Ziel dieser Arbeit war es, einen durchflusszytometrischen Assay zum Nachweis von injizierten, bzw. endogen im Organismus synthetisierten, P2X7-spezifischen Nanobodies auf Gewebe-residenten Immunzellen zu entwickeln und damit zu klären, inwiefern Nanobodies in vivo endotheliale Barrieren überwinden können. Hierzu wurden die Bindungsstärke, die in vivo Halbwertszeit, die Löslichkeit, der isoelektrische Punkt und die P2X7-antagonisierende Funktion der Nanobodies durch Klonierung und gezielte Mutagenese optimiert. Nach Überprüfung dieser Parameter in Zellkulturmodellen in vitro, wurde in Pilotexperimenten im Mausmodell in vivo das Targeting von P2X7 auf cerebraler Microglia und renalen T Zellen durch injizierte bzw. endogen produzierte Nanobodies untersucht.

Die Ergebnisse zeigen 4 Stunden nach intravenöser Injektion ein effizienteres Targeting von P2X7 auf renalen T-Zellen als auf cerebraler Microglia ($EC_{50} \sim 100 \mu\text{g}/\text{kg}$ vs. $50 \text{ mg}/\text{kg}$). 18 Stunden nach intracerebroventrikulärer Injektion wurde auch mit deutlich niedrigeren Nanobody-Dosen eine weitgehende Sättigung von P2X7 auf Microglia erreicht. Nach intramuskulärer Injektion von Nanobody-kodierenden AAV-Vektoren erzielten die endogen produzierten Nanobodies auch nach 6 Monaten noch eine weitgehende Sättigung von P2X7 auf renalen und cerebralen Immunzellen. Die Ergebnisse ermöglichen künftig ein besseres therapeutisches Targeting von P2X7 auf Immunzellen in Gehirn und Niere.

7. Abbreviations

3D	three dimensional
AAV	adeno-associated virus
A β	β -amyloid peptide
ACK	ammonium-Chloride-Potassium
AD	Alzheimer's disease
ADAM	disintegrin and metalloprotease
ADCC	antibody-dependent cellular cytotoxicity
ATP	Adenosine triphosphate
AET	active efflux transport
AMT	adsorptive mediated transcytosis
ART2	ADP-ribosyl transferase 2
ASC	apoptosis associated speck-like adaptor protein
APC	professional antigen processing cells
AR	adenosine receptors
ATP	adenosine triphosphate
BBB	blood brain barrier
BCA	bicinchoninic acid
BSA	bovine serum albumin
BME	Basal Medium Eagle
CD	cluster of differentiation
CDC	complement dependent cytotoxicity
CDR	complementary determining region
CH	constant domain of the antibody heavy chain
CL	constant domain of the light chain
CNS	central nervous system
CMT	carrier-mediated transport
CSF	cerebrospinal fluid
DAMP	damage-associated molecular pattern
DAPI	4',6-diamidino-2-phenylindole
DMEM	Dulbecco's modified Eagle medium
DNA	deoxyribonucleic acid
dNTP	deoxyribonucleotide triphosphate
EAE	experimental autoimmune encephalomyelitis
EAG	experimental autoimmune glomerulonephritis
EDTA	ethylenediaminetetraacetic acid
ELISA	enzyme-linked immunosorbent assay
ESAM	endothelial selective adhesion molecule
Fab	fragment antigen binding
FACS	fluorescence-activated cell sorting
Fc	fragment of crystallization
FcRn	neonatal Fc receptor
FCS	fetal calf serum
Fig.	figure
FR	framework regions
FSC	forward scatter
hcAbs	heavy chain antibody
HEK	human embryonal kidney cells

HEPES	4-(2-hydroxyethyl)-1-piperazineethanesulfonic acid
HLE	half-life extended
HRP	Horseradish Peroxidase
HSB	histidine sucrose buffer
icb	intracerebral
icv	intracerebroventricular
Ig	immunoglobulin
iv	intravenous
IL-6R	interleukin 6 receptor
IL18	interleukin-18
IL1- β	interleukin-1 β
IMAC	immobilized metal ion affinity chromatography
iNKT	iNKT
JAMs	junctional adhesion molecules
kDa	kilodalton
LB	Luria broth
LPS	lipopolysaccharide
mAb	monoclonal antibody
MCAO	middle cerebral artery occlusion
MES	2-(N-morpholino) ethanesulfonic acid
mP2X7	mouse P2X7
MS	multiple sclerosis
MHC-II	major histocompatibility complex class II
NAD+	nicotinamide adenine dinucleotide
NALP3	NOD-like receptor subfamily containing a pyrin domain 3
NF κ β	nuclear factor kappa-light-chain-enhancer of activated B cells
Nb	Nanobody
Ni-NTA	nickel-nitriloacetic acid
NVU	neurovascular unit
P2X7	P2X purinoceptor 7
PAMP	pathogen-associated molecular patterns
PAGE	polyacrylamide gel electrophoresis
PBS	phosphate buffer saline
PCR	polymerase chain reaction
PECAM	platelet–endothelial cell adhesion molecule
pI	isoelectric point
PRR	pattern recognition receptors
RA	rheumatoid arthritis
ROS	Reactive oxygen species
RTM	receptor mediated transcytosis
RPMI	Roswell Park Memorial Institute (medium)
RT	room temperature
sdAb	single domain antibody
scFv	single chain variable fragment
SDS	sodium dodecyl sulfate
SOC	super optimal broth with catabolite repression
SSC	sideward scatter
TACE	tumor necrosis factor- α converting enzyme
TAE	tris-acetate-EDTA

TfR	transferrin receptor
Th	T helper cells
TLR	Toll-like receptor
TMB	3,3',5,5'-Tetramethylbenzidine
TNF- α	tumor necrosis factor- α
Trm	tissue resident memory T cells
UV	ultraviolet
V	volt
VE-cadherin	vascular endothelial cadherin
VH	variable domain of the heavy chain
VHH	variable domain of the heavy chain only antibody
VL	variable domain of the light chain
v/v	volume per volume
wt	wild type
w/v	weight per volume
ZO	zona occludens protein group

8. References

- Abbott, N.J., and A. Friedman. 2012. Overview and introduction: the blood-brain barrier in health and disease. *Epilepsia* 53 Suppl 6:1-6.
- Abbott, N.J., A.A. Patabendige, D.E. Dolman, S.R. Yusof, and D.J. Begley. 2010. Structure and function of the blood-brain barrier. *Neurobiol Dis* 37:13-25.
- Abbott, N.J., L. Ronnback, and E. Hansson. 2006. Astrocyte-endothelial interactions at the blood-brain barrier. *Nat Rev Neurosci* 7:41-53.
- Abdi, M.H., P.J. Beswick, A. Billinton, L.J. Chambers, A. Charlton, S.D. Collins, K.L. Collis, D.K. Dean, E. Fonfria, R.J. Gleave, C.L. Lejeune, D.G. Livermore, S.J. Medhurst, A.D. Michel, A.P. Moses, L. Page, S. Patel, S.A. Roman, S. Senger, B. Slingsby, J.G. Steadman, A.J. Stevens, and D.S. Walter. 2010. Discovery and structure-activity relationships of a series of pyroglutamic acid amide antagonists of the P2X7 receptor. *Bioorg Med Chem Lett* 20:5080-5084.
- Able, S.L., R.L. Fish, H. Bye, L. Booth, Y.R. Logan, C. Nathaniel, P. Hayter, and S.D. Katugampola. 2011. Receptor localization, native tissue binding and ex vivo occupancy for centrally penetrant P2X7 antagonists in the rat. *Br J Pharmacol* 162:405-414.
- Abuqayyas, L., and J.P. Balthasar. 2013. Investigation of the role of FcγR and FcRn in mAb distribution to the brain. *Mol Pharm* 10:1505-1513.
- Adriouch, S., P. Bannas, N. Schwarz, R. Fliegert, A.H. Guse, M. Seman, F. Haag, and F. Koch-Nolte. 2008. ADP-ribosylation at R125 gates the P2X7 ion channel by presenting a covalent ligand to its nucleotide binding site. *FASEB J* 22:861-869.
- Adriouch, S., C. Dox, V. Welge, M. Seman, F. Koch-Nolte, and F. Haag. 2002. Cutting edge: a natural P451L mutation in the cytoplasmic domain impairs the function of the mouse P2X7 receptor. *J Immunol* 169:4108-4112.
- Adriouch, S., S. Hubert, S. Pechberty, F. Koch-Nolte, F. Haag, and M. Seman. 2007. NAD⁺ released during inflammation participates in T cell homeostasis by inducing ART2-mediated death of naive T cells in vivo. *J Immunol* 179:186-194.
- Ali, Z., B. Laurijssens, T. Ostefeld, S. McHugh, A. Stylianou, P. Scott-Stevens, L. Hosking, O. Dewit, J.C. Richardson, and C. Chen. 2013. Pharmacokinetic and pharmacodynamic profiling of a P2X7 receptor allosteric modulator GSK1482160 in healthy human subjects. *Br J Clin Pharmacol* 75:197-207.
- Alzogaray, V., W. Danquah, A. Aguirre, M. Urrutia, P. Berguer, E. Garcia Vescovi, F. Haag, F. Koch-Nolte, and F.A. Goldbaum. 2011. Single-domain llama antibodies as specific intracellular inhibitors of SpvB, the actin ADP-ribosylating toxin of *Salmonella typhimurium*. *FASEB J* 25:526-534.
- Anderson, K.G., K. Mayer-Barber, H. Sung, L. Beura, B.R. James, J.J. Taylor, L. Qunaj, T.S. Griffith, V. Vezys, D.L. Barber, and D. Masopust. 2014. Intravascular staining for discrimination of vascular and tissue leukocytes. *Nat Protoc* 9:209-222.
- Arbeloa, J., A. Perez-Samartin, M. Gottlieb, and C. Matute. 2012. P2X7 receptor blockade prevents ATP excitotoxicity in neurons and reduces brain damage after ischemia. *Neurobiol Dis* 45:954-961.
- Arulkumaran, N., R.J. Unwin, and F.W. Tam. 2011. A potential therapeutic role for P2X7 receptor (P2X7R) antagonists in the treatment of inflammatory diseases. *Expert Opin Investig Drugs* 20:897-915.
- Baek, Y., N. Singh, A. Arunkumar, and A.L. Zydney. 2017. Effects of Histidine and Sucrose on the Biophysical Properties of a Monoclonal Antibody. *Pharm Res* 34:629-639.
- Baroja-Mazo, A., M. Barbera-Cremades, and P. Pelegrin. 2013. The participation of plasma membrane hemichannels to purinergic signaling. *Biochim Biophys Acta* 1828:79-93.

- Bartlett, R., L. Stokes, and R. Sluyter. 2014. The P2X7 receptor channel: recent developments and the use of P2X7 antagonists in models of disease. *Pharmacol Rev* 66:638-675.
- Basso, A.M., N.A. Bratcher, R.R. Harris, M.F. Jarvis, M.W. Decker, and L.E. Rueter. 2009. Behavioral profile of P2X7 receptor knockout mice in animal models of depression and anxiety: relevance for neuropsychiatric disorders. *Behav Brain Res* 198:83-90.
- Baudino, L., Y. Shinohara, F. Nimmerjahn, J. Furukawa, M. Nakata, E. Martinez-Soria, F. Petry, J.V. Ravetch, S. Nishimura, and S. Izui. 2008. Crucial role of aspartic acid at position 265 in the CH2 domain for murine IgG2a and IgG2b Fc-associated effector functions. *J Immunol* 181:6664-6669.
- Becker, D., R. Woltersdorf, W. Boldt, S. Schmitz, U. Braam, G. Schmalzing, and F. Markwardt. 2008. The P2X7 carboxyl tail is a regulatory module of P2X7 receptor channel activity. *J Biol Chem* 283:25725-25734.
- Begley, D.J., and M.W. Brightman. 2003. Structural and functional aspects of the blood-brain barrier. *Prog Drug Res* 61:39-78.
- Bianchi, B.R., K.J. Lynch, E. Touma, W. Niforatos, E.C. Burgard, K.M. Alexander, H.S. Park, H. Yu, R. Metzger, E. Kowaluk, M.F. Jarvis, and T. van Biesen. 1999. Pharmacological characterization of recombinant human and rat P2X receptor subtypes. *Eur J Pharmacol* 376:127-138.
- Blobel, C.P. 2005. ADAMs: key components in EGFR signalling and development. *Nat Rev Mol Cell Biol* 6:32-43.
- Boucher, A.A., J.C. Arnold, G.E. Hunt, A. Spiro, J. Spencer, C. Brown, I.S. McGregor, M.R. Bennett, and M. Kassiou. 2011. Resilience and reduced c-Fos expression in P2X7 receptor knockout mice exposed to repeated forced swim test. *Neuroscience* 189:170-177.
- Bousquet, G., and A. Janin. 2014. Passage of Humanized Monoclonal Antibodies Across the Blood-Brain Barrier: Relevance in the Treatment of Cancer Brain Metastases? *Journal of Applied Biopharmaceutics and Pharmacokinetics* 2:50-58.
- Bradley, H.J., J.M. Baldwin, G.R. Goli, B. Johnson, J. Zou, A. Sivaprasadarao, S.A. Baldwin, and L.H. Jiang. 2011a. Residues 155 and 348 contribute to the determination of P2X7 receptor function via distinct mechanisms revealed by single-nucleotide polymorphisms. *J Biol Chem* 286:8176-8187.
- Bradley, H.J., L.E. Browne, W. Yang, and L.H. Jiang. 2011b. Pharmacological properties of the rhesus macaque monkey P2X7 receptor. *Br J Pharmacol* 164:743-754.
- Brady, J.M., D. Baltimore, and A.B. Balazs. 2017. Antibody gene transfer with adeno-associated viral vectors as a method for HIV prevention. *Immunol Rev* 275:324-333.
- Brightman, M.W., and T.S. Reese. 1969. Junctions between intimately apposed cell membranes in the vertebrate brain. *J Cell Biol* 40:648-677.
- Brumfield, S., J.J. Matasi, D. Tulshian, M. Czarniecki, W. Greenlee, C. Garlisi, H. Qiu, K. Devito, S.C. Chen, Y. Sun, R. Bertorelli, J. Ansell, W. Geiss, V.D. Le, G.S. Martin, S.A. Vellekoop, J. Haber, and M.L. Allard. 2011. Synthesis and SAR development of novel P2X7 receptor antagonists for the treatment of pain: part 2. *Bioorg Med Chem Lett* 21:7287-7290.
- Buell, G., I.P. Chessell, A.D. Michel, G. Collo, M. Salazzo, S. Herren, D. Gretener, C. Grahames, R. Kaur, M.H. Kosco-Vilbois, and P.P. Humphrey. 1998. Blockade of human P2X7 receptor function with a monoclonal antibody. *Blood* 92:3521-3528.
- Bynoe, M.S., C. Viret, A. Yan, and D.G. Kim. 2015. Adenosine receptor signaling: a key to opening the blood-brain door. *Fluids Barriers CNS* 12:20.

- Calias, P., W.A. Banks, D. Begley, M. Scarpa, and P. Dickson. 2014. Intrathecal delivery of protein therapeutics to the brain: a critical reassessment. *Pharmacol Ther* 144:114-122.
- Chekeni, F.B., M.R. Elliott, J.K. Sandilos, S.F. Walk, J.M. Kinchen, E.R. Lazarowski, A.J. Armstrong, S. Penuela, D.W. Laird, G.S. Salvesen, B.E. Isakson, D.A. Bayliss, and K.S. Ravichandran. 2010. Pannexin 1 channels mediate 'find-me' signal release and membrane permeability during apoptosis. *Nature* 467:863-867.
- Chen, S., Q. Ma, P.R. Krafft, Y. Chen, J. Tang, J. Zhang, and J.H. Zhang. 2013. P2X7 receptor antagonism inhibits p38 mitogen-activated protein kinase activation and ameliorates neuronal apoptosis after subarachnoid hemorrhage in rats. *Crit Care Med* 41:e466-474.
- Chen, X., B. Pierce, W. Naing, M.L. Grapperhaus, and D.P. Phillion. 2010. Discovery of 2-chloro-N-((4,4-difluoro-1-hydroxycyclohexyl)methyl)-5-(5-fluoropyrimidin-2-yl)benzamide as a potent and CNS penetrable P2X7 receptor antagonist. *Bioorg Med Chem Lett* 20:3107-3111.
- Chessell, I.P., J.P. Hatcher, C. Bountra, A.D. Michel, J.P. Hughes, P. Green, J. Egerton, M. Murfin, J. Richardson, W.L. Peck, C.B. Grahames, M.A. Casula, Y. Yiangou, R. Birch, P. Anand, and G.N. Buell. 2005. Disruption of the P2X7 purinoceptor gene abolishes chronic inflammatory and neuropathic pain. *Pain* 114:386-396.
- Christy, N.P., and R.A. Fishman. 1961. Studies of the blood-cerebrospinal fluid barrier to cortisol in the dog. *J Clin Invest* 40:1997-2006.
- Chrovian, C.C., J.C. Rech, A. Bhattacharya, and M.A. Letavic. 2014. P2X7 antagonists as potential therapeutic agents for the treatment of CNS disorders. *Prog Med Chem* 53:65-100.
- Chu, K., B. Yin, J. Wang, G. Peng, H. Liang, Z. Xu, Y. Du, M. Fang, Q. Xia, and B. Luo. 2012. Inhibition of P2X7 receptor ameliorates transient global cerebral ischemia/reperfusion injury via modulating inflammatory responses in the rat hippocampus. *J Neuroinflammation* 9:69.
- Crone, C. 1965. Facilitated transfer of glucose from blood into brain tissue. *J Physiol* 181:103-113.
- Csolle, C., M. Baranyi, G. Zsilla, A. Kittel, F. Goloncser, P. Illes, E. Papp, E.S. Vizi, and B. Sperlagh. 2013. Neurochemical Changes in the Mouse Hippocampus Underlying the Antidepressant Effect of Genetic Deletion of P2X7 Receptors. *PLoS One* 8:e66547.
- Danquah, W. 2012. Selection and characterization of llama-derived anti-P2X7 single domain antibodies. In Universität Hamburg, Hamburg.
- Danquah, W., C. Meyer-Schwesinger, B. Rissiek, C. Pinto, A. Serracant-Prat, M. Amadi, D. Iacenda, J.H. Knop, A. Hammel, P. Bergmann, N. Schwarz, J. Assuncao, W. Rotthier, F. Haag, E. Tolosa, P. Bannas, E. Boue-Grabot, T. Magnus, T. Laeremans, C. Stortelers, and F. Koch-Nolte. 2016. Nanobodies that block gating of the P2X7 ion channel ameliorate inflammation. *Sci Transl Med* 8:366ra162.
- Davies, D.R., and G.H. Cohen. 1996. Interactions of protein antigens with antibodies. *Proc Natl Acad Sci U S A* 93:7-12.
- De Genst, E., K. Silence, K. Decanniere, K. Conrath, R. Loris, J. Kinne, S. Muyldermans, and L. Wyns. 2006. Molecular basis for the preferential cleft recognition by dromedary heavy-chain antibodies. *Proc Natl Acad Sci U S A* 103:4586-4591.
- Delarasse, C., R. Auger, P. Gonnord, B. Fontaine, and J.M. Kanellopoulos. 2011. The purinergic receptor P2X7 triggers alpha-secretase-dependent processing of the amyloid precursor protein. *J Biol Chem* 286:2596-2606.

- Desmyter, A., T.R. Transue, M.A. Ghahroudi, M.H. Thi, F. Poortmans, R. Hamers, S. Muyldermans, and L. Wyns. 1996. Crystal structure of a camel single-domain VH antibody fragment in complex with lysozyme. *Nat Struct Biol* 3:803-811.
- Deverman, B.E., P.L. Pravdo, B.P. Simpson, S.R. Kumar, K.Y. Chan, A. Banerjee, W.L. Wu, B. Yang, N. Huber, S.P. Pasca, and V. Gradinaru. 2016. Cre-dependent selection yields AAV variants for widespread gene transfer to the adult brain. *Nat Biotechnol* 34:204-209.
- Di Virgilio, F. 1995. The P2Z purinoceptor: an intriguing role in immunity, inflammation and cell death. *Immunol Today* 16:524-528.
- Di Virgilio, F. 2007. Liaisons dangereuses: P2X(7) and the inflammasome. *Trends Pharmacol Sci* 28:465-472.
- Di Virgilio, F., D. Dal Ben, A.C. Sarti, A.L. Giuliani, and S. Falzoni. 2017. The P2X7 Receptor in Infection and Inflammation. *Immunity* 47:15-31.
- Diaz-Hernandez, J.I., R. Gomez-Villafuertes, M. Leon-Otegui, L. Hontecillas-Prieto, A. Del Puerto, J.L. Trejo, J.J. Lucas, J.J. Garrido, J. Gualix, M.T. Miras-Portugal, and M. Diaz-Hernandez. 2012. In vivo P2X7 inhibition reduces amyloid plaques in Alzheimer's disease through GSK3beta and secretases. *Neurobiol Aging* 33:1816-1828.
- Diaz-Hernandez, M., M. Diez-Zaera, J. Sanchez-Nogueiro, R. Gomez-Villafuertes, J.M. Canals, J. Alberch, M.T. Miras-Portugal, and J.J. Lucas. 2009. Altered P2X7-receptor level and function in mouse models of Huntington's disease and therapeutic efficacy of antagonist administration. *FASEB J* 23:1893-1906.
- Dinarello, C.A. 2011. Interleukin-1 in the pathogenesis and treatment of inflammatory diseases. *Blood* 117:3720-3732.
- Domercq, M., A. Perez-Samartin, D. Aparicio, E. Alberdi, O. Pampliega, and C. Matute. 2010. P2X7 receptors mediate ischemic damage to oligodendrocytes. *Glia* 58:730-740.
- Dona, F., H. Ulrich, D.S. Persike, I.M. Conceicao, J.P. Blini, E.A. Cavalheiro, and M.J. Fernandes. 2009. Alteration of purinergic P2X4 and P2X7 receptor expression in rats with temporal-lobe epilepsy induced by pilocarpine. *Epilepsy Res* 83:157-167.
- Donnelly-Roberts, D.L., M.T. Namovic, P. Han, and M.F. Jarvis. 2009. Mammalian P2X7 receptor pharmacology: comparison of recombinant mouse, rat and human P2X7 receptors. *Br J Pharmacol* 157:1203-1214.
- Dubyak, G.R. 2012. P2X7 receptor regulation of non-classical secretion from immune effector cells. *Cell Microbiol* 14:1697-1706.
- Eden, T., S. Menzel, J. Wesolowski, P. Bergmann, M. Nissen, G. Dubberke, F. Seyfried, B. Albrecht, F. Haag, and F. Koch-Nolte. 2017. A cDNA Immunization Strategy to Generate Nanobodies against Membrane Proteins in Native Conformation. *Front Immunol* 8:1989.
- Eltzschig, H.K., T. Eckle, A. Mager, N. Kuper, C. Karcher, T. Weissmuller, K. Boengler, R. Schulz, S.C. Robson, and S.P. Colgan. 2006. ATP release from activated neutrophils occurs via connexin 43 and modulates adenosine-dependent endothelial cell function. *Circ Res* 99:1100-1108.
- Eltzschig, H.K., C.F. Macmanus, and S.P. Colgan. 2008. Neutrophils as sources of extracellular nucleotides: functional consequences at the vascular interface. *Trends Cardiovasc Med* 18:103-107.
- Engel, T., R. Gomez-Villafuertes, K. Tanaka, G. Mesuret, A. Sanz-Rodriguez, P. Garcia-Huerta, M.T. Miras-Portugal, D.C. Henshall, and M. Diaz-Hernandez. 2012. Seizure suppression and neuroprotection by targeting the purinergic P2X7 receptor during status epilepticus in mice. *FASEB J* 26:1616-1628.

- Ertl, H.C.J. 2017. Preclinical models to assess the immunogenicity of AAV vectors. *Cell Immunol*
- Evavold, C.L., J. Ruan, Y. Tan, S. Xia, H. Wu, and J.C. Kagan. 2018. The Pore-Forming Protein Gasdermin D Regulates Interleukin-1 Secretion from Living Macrophages. *Immunity* 48:35-44 e36.
- Fadeel, B. 2004. Plasma membrane alterations during apoptosis: role in corpse clearance. *Antioxid Redox Signal* 6:269-275.
- Faigle, M., J. Seessle, S. Zug, K.C. El Kasmi, and H.K. Eltzschig. 2008. ATP release from vascular endothelia occurs across Cx43 hemichannels and is attenuated during hypoxia. *PLoS One* 3:e2801.
- Ferrari, D., C. Pizzirani, E. Adinolfi, R.M. Lemoli, A. Curti, M. Idzko, E. Panther, and F. Di Virgilio. 2006. The P2X7 receptor: a key player in IL-1 processing and release. *J Immunol* 176:3877-3883.
- Fischer, H., R. Gottschlich, and A. Seelig. 1998. Blood-brain barrier permeation: molecular parameters governing passive diffusion. *J Membr Biol* 165:201-211.
- Fishman, R.A., and N.P. Christy. 1965. Fate of Adrenal Cortical Steroids Following Intrathecal Injection. *Neurology* 15:1-6.
- Foust, K.D., E. Nurre, C.L. Montgomery, A. Hernandez, C.M. Chan, and B.K. Kaspar. 2009. Intravascular AAV9 preferentially targets neonatal neurons and adult astrocytes. *Nat Biotechnol* 27:59-65.
- Friedle, S.A., M.A. Curet, and J.J. Watters. 2010. Recent patents on novel P2X(7) receptor antagonists and their potential for reducing central nervous system inflammation. *Recent Pat CNS Drug Discov* 5:35-45.
- Garbers, C., N. Janner, A. Chalaris, M.L. Moss, D.M. Floss, D. Meyer, F. Koch-Nolte, S. Rose-John, and J. Scheller. 2011. Species specificity of ADAM10 and ADAM17 proteins in interleukin-6 (IL-6) trans-signaling and novel role of ADAM10 in inducible IL-6 receptor shedding. *J Biol Chem* 286:14804-14811.
- Goloncser, F., and B. Sperlagh. 2014. Effect of genetic deletion and pharmacological antagonism of P2X7 receptors in a mouse animal model of migraine. *J Headache Pain* 15:24.
- Greenwood, J., M. Hammarlund-Udenaes, H.C. Jones, A.W. Stitt, R.E. Vandenbroucke, I.A. Romero, M. Campbell, G. Fricker, B. Brodin, H. Manninga, P.J. Gaillard, M. Schwaninger, C. Webster, K.B. Wicher, and M. Khrestchatisky. 2017. Current research into brain barriers and the delivery of therapeutics for neurological diseases: a report on CNS barrier congress London, UK, 2017. *Fluids Barriers CNS* 14:31.
- Grygorowicz, T., M. Welniak-Kaminska, and L. Struzynska. 2016. Early P2X7R-related astrogliosis in autoimmune encephalomyelitis. *Mol Cell Neurosci* 74:1-9.
- Guile, S.D., L. Alcaraz, T.N. Birkinshaw, K.C. Bowers, M.R. Ebdon, M. Furber, and M.J. Stocks. 2009. Antagonists of the P2X(7) receptor. From lead identification to drug development. *J Med Chem* 52:3123-3141.
- Gulbransen, B.D., M. Bashashati, S.A. Hirota, X. Gui, J.A. Roberts, J.A. MacDonald, D.A. Muruve, D.M. McKay, P.L. Beck, G.M. Mawe, R.J. Thompson, and K.A. Sharkey. 2012. Activation of neuronal P2X7 receptor-pannexin-1 mediates death of enteric neurons during colitis. *Nat Med* 18:600-604.
- Haag, F., S. Adriouch, A. Brass, C. Jung, S. Moller, F. Scheuplein, P. Bannas, M. Seman, and F. Koch-Nolte. 2007. Extracellular NAD and ATP: Partners in immune cell modulation. *Purinergic Signal* 3:71-81.

- Hamers-Casterman, C., T. Atarhouch, S. Muyldermans, G. Robinson, C. Hamers, E.B. Songa, N. Bendahman, and R. Hamers. 1993. Naturally occurring antibodies devoid of light chains. *Nature* 363:446-448.
- Hattori, M., and E. Gouaux. 2012. Molecular mechanism of ATP binding and ion channel activation in P2X receptors. *Nature* 485:207-212.
- Hawkins, B.T., D.B. Sykes, and D.S. Miller. 2010. Rapid, reversible modulation of blood-brain barrier P-glycoprotein transport activity by vascular endothelial growth factor. *J Neurosci* 30:1417-1425.
- He, W.J., J. Cui, L. Du, Y.D. Zhao, G. Burnstock, H.D. Zhou, and H.Z. Ruan. 2012. Spinal P2X(7) receptor mediates microglia activation-induced neuropathic pain in the sciatic nerve injury rat model. *Behav Brain Res* 226:163-170.
- Herve, F., N. Ghinea, and J.M. Scherrmann. 2008. CNS delivery via adsorptive transcytosis. *AAPS J* 10:455-472.
- Holliger, P., and P.J. Hudson. 2005. Engineered antibody fragments and the rise of single domains. *Nat Biotechnol* 23:1126-1136.
- Honore, P., C.L. Wade, C. Zhong, R.R. Harris, C. Wu, T. Ghayur, Y. Iwakura, M.W. Decker, C. Faltynek, J. Sullivan, and M.F. Jarvis. 2006. Interleukin-1alpha gene-deficient mice show reduced nociceptive sensitivity in models of inflammatory and neuropathic pain but not post-operative pain. *Behav Brain Res* 167:355-364.
- Huang, Z.X., Z.J. Lu, W.Q. Ma, F.X. Wu, Y.Q. Zhang, W.F. Yu, and Z.Q. Zhao. 2014. Involvement of RVM-expressed P2X7 receptor in bone cancer pain: mechanism of descending facilitation. *Pain* 155:783-791.
- Hubert, S., B. Rissiek, K. Klages, J. Huehn, T. Sparwasser, F. Haag, F. Koch-Nolte, O. Boyer, M. Seman, and S. Adriouch. 2010. Extracellular NAD⁺ shapes the Foxp3⁺ regulatory T cell compartment through the ART2-P2X7 pathway. *J Exp Med* 207:2561-2568.
- Idzko, M., D. Ferrari, and H.K. Eltzschig. 2014. Nucleotide signalling during inflammation. *Nature* 509:310-317.
- Ito, G., Y. Suekawa, M. Watanabe, K. Takahashi, T. Inubushi, K. Murasaki, N. Hirose, S. Hiyama, T. Uchida, and K. Tanne. 2013. P2X7 receptor in the trigeminal sensory nuclear complex contributes to tactile allodynia/hyperalgesia following trigeminal nerve injury. *Eur J Pain* 17:185-199.
- Jager, V., K. Bussow, A. Wagner, S. Weber, M. Hust, A. Frenzel, and T. Schirrmann. 2013. High level transient production of recombinant antibodies and antibody fusion proteins in HEK293 cells. *BMC Biotechnol* 13:52.
- Jiang, L.H., J.M. Baldwin, S. Roger, and S.A. Baldwin. 2013. Insights into the Molecular Mechanisms Underlying Mammalian P2X7 Receptor Functions and Contributions in Diseases, Revealed by Structural Modeling and Single Nucleotide Polymorphisms. *Front Pharmacol* 4:55.
- Jimenez-Pacheco, A., G. Mesuret, A. Sanz-Rodriguez, K. Tanaka, C. Mooney, R. Conroy, M.T. Miras-Portugal, M. Diaz-Hernandez, D.C. Henshall, and T. Engel. 2013. Increased neocortical expression of the P2X7 receptor after status epilepticus and anticonvulsant effect of P2X7 receptor antagonist A-438079. *Epilepsia* 54:1551-1561.
- Jin, C., and R.A. Flavell. 2010. Molecular mechanism of NLRP3 inflammasome activation. *J Clin Immunol* 30:628-631.
- Johnsen, K.B., A. Burkhart, F. Melander, P.J. Kempen, J.B. Vejlebo, P. Siupka, M.S. Nielsen, T.L. Andresen, and T. Moos. 2017. Targeting transferrin receptors at the blood-brain barrier improves the uptake of immunoliposomes and subsequent cargo transport into the brain parenchyma. *Sci Rep* 7:10396.

- Junger, W.G. 2011. Immune cell regulation by autocrine purinergic signalling. *Nat Rev Immunol* 11:201-212.
- Kabat, E.A., and T.T. Wu. 1991. Identical V region amino acid sequences and segments of sequences in antibodies of different specificities. Relative contributions of VH and VL genes, minigenes, and complementarity-determining regions to binding of antibody-combining sites. *J Immunol* 147:1709-1719.
- Kasuya, G., T. Yamaura, X.B. Ma, R. Nakamura, M. Takemoto, H. Nagumo, E. Tanaka, N. Dohmae, T. Nakane, Y. Yu, R. Ishitani, O. Matsuzaki, M. Hattori, and O. Nureki. 2017. Structural insights into the competitive inhibition of the ATP-gated P2X receptor channel. *Nat Commun* 8:876.
- Keystone, E.C., M.M. Wang, M. Layton, S. Hollis, and I.B. McInnes. 2012. Clinical evaluation of the efficacy of the P2X7 purinergic receptor antagonist AZD9056 on the signs and symptoms of rheumatoid arthritis in patients with active disease despite treatment with methotrexate or sulphasalazine. *Ann Rheum Dis* 71:1630-1635.
- Khakh, B.S., and R.A. North. 2006. P2X receptors as cell-surface ATP sensors in health and disease. *Nature* 442:527-532.
- Killian, D.M., S. Hermeling, and P.J. Chikhale. 2007. Targeting the cerebrovascular large neutral amino acid transporter (LAT1) isoform using a novel disulfide-based brain drug delivery system. *Drug Deliv* 14:25-31.
- Kim, J.E., S.E. Kwak, S.M. Jo, and T.C. Kang. 2009. Blockade of P2X receptor prevents astroglial death in the dentate gyrus following pilocarpine-induced status epilepticus. *Neurol Res* 31:982-988.
- Kimbler, D.E., J. Shields, N. Yanasak, J.R. Vender, and K.M. Dhandapani. 2012. Activation of P2X7 promotes cerebral edema and neurological injury after traumatic brain injury in mice. *PLoS One* 7:e41229.
- Koch-Nolte, F., J. Reyelt, B. Schossow, N. Schwarz, F. Scheuplein, S. Rothenburg, F. Haag, V. Alzogaray, A. Cauerhff, and F.A. Goldbaum. 2007. Single domain antibodies from llama effectively and specifically block T cell ecto-ADP-ribosyltransferase ART2.2 in vivo. *FASEB J* 21:3490-3498.
- Korbelin, J., G. Dogbevia, S. Michelfelder, D.A. Ridder, A. Hunger, J. Wenzel, H. Seismann, M. Lampe, J. Bannach, M. Pasparakis, J.A. Kleinschmidt, M. Schwaninger, and M. Trepel. 2016. A brain microvasculature endothelial cell-specific viral vector with the potential to treat neurovascular and neurological diseases. *EMBO Mol Med* 8:609-625.
- Kristensson, K., and Y. Olsson. 1971. Uptake of exogenous proteins in mouse olfactory cells. *Acta Neuropathol* 19:145-154.
- Kurashima, Y., T. Amiya, T. Nochi, K. Fujisawa, T. Haraguchi, H. Iba, H. Tsutsui, S. Sato, S. Nakajima, H. Iijima, M. Kubo, J. Kunisawa, and H. Kiyono. 2012. Extracellular ATP mediates mast cell-dependent intestinal inflammation through P2X7 purinoceptors. *Nat Commun* 3:1034.
- la Sala, A., D. Ferrari, F. Di Virgilio, M. Idzko, J. Norgauer, and G. Girolomoni. 2003. Alerting and tuning the immune response by extracellular nucleotides. *J Leukoc Biol* 73:339-343.
- Lamkanfi, M., and V.M. Dixit. 2009. Inflammasomes: guardians of cytosolic sanctity. *Immunol Rev* 227:95-105.
- Lammer, A.B., A. Beck, B. Grummich, A. Forschler, T. Krugel, T. Kahn, D. Schneider, P. Illes, H. Franke, and U. Krugel. 2011. The P2 receptor antagonist PPADS supports recovery from experimental stroke in vivo. *PLoS One* 6:e19983.

- Lauwereys, M., M. Arbabi Ghahroudi, A. Desmyter, J. Kinne, W. Holzer, E. De Genst, L. Wyns, and S. Muyldermans. 1998. Potent enzyme inhibitors derived from dromedary heavy-chain antibodies. *EMBO J* 17:3512-3520.
- Le Gall, S.M., P. Bobe, K. Reiss, K. Horiuchi, X.D. Niu, D. Lundell, D.R. Gibb, D. Conrad, P. Saftig, and C.P. Blobel. 2009. ADAMs 10 and 17 represent differentially regulated components of a general shedding machinery for membrane proteins such as transforming growth factor alpha, L-selectin, and tumor necrosis factor alpha. *Mol Biol Cell* 20:1785-1794.
- Letavic, M.A., B. Lord, F. Bischoff, N.A. Hawryluk, S. Pieters, J.C. Rech, Z. Sales, A.I. Velter, H. Ao, P. Bonaventure, V. Contreras, X. Jiang, K.L. Morton, B. Scott, Q. Wang, A.D. Wickenden, N.I. Carruthers, and A. Bhattacharya. 2013. Synthesis and Pharmacological Characterization of Two Novel, Brain Penetrating P2X7 Antagonists. *ACS Med Chem Lett* 4:419-422.
- Li, T., J.P. Bourgeois, S. Celli, F. Glacial, A.M. Le Sourd, S. Mecheri, B. Weksler, I. Romero, P.O. Couraud, F. Rougeon, and P. Lafaye. 2012. Cell-penetrating anti-GFAP VHH and corresponding fluorescent fusion protein VHH-GFP spontaneously cross the blood-brain barrier and specifically recognize astrocytes: application to brain imaging. *FASEB J* 26:3969-3979.
- Li, T., M. Vandesquille, F. Koukouli, C. Duffeffant, I. Youssef, P. Lenormand, C. Ganneau, U. Maskos, C. Czech, F. Grueninger, C. Duyckaerts, M. Dhenain, S. Bay, B. Delatour, and P. Lafaye. 2016. Camelid single-domain antibodies: A versatile tool for in vivo imaging of extracellular and intracellular brain targets. *J Control Release* 243:1-10.
- Lipinski, C.A. 2000. Drug-like properties and the causes of poor solubility and poor permeability. *J Pharmacol Toxicol Methods* 44:235-249.
- Lopez-Castejon, G., and D. Brough. 2011. Understanding the mechanism of IL-1beta secretion. *Cytokine Growth Factor Rev* 22:189-195.
- Mariathasan, S., D.S. Weiss, K. Newton, J. McBride, K. O'Rourke, M. Roose-Girma, W.P. Lee, Y. Weinrauch, D.M. Monack, and V.M. Dixit. 2006. Cryopyrin activates the inflammasome in response to toxins and ATP. *Nature* 440:228-232.
- Martinon, F., V. Petrilli, A. Mayor, A. Tardivel, and J. Tschopp. 2006. Gout-associated uric acid crystals activate the NALP3 inflammasome. *Nature* 440:237-241.
- Matasi, J.J., S. Brumfield, D. Tulshian, M. Czarnecki, W. Greenlee, C.G. Garlisi, H. Qiu, K. Devito, S.C. Chen, Y. Sun, R. Bertorelli, W. Geiss, V.D. Le, G.S. Martin, S.A. Vellekoop, J. Haber, and M.L. Allard. 2011. Synthesis and SAR development of novel P2X7 receptor antagonists for the treatment of pain: part 1. *Bioorg Med Chem Lett* 21:3805-3808.
- Matute, C., I. Torre, F. Perez-Cerda, A. Perez-Samartin, E. Alberdi, E. Etxebarria, A.M. Arranz, R. Ravid, A. Rodriguez-Antiguedad, M. Sanchez-Gomez, and M. Domercq. 2007. P2X(7) receptor blockade prevents ATP excitotoxicity in oligodendrocytes and ameliorates experimental autoimmune encephalomyelitis. *J Neurosci* 27:9525-9533.
- McLarnon, J.G., J.K. Ryu, D.G. Walker, and H.B. Choi. 2006. Upregulated expression of purinergic P2X(7) receptor in Alzheimer disease and amyloid-beta peptide-treated microglia and in peptide-injected rat hippocampus. *J Neuropathol Exp Neurol* 65:1090-1097.
- McQuillin, A., N.J. Bass, K. Choudhury, V. Puri, M. Kosmin, J. Lawrence, D. Curtis, and H.M. Gurling. 2009. Case-control studies show that a non-conservative amino-acid change from a glutamine to arginine in the P2RX7 purinergic receptor protein is

- associated with both bipolar- and unipolar-affective disorders. *Mol Psychiatry* 14:614-620.
- Menzel, S., N. Schwarz, F. Haag, and F. Koch-Nolte. 2018. Nanobody-Based Biologics for Modulating Purinergic Signaling in Inflammation and Immunity. *Front Pharmacol* 9:266.
- Merkus, P., H.J. Guchelaar, D.A. Bosch, and F.W. Merkus. 2003. Direct access of drugs to the human brain after intranasal drug administration? *Neurology* 60:1669-1671.
- Meyer-Schwesinger, C., S. Dehde, P. Klug, J.U. Becker, S. Mathey, K. Arefi, S. Balabanov, S. Venz, K.H. Endlich, M. Pekna, J.E. Gessner, F. Thaiss, and T.N. Meyer. 2011. Nephrotic syndrome and subepithelial deposits in a mouse model of immune-mediated anti-podocyte glomerulonephritis. *J Immunol* 187:3218-3229.
- Moon, H., H.Y. Na, K.H. Chong, and T.J. Kim. 2006. P2X7 receptor-dependent ATP-induced shedding of CD27 in mouse lymphocytes. *Immunol Lett* 102:98-105.
- Murphy, K., and C. Weaver. 2016. Janeway's Immunobiology 9th Edition. *Garland Science*
- Muruganandam, A., J. Tanha, S. Narang, and D. Stanimirovic. 2002. Selection of phage-displayed llama single-domain antibodies that transmigrate across human blood-brain barrier endothelium. *FASEB J* 16:240-242.
- Nadal, A., E. Fuentes, J. Pastor, and P.A. McNaughton. 1995. Plasma albumin is a potent trigger of calcium signals and DNA synthesis in astrocytes. *Proc Natl Acad Sci U S A* 92:1426-1430.
- Nguyen, V.K., C. Su, S. Muyldermans, and W. van der Loo. 2002. Heavy-chain antibodies in Camelidae; a case of evolutionary innovation. *Immunogenetics* 54:39-47.
- Nicke, A. 2008. Homotrimeric complexes are the dominant assembly state of native P2X7 subunits. *Biochem Biophys Res Commun* 377:803-808.
- Nickel, W., and C. Rabouille. 2009. Mechanisms of regulated unconventional protein secretion. *Nat Rev Mol Cell Biol* 10:148-155.
- Niewoehner, J., B. Bohrmann, L. Collin, E. Urich, H. Sade, P. Maier, P. Rueger, J.O. Stracke, W. Lau, A.C. Tissot, H. Loetscher, A. Ghosh, and P.O. Freskgard. 2014. Increased brain penetration and potency of a therapeutic antibody using a monovalent molecular shuttle. *Neuron* 81:49-60.
- Niyadurupola, N., P. Sidaway, N. Ma, J.D. Rhodes, D.C. Broadway, and J. Sanderson. 2013. P2X7 receptor activation mediates retinal ganglion cell death in a human retina model of ischemic neurodegeneration. *Invest Ophthalmol Vis Sci* 54:2163-2170.
- North, R.A. 2016. P2X receptors. *Philos Trans R Soc Lond B Biol Sci* 371:
- O'Farrell, P.Z., H.M. Goodman, and P.H. O'Farrell. 1977. High resolution two-dimensional electrophoresis of basic as well as acidic proteins. *Cell* 12:1133-1141.
- Pardridge, W.M. 2005. The blood-brain barrier: bottleneck in brain drug development. *NeuroRx* 2:3-14.
- Pardridge, W.M. 2012. Drug transport across the blood-brain barrier. *J Cereb Blood Flow Metab* 32:1959-1972.
- Pardridge, W.M., J. Eisenberg, and J. Yang. 1987. Human blood-brain barrier transferrin receptor. *Metabolism* 36:892-895.
- Pelegrin, P., and A. Surprenant. 2006. Pannexin-1 mediates large pore formation and interleukin-1beta release by the ATP-gated P2X7 receptor. *EMBO J* 25:5071-5082.
- Peng, W., M.L. Cotrina, X. Han, H. Yu, L. Bekar, L. Blum, T. Takano, G.F. Tian, S.A. Goldman, and M. Nedergaard. 2009. Systemic administration of an antagonist of the ATP-sensitive receptor P2X7 improves recovery after spinal cord injury. *Proc Natl Acad Sci U S A* 106:12489-12493.

- Perez-Medrano, A., D.L. Donnelly-Roberts, P. Honore, G.C. Hsieh, M.T. Namovic, S. Peddi, Q. Shuai, Y. Wang, C.R. Faltynek, M.F. Jarvis, and W.A. Carroll. 2009. Discovery and biological evaluation of novel cyanoguanidine P2X(7) antagonists with analgesic activity in a rat model of neuropathic pain. *J Med Chem* 52:3366-3376.
- Petrilli, V., S. Papin, C. Dostert, A. Mayor, F. Martinon, and J. Tschopp. 2007. Activation of the NALP3 inflammasome is triggered by low intracellular potassium concentration. *Cell Death Differ* 14:1583-1589.
- Rampe, D., L. Wang, and G.E. Ringheim. 2004. P2X7 receptor modulation of beta-amyloid- and LPS-induced cytokine secretion from human macrophages and microglia. *J Neuroimmunol* 147:56-61.
- Rao, J.S., G.J. Harry, S.I. Rapoport, and H.W. Kim. 2010. Increased excitotoxicity and neuroinflammatory markers in postmortem frontal cortex from bipolar disorder patients. *Mol Psychiatry* 15:384-392.
- Rapoport, S.I. 2000. Osmotic opening of the blood-brain barrier: principles, mechanism, and therapeutic applications. *Cell Mol Neurobiol* 20:217-230.
- Rasmussen, S.G., H.J. Choi, J.J. Fung, E. Pardon, P. Casarosa, P.S. Chae, B.T. Devree, D.M. Rosenbaum, F.S. Thian, T.S. Kobilka, A. Schnapp, I. Konetzki, R.K. Sunahara, S.H. Gellman, A. Pautsch, J. Steyaert, W.I. Weis, and B.K. Kobilka. 2011. Structure of a nanobody-stabilized active state of the beta(2) adrenoceptor. *Nature* 469:175-180.
- Richardson, D.S., and J.W. Lichtman. 2015. Clarifying Tissue Clearing. *Cell* 162:246-257.
- Roger, S., Z.Z. Mei, J.M. Baldwin, L. Dong, H. Bradley, S.A. Baldwin, A. Surprenant, and L.H. Jiang. 2010. Single nucleotide polymorphisms that were identified in affective mood disorders affect ATP-activated P2X7 receptor functions. *J Psychiatr Res* 44:347-355.
- Roman, S., F.S. Cusdin, E. Fonfria, J.A. Goodwin, J. Reeves, S.C. Lappin, L. Chambers, D.S. Walter, W.C. Clay, and A.D. Michel. 2009. Cloning and pharmacological characterization of the dog P2X7 receptor. *Br J Pharmacol* 158:1513-1526.
- Roth, T.L., D. Nayak, T. Atanasijevic, A.P. Koretsky, L.L. Latour, and D.B. McGavern. 2014. Transcranial amelioration of inflammation and cell death after brain injury. *Nature* 505:223-228.
- Rubartelli, A., F. Cozzolino, M. Talio, and R. Sitia. 1990. A novel secretory pathway for interleukin-1 beta, a protein lacking a signal sequence. *EMBO J* 9:1503-1510.
- Rubenstein, J.L., D. Combs, J. Rosenberg, A. Levy, M. McDermott, L. Damon, R. Ignoffo, K. Aldape, A. Shen, D. Lee, A. Grillo-Lopez, and M.A. Shuman. 2003. Rituximab therapy for CNS lymphomas: targeting the leptomeningeal compartment. *Blood* 101:466-468.
- Ruderisch, N., D. Schlatter, A. Kuglstatter, W. Guba, S. Huber, C. Cusulin, J. Benz, A.C. Rufer, J. Hoernschemeyer, C. Schweitzer, T. Bulau, A. Gartner, E. Hoffmann, J. Niewoehner, C. Patsch, K. Baumann, H. Loetscher, E. KITAS, and P.O. Freskgard. 2017. Potent and Selective BACE-1 Peptide Inhibitors Lower Brain Abeta Levels Mediated by Brain Shuttle Transport. *EBioMedicine* 24:76-92.
- Sanz, J.M., P. Chiozzi, D. Ferrari, M. Colaianna, M. Idzko, S. Falzoni, R. Fellin, L. Trabace, and F. Di Virgilio. 2009. Activation of microglia by amyloid {beta} requires P2X7 receptor expression. *J Immunol* 182:4378-4385.
- Schaffer, U., A. Schlosser, K.M. Muller, A. Schafer, N. Katava, R. Baumeister, and E. Schulze. 2010. SnAvi--a new tandem tag for high-affinity protein-complex purification. *Nucleic Acids Res* 38:e91.
- Scheuplein, F., B. Rissiek, J.P. Driver, Y.G. Chen, F. Koch-Nolte, and D.V. Serreze. 2010. A recombinant heavy chain antibody approach blocks ART2 mediated deletion of

- an iNKT cell population that upon activation inhibits autoimmune diabetes. *J Autoimmun* 34:145-154.
- Scheuplein, F., N. Schwarz, S. Adriouch, C. Krebs, P. Bannas, B. Rissiek, M. Seman, F. Haag, and F. Koch-Nolte. 2009. NAD⁺ and ATP released from injured cells induce P2X7-dependent shedding of CD62L and externalization of phosphatidylserine by murine T cells. *J Immunol* 182:2898-2908.
- Schlachetzki, F., C. Zhu, and W.M. Pardridge. 2002. Expression of the neonatal Fc receptor (FcRn) at the blood-brain barrier. *J Neurochem* 81:203-206.
- Seman, M., S. Adriouch, F. Scheuplein, C. Krebs, D. Freese, G. Glowacki, P. Deterre, F. Haag, and F. Koch-Nolte. 2003. NAD-induced T cell death: ADP-ribosylation of cell surface proteins by ART2 activates the cytolytic P2X7 purinoceptor. *Immunity* 19:571-582.
- Sharp, A.J., P.E. Polak, V. Simonini, S.X. Lin, J.C. Richardson, E.R. Bongarzone, and D.L. Feinstein. 2008. P2x7 deficiency suppresses development of experimental autoimmune encephalomyelitis. *J Neuroinflammation* 5:33.
- Shi, J., W. Gao, and F. Shao. 2017. Pyroptosis: Gasdermin-Mediated Programmed Necrotic Cell Death. *Trends Biochem Sci* 42:245-254.
- Sims, J.E., and D.E. Smith. 2010. The IL-1 family: regulators of immunity. *Nat Rev Immunol* 10:89-102.
- Smart, M.L., B. Gu, R.G. Panchal, J. Wiley, B. Cromer, D.A. Williams, and S. Petrou. 2003. P2X7 receptor cell surface expression and cytolytic pore formation are regulated by a distal C-terminal region. *J Biol Chem* 278:8853-8860.
- Soderlund, J., S.K. Olsson, M. Samuelsson, L. Walther-Jallow, C. Johansson, S. Erhardt, M. Landen, and G. Engberg. 2011. Elevation of cerebrospinal fluid interleukin-1ss in bipolar disorder. *J Psychiatry Neurosci* 36:114-118.
- Solle, M., J. Labasi, D.G. Perregaux, E. Stam, N. Petrushova, B.H. Koller, R.J. Griffiths, and C.A. Gabel. 2001. Altered cytokine production in mice lacking P2X(7) receptors. *J Biol Chem* 276:125-132.
- Soronen, P., O. Mantere, T. Melartin, K. Suominen, M. Vuorilehto, H. Rytala, P. Arvilommi, I. Holma, M. Holma, P. Jylha, H.M. Valtonen, J. Haukka, E. Isometsa, and T. Paunio. 2011. P2RX7 gene is associated consistently with mood disorders and predicts clinical outcome in three clinical cohorts. *Am J Med Genet B Neuropsychiatr Genet* 156B:435-447.
- Sperlagh, B., and P. Illes. 2014. P2X7 receptor: an emerging target in central nervous system diseases. *Trends Pharmacol Sci* 35:537-547.
- Stanimirovic, D., K. Kemmerich, A.S. Haqqani, and G.K. Farrington. 2014. Engineering and pharmacology of blood-brain barrier-permeable bispecific antibodies. *Adv Pharmacol* 71:301-335.
- Stock, T.C., B.J. Bloom, N. Wei, S. Ishaq, W. Park, X. Wang, P. Gupta, and C.A. Mebus. 2012. Efficacy and safety of CE-224,535, an antagonist of P2X7 receptor, in treatment of patients with rheumatoid arthritis inadequately controlled by methotrexate. *J Rheumatol* 39:720-727.
- Stortelers, C., C. Pinto-Espinoza, D. Van Hoorick, and F. Koch-Nolte. 2018. Modulating ion channel function with antibodies and nanobodies. *Curr Opin Immunol* 52:18-26.
- Subramanyam, C., A.J. Duplantier, M.A. Dombroski, S.P. Chang, C.A. Gabel, C. Whitney-Pickett, D.G. Perregaux, J.M. Labasi, K. Yoon, R.M. Shepard, and M. Fisher. 2011. Discovery, synthesis and SAR of azinyl- and azolylbenzamides antagonists of the P2X(7) receptor. *Bioorg Med Chem Lett* 21:5475-5479.
- Sun, H., and M. Li. 2013. Antibody therapeutics targeting ion channels: are we there yet? *Acta Pharmacol Sin* 34:199-204.

- Surprenant, A., F. Rassendren, E. Kawashima, R.A. North, and G. Buell. 1996. The cytolytic P2Z receptor for extracellular ATP identified as a P2X receptor (P2X7). *Science* 272:735-738.
- Suzuki, T., I. Hide, K. Ido, S. Kohsaka, K. Inoue, and Y. Nakata. 2004. Production and release of neuroprotective tumor necrosis factor by P2X7 receptor-activated microglia. *J Neurosci* 24:1-7.
- Takenouchi, T., S. Sugama, Y. Iwamaru, M. Hashimoto, and H. Kitani. 2009. Modulation of the ATP-Induced release and processing of IL-1beta in microglial cells. *Crit Rev Immunol* 29:335-345.
- Taylor, S.R., C.M. Turner, J.I. Elliott, J. McDaid, R. Hewitt, J. Smith, M.C. Pickering, D.L. Whitehouse, H.T. Cook, G. Burnstock, C.D. Pusey, R.J. Unwin, and F.W. Tam. 2009. P2X7 deficiency attenuates renal injury in experimental glomerulonephritis. *J Am Soc Nephrol* 20:1275-1281.
- Tijink, B.M., T. Laeremans, M. Budde, M. Stigter-van Walsum, T. Dreier, H.J. de Haard, C.R. Leemans, and G.A. van Dongen. 2008. Improved tumor targeting of anti-epidermal growth factor receptor Nanobodies through albumin binding: taking advantage of modular Nanobody technology. *Mol Cancer Ther* 7:2288-2297.
- Trauble, H. 1971. The movement of molecules across lipid membranes: A molecular theory. *J Membr Biol* 4:193-208.
- Tschopp, J., and K. Schroder. 2010. NLRP3 inflammasome activation: The convergence of multiple signalling pathways on ROS production? *Nat Rev Immunol* 10:210-215.
- Uchida, Y., S. Ohtsuki, Y. Katsukura, C. Ikeda, T. Suzuki, J. Kamiie, and T. Terasaki. 2011. Quantitative targeted absolute proteomics of human blood-brain barrier transporters and receptors. *J Neurochem* 117:333-345.
- Venkatachalam, M.A., and H.G. Rennke. 1978. The structural and molecular basis of glomerular filtration. *Circ Res* 43:337-347.
- Vu, K.B., M.A. Ghahroudi, L. Wyns, and S. Muyldermans. 1997. Comparison of llama VH sequences from conventional and heavy chain antibodies. *Mol Immunol* 34:1121-1131.
- Weber, F., B. Bohrmann, J. Niewoehner, J.A.A. Fischer, P. Rueger, G. Tiefenthaler, J. Moelleken, A. Bujotzek, K. Brady, T. Singer, M. Ebeling, A. Iglesias, and P.O. Freskgard. 2018. Brain Shuttle Antibody for Alzheimer's Disease with Attenuated Peripheral Effector Function due to an Inverted Binding Mode. *Cell Rep* 22:149-162.
- Weber, F.C., P.R. Esser, T. Muller, J. Ganesan, P. Pellegatti, M.M. Simon, R. Zeiser, M. Idzko, T. Jakob, and S.F. Martin. 2010. Lack of the purinergic receptor P2X(7) results in resistance to contact hypersensitivity. *J Exp Med* 207:2609-2619.
- Wesolowski, J., V. Alzogaray, J. Reyelt, M. Unger, K. Juarez, M. Urrutia, A. Cauerhff, W. Danquah, B. Rissiek, F. Scheuplein, N. Schwarz, S. Adriouch, O. Boyer, M. Seman, A. Licea, D.V. Serreze, F.A. Goldbaum, F. Haag, and F. Koch-Nolte. 2009. Single domain antibodies: promising experimental and therapeutic tools in infection and immunity. *Med Microbiol Immunol* 198:157-174.
- Yan, Z., A. Khadra, S. Li, M. Tomic, A. Sherman, and S.S. Stojilkovic. 2010. Experimental characterization and mathematical modeling of P2X7 receptor channel gating. *J Neurosci* 30:14213-14224.
- Yan, Z., S. Li, Z. Liang, M. Tomic, and S.S. Stojilkovic. 2008. The P2X7 receptor channel pore dilates under physiological ion conditions. *J Gen Physiol* 132:563-573.
- Young, M.T. 2010. P2X receptors: dawn of the post-structure era. *Trends Biochem Sci* 35:83-90.

- Yu, Q., Z. Guo, X. Liu, Q. Ouyang, C. He, G. Burnstock, H. Yuan, and Z. Xiang. 2013. Block of P2X7 receptors could partly reverse the delayed neuronal death in area CA1 of the hippocampus after transient global cerebral ischemia. *Purinergic Signal* 9:663-675.
- Zhang, B., X. Sun, H. Mei, Y. Wang, Z. Liao, J. Chen, Q. Zhang, Y. Hu, Z. Pang, and X. Jiang. 2013. LDLR-mediated peptide-22-conjugated nanoparticles for dual-targeting therapy of brain glioma. *Biomaterials* 34:9171-9182.

9. List of Figures and tables

Figure 1. Structural characteristics of P2X7.	5
Figure 2. ATP-induced P2X7-mediated downstream effects on microglia and T lymphocytes.	7
Figure 3. Structural features of conventional antibodies vs. heavy chain antibodies	15
Figure 4. Components of the Blood brain barrier (BBB) and potential pathways for drug delivery to the brain.	19
Figure 5. Schematic diagram of bivalent, engineered, half-life extended P2X7-antagonistic nanobodies.	53
Figure 6. Expression, purification and chemical characterization of engineered nanobodies.	56
Figure 7. Monovalent and bivalent formats nanobodies bind with high specificity to P2X7.	58
Figure 8. Bivalent P2X7-specific nanobodies block ATP-induced influx of Ca^{2+} more potently than their monovalent counterparts.	59
Figure 9. Bivalent half-life extended P2X7-specific nanobodies effectively block ATP-induced release of IL-1 β by endotoxin-primed mouse microglia.	60
Figure 10. Bivalent half-life extended P2X7-specific nanobody 13A7 blocks ATP-induced activation of the inflammasome by endotoxin-primed mouse peritoneal macrophages.	61
Figure 11. Experimental strategy to assess occupancy of cell surface P2X7 achieved by systemically injected bivalent HLE-nanobodies.	63
Figure 12. Full occupancy of P2X7 on microglia is achieved only by a high dose (3.2 mg) of intravenously injected 13A7-dim HLE.	65
Figure 13. Full occupancy of P2X7 on renal CD4+ T cells is achieved already by low doses ($> 10 \mu\text{g}$) of intravenously injected 13A7-dim HLE.	67
Figure 14. The concentration of unbound 13A7-dim HLE in serum 4 h after intravenous injection correlates with the administered dose.	69
Figure 15. Full occupancy of P2X7 on microglia is achieved only by a high dose ($> 1 \text{ mg}$) of intravenously injected 1c81-dim HLE and 13A7-mlgG2c.	71
Figure 16. 190 days after intramuscular injection of 13A7-dim-HLE encoding AAV vectors, endogenously produced nanobodies are bound to P2X7 on microglia.	73
Figure 17. 190 days after intramuscular injection of 13A7-dim-HLE encoding AAV vectors, endogenously produced nanobodies are bound to P2X7 on renal CD4+ T cells.	75
Figure 18. The concentration of 13A7-dim HLE in serum 6 months after injection of AAV is similar to that seen 4 hours after intravenous injection of $30 \mu\text{g}$ 13A7-dim HLE.	76
Figure 19. Full occupancy of P2X7 on microglia is achieved by a low dose ($> 10 \mu\text{g}$) of icv injected 1c81-dim ^{sh} HLE.	77
Figure 20. Full occupancy of P2X7 on renal CD4+ T cells is achieved by a low dose ($> 10 \mu\text{g}$) of icv injected 1c81-dim ^{sh} HLE.	79
Figure 21. Only very low concentrations of unbound 1c81-dim ^{sh} HLE ($< 2 \mu\text{g/ml}$) can be detected in serum 18 h after icv administration.	80
Figure 22. 48 h following icv administration, a low dose of bivalent HLE nanobodies achieved full occupancy of P2X7 in microglia.	81
Figure 23. Schematic representation of the engineered bivalent P2X7-specific nanobodies analyzed in this thesis.	82

Figure 24. Transport of drug molecules following intracerebroventricular (icv) injection.	88
Figure 25. Strategies for facilitating transport of biologics across the BBB.	90
Table 1. PCR reaction with KOD polymerase.	33
Table 2. Standard PCR amplification.	34
Table 3. Mutagenesis PCR reaction.	34
Table 4. Mutagenesis PCR amplification.	34
Table 5. Physicochemical properties of the engineered nanobodies.	83
Table 6. Potential advantages and limitations of P2X7-antagonistic nanobodies vs. lipidized small molecules inhibitors.	84
Table 7. Assessment of target engagement of engineered P2X7-antagonistic nanobodies in brain microglia vs. renal Trm cells.	86

10. Acknowledgements

I would like to express my deep gratitude first and foremost to Prof. Dr. Friedrich Koch-Nolte for giving me the opportunity, 4.5 years ago, to pursue my professional dream of doing a PhD in the field of nanobodies. Thank you Fritz for your constant support at the scientific level, for guiding me to address scientific questions and the provided freedom to implement my own scientific ideas. I learnt from you to develop a scientific analytical reasoning. I thank you also for the encouragement to attend conferences, where I got the inspiration to expand my project and finally, I am really grateful for the support at the human level with your advice during all this time.

I would like to sincerely acknowledge Dr. Nicole Schwarz, I appreciate Nic Nic for your smile every day, the fruitful collaboration, the scientific discussions, brainstorming, proofreading my thesis and especially for the soul-connection we built. I will always remember our crazy long nights in front of our beloved friend CELESTA, we had so much fun working together. I extend my thanks to Mr. Marten Junge, for your help during common experiments, your input with good ideas and your good mood during long days.

I am especially grateful with Dr. Björn Rissiek, I really appreciate your contribution in my project, the feedback, scientific discussions, all the support during animal experiments and finally for proofreading my thesis. I wish also to thank Dr. Ehsan Javidi for his assistance with the intracerebroventricular injections and Mrs. Larissa Jank for the help with the microglia cultures.

Moreover, I am really thankful with Dr. Sahil Adriouch, for the collaboration we established regarding the AAV-based delivery of nanobodies, for sharing his knowledge with me, his ideas and suggestions on my project and contagious enthusiasm.

I would like to express my sincere appreciation to Dr. Catelijne Stortelers from Ablynx, for all the feedback regarding my project, the exchanged mails, sharing of your expertise with me and for kindly sending me all the material needed to keep on carrying out my project.

My special thanks go to Dr. Anna Eichhoff for proofreading my thesis, por los lindos momentos que pasamos en el lab y por hacerme sentir como en casa. Further, many thanks to all my colleagues and principal investigators from IFI land, especially Mr.

Klaus Kaschubowski, Dr. Thomas Eden, Dr. Stephan Menzel and Mrs. Intissar Chahbani for being always ready to help, Dr. Anne Rissiek for the encouragement during writing and my colleague and friend Mr. Arnau Serracant-Prat for his support at all levels, it was a joy living with you. I also extend my thanks to Mrs. Fabienne Seyfried, Mrs. Marion Nissen, Mrs. Birte Albrecht, Mrs. Lynn Dieckow, Mrs. Gudrun Dubberke and Mrs. Joanna Smith for the exceptional technical assistance and the nice time.

I very much appreciate the financial support from the DAAD and Prof. Dr. Friedrich Koch-Nolte that allowed me to perform my doctoral thesis.

Mis agradecimientos más profundos a mi familia en Perú, porque siempre estuvieron ahí para mi cuando lo necesité, aunque estuvieron lejos sentí su apoyo incondicional, gracias pa, Vashofer y José y especialmente a ti mami por siempre animarme a mirar al cielo y volar sin miedo. Los amo muchísimo.

Last but not least, I wish to express my eternal gratitude to the second author of this thesis, Mr. Dimitrios Volikakis, I thank you for believing in me when I couldn't, for listening to me and holding my hand when I needed the most. Mi amor precioso, ευχαριστώ πολύ, te amo inmensamente.

Curriculum vitae

Lebenslauf entfällt aus datenschutzrechtlichen Gründen.

Eidesstattliche Versicherung

Ich versichere ausdrücklich, dass ich die Arbeit selbständig und ohne fremde Hilfe verfasst, andere als die von mir angegebenen Quellen und Hilfsmittel nicht benutzt und die aus den benutzten Werken wörtlich oder inhaltlich entnommenen Stellen einzeln nach Ausgabe (Auflage und Jahr des Erscheinens), Band und Seite des benutzten Werkes kenntlich gemacht habe.

Ferner versichere ich, dass ich die Dissertation bisher nicht einem Fachvertreter an einer anderen Hochschule zur Überprüfung vorgelegt oder mich anderweitig um Zulassung zur Promotion beworben habe.

Ich erkläre mich einverstanden, dass meine Dissertation vom Dekanat der Medizinischen Fakultät mit einer gängigen Software zur Erkennung von Plagiaten überprüft werden kann.

Unterschrift:

The GPMRT mutant of Nb 1c81 described in section 3.1 (Fig. 5) as well as the antibodies mAb74, mAb77, pAbR345 described in Fig. 14 and Fig. 18 were kindly provided by Dr. Catelijne Stortelers, Ablynx, Ghent, Belgium. Cultivation of microglia (Fig. 9) and peritoneal macrophages (Fig. 10) were performed with assistance by Larissa Jank and Dr. Björn Rissiek, Dept. Neurology, UKE. Experiments with injections of nanobodies and flow cytometry analyses of brain and kidney cells described in sections 3.3.1-3.3.4 (Figs. 11-15, 19-21) were performed together with Marten Junge, Dr. Nicole Schwarz, Institute of Immunology, UKE, and Dr. Björn Rissiek, Dr. Ehsan Javidi, Dept. of Neurology, UKE. Dr. Sahil Adriouch, Univ. Rouen, France kindly provided HEK cells stably transfected with mouse P2X7 (Fig. 8) and assistance with the AAV transduction of muscle cells described in section 3.3.5 (Fig. 16-18).

Angenommen von der Medizinischen Fakultät am: 01.03.2019

Veröffentlichung mit Genehmigung der medizinischen Fakultät der Universität Hamburg.

Prüfungsausschuss, der/die Vorsitzende: Prof. Dr. Friedrich Koch-Nolte

Prüfungsausschuss, 2. Gutachter/in: Prof. Dr. Tim Magnus